Technische Universität München
Institut für Energietechnik

Professur für Thermofluiddynamik

Time Scales of Equivalence Ratio and Inertial Waves in Unsteady Combustion Dynamics

Alp Albayrak

Vollständiger Abdruck der von der Fakultät für Maschinenwesen der Technischen Universität München zur Erlangung des akademischen Grades eines

DOKTOR – INGENIEURS

genehmigten Dissertation.

Vorsitzender:
Prof. Dr.-Ing. Wolfgang A. Wall
Prüfer der Dissertation:
1. Prof. Wolfgang Polifke, Ph.D.
2. Prof. Aimee S. Morgans, Ph.D.

Die Dissertation wurde am 11.09.2018 bei der Technischen Universität München eingereicht und durch die Fakultät für Maschinenwesen am 01.03.2019 angenommen.

Abstract

Combustion systems are prone to thermo-acoustic instabilities. The flame response to acoustic waves is an important mechanism that controls instabilities. The estimation of the flame response is a crucial step in state-of-art modeling approaches. In industrial application, e.g. gas turbines, technically premixed swirl stabilized flames are commonly employed. For such systems, two different mechanisms, namely *inertial waves* and *equivalence ratio waves*, have a strong impact on the flame response besides direct contribution of acoustic waves. This work focuses on the accurate estimation and the physical interpretation of relevant time scales of these two mechanisms.

Inertial waves are generated by acoustic waves crossing the swirler. These waves are also recognized as *swirl waves* in literature, which are commonly assumed to propagate with the bulk flow velocity. In this thesis, the dispersive nature of inertial waves in rotating flows is shown to cause a deviation in propagation speed around 40-50% from the bulk velocity. The wave propagation speed is derived from the dispersion relation by employing a linear hydrodynamic stability analysis formalism. The step response solution is obtained by posing an initial value problem. This serves as an accurate time lag model for inertial waves in thermo-acoustic network models. Moreover, a novel contribution to the list of flame interaction mechanisms caused by tangential velocity fluctuations is identified using inertial wave dynamics.

Equivalence ratio waves are generated by acoustic waves crossing the fuel injector. The flame frequency response to equivalence ratio fluctuations has been extensively studied in the literature. Three major contributions that cause heat release rate fluctuations were identified. Fluctuations in the heat of reaction and the burning speed acts on the flame directly, whereas fluctuations in the flame surface area are caused indirectly by the burning speed perturbations. In this thesis, physical interpretation to these contributions is given by employing a time domain approach. The level set G-equation flame model is used to derive the relevant time scales, and their contribution to the flame response is discussed. Similar to inertial waves, the step response solution is derived to quantify the propagation of equivalence ratio waves. For technically premixed flames, the analytical flame response model is further improved by including molecular diffusion.

Kurzfassung

Verbrennungssysteme sind anfällig für thermoakustische Instabilitäten. Die Flammenantwort auf akustische Wellen ist ein wichtiger Mechanismus der auf Instabilitäten wirkt. Die Abschätzung der Flammenantwort ist ein kritischer Punkt für aktuelle thermoakustische Modelle. In industriellen Anwendungen von z.B. Gasturbinen werden häufig drallstabilisierte, technisch-vorgemischte Flammen verwendet. Für solche Systeme haben, neben akustischen Wellen, *Trägheitswellen* und *Äquivalenzverhaltniswellen* einen starken Einfluss auf die Flammenantwort. Die präzise Abschätzung und die physikalische Interpretation der charakteristischen Zeitskalen dieser Wellen bilden den Schwerpunkt der vorliegenden Dissertation.

Akustische Wellen, die auf einen Drallerzeuger treffen, generieren Trägheitswellen. In der Literatur werden diese Wellen auch als *Drallwellen* bezeichnet, fr deren Ausbreitung die konvektive Geschwindigkeit angenommen wird. In dieser Arbeit wird gezeigt, dass die dispersive Ausbreitung der Trägheitswellen eine Abweichung von ca. 40-50% in der Konvektionsgeschwindigkeit verursacht. Die Wellengeschwindigkeit ist aus der linearen hydrodynamischer Stabilitätsanalyse mit Hilfe der Dispersionsrelation abgeleitet. Ein präzises Zeitverzugsmodell für thermoakustische Netzwerkmodelle wird als Anfangswertproblem aufgestellt und mittels einer Sprungantwort gelöst. Es wird gezeigt, dass Trägheitswellen eine neue Interpretation der Flammenantwort liefern: tangentiale Geschwindigkeitsstörungen, die im Falle einer symmetrischen Flamme keine fluktuierende Wärmefreisetzung hervorrufen, erzeugen axiale Geschwindigkeitsfluktuationen, die durch Trägheitswellen verursacht werden, und diese schließlich Fluktuationen der Wärmefreisetzungsrate generieren.

Aquivalenzverhältniswellen werden durch akustische Wellen generiert, die auf die Brennstoffeindüsung treffen. Die Flammenantwort verursacht durch Aquivalenzverhältniswellen im Frequenzbereich wurde bereits eingehend in der Literatur diskutiert. Drei wesentliche Beiträge, die Fluktuationen der Wärmefreisetzung verursachen, sind beschrieben. Fluktuationen der Reaktionswärme und der Flammengeschwindigkeit wirken direkt auf die Flamme, während Fluktuationen der Flammenoberfläche durch die Flammengeschwindigkeitstörung indirekt verursacht wird. In dieser Dissertation wird die physikalische Interpretation dieser Beiträge im Zeitbereich vorgestellt. Die charakteristischen Zeitskalen sind anhand des Level-Set G-Gleichung Flammenmodels hergeleitet und ihr Einfluss auf die Flammenantwort wird diskutiert. Die Sprungantwort wird analog zu den bereits erwähnten Trägheitswellen hergeleitet, um die Ausbreitung der Aquivalenzverhältniswellen zu quantifizieren. Für technisch-vorgemischte Flammen wird das analytische Flammenantwortmodell weiter durch Einbeziehung der molekularen Diffusion verbessert.

Contents

1 Introduction

Over last decades, the gas turbine combustion design shifted to lean premixtures in response to stricter emission regulations. However, lean premixed flames are prone to thermo-acoustic instabilities, which might reduce the lifespan of the combustor or even cause structural damage. Thermo-acoustic instabilities are understood as a coupling between acoustics and flame dynamics: Acoustic waves feed energy into the flame and cause unsteady heat release rate. The latter causes acoustic oscillations in return so that a feedback loop is formed. In the 1800s, Rayleigh [1] introduced a famous criterion to explain the nature of this instability. According to this criterion, the instability is encouraged if fluctuations of the heat release and the acoustic pressure are in phase. This introduced a fundamental point of view to thermo-acoustics and formed a basis for the further research on the subject.

Thermo-acoustics is a multiscale phenomenon comprised of large acoustic and small turbulent combustion scales. The state of art modeling approach to predict thermo-acoustic instabilities is to employ low order network models [2] for acoustic elements, e.g. ducts, area jumps and swirl generators, and to couple them with a *flame transfer function*. The flame transfer function, $F(\omega)$ is the frequency response of the unsteady heat release rate, $\dot{Q}'$, to upstream acoustic velocity perturbations, u', and defined as

$$\frac{\hat{\dot{Q}}}{\bar{\dot{Q}}} = F(\omega)\frac{\hat{u}}{\bar{u}} \,, \tag{1.1}$$

where ω indicates the angular frequency. The Fourier transformed perturbed quantities are indicated by $\hat{(\cdot)}$ and the normalization is achieved by dividing the quantities by mean values, $\bar{(\cdot)}$.

For perfectly premixed flames, the major mechanism of the flame response is the flame front kinematics. The top part of Fig. 1.1 illustrates this mechanism schematically. Acoustic waves across the dump plane generate kinematic waves, which modulate the flame front and thus cause unsteady heat release rate. This mechanism is extensively studied in the literature (see [3–6]) and is not the focus of this thesis. In industrial combustion applications, the flame response depends also on two other mechanisms that are caused by acoustic waves, i.e. *equivalence ratio waves* and *inertial waves*. These mechanisms are illustrated schematically in Fig. 1.1. The reader may refer to Polifke [7], Lieuwen [8] for an introductory level description of the subject. The overall flame response is the superposition of three contributions represented in Fig. 1.1. In the presence of multiple mechanisms, corresponding time delays affect the flame response strongly due to the constructive/destructive superposition in the unsteady heat release depending on the frequency.

To elucidate the importance of the superposition principle on an introductory level, a pedagogic toy model example is presented here. An idealized premixed flame that is acoustically forced

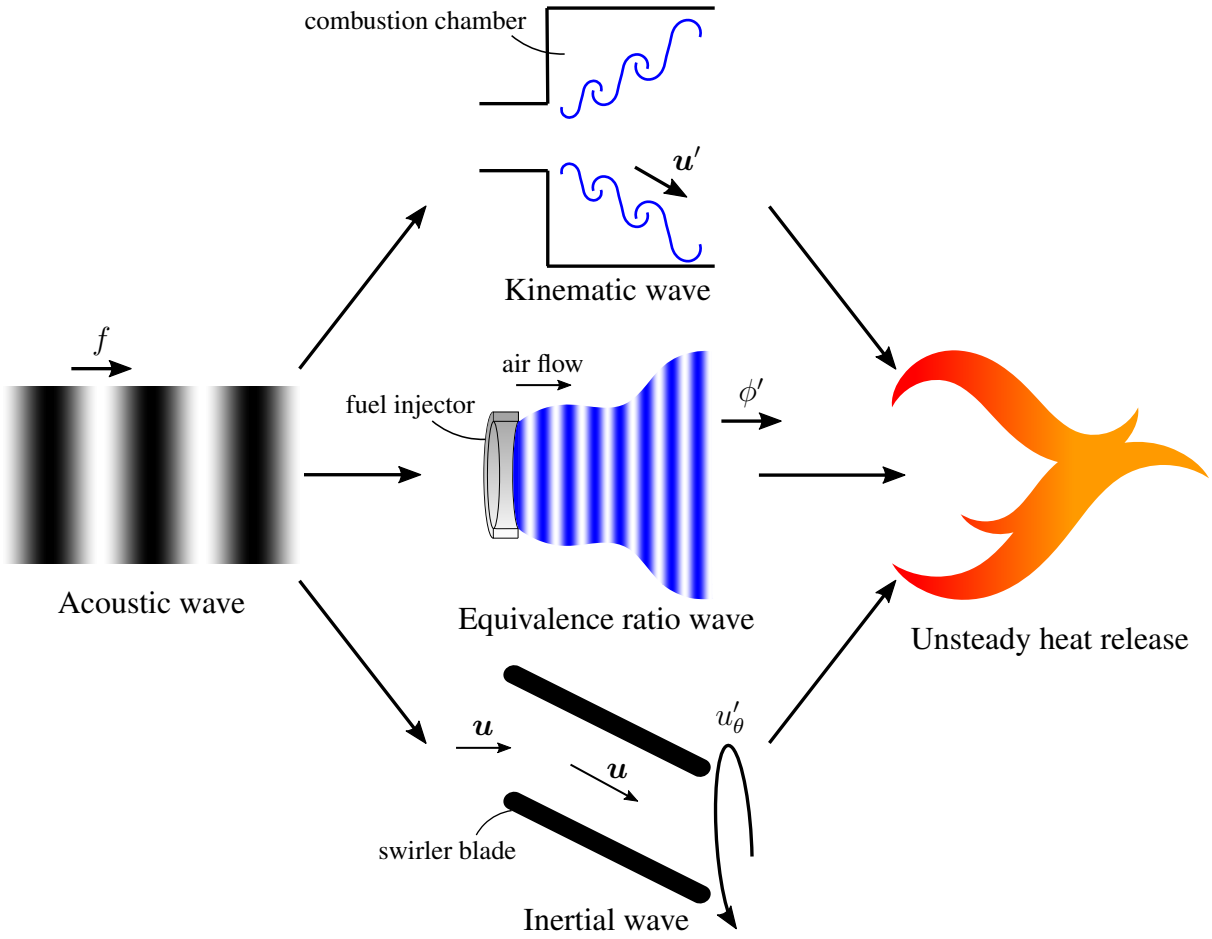

Figure 1.1: Schematic illustration of major flame response mechanisms in technically premixed swirl stabilized flames. Incident plane acoustic waves that propagate downstream (f-wave) are shown in the left image. The flame image on the right part indicates the unsteady heat release rate. Mode conversion processes stemming from acoustic waves are sketched in the middle column. A combustion chamber dump plane is shown in the top image. Via mode conversion, kinematic waves are generated, which modulates the flame surface area. A fuel injector is shown in the center, which illustrates the generation of equivalence ratio waves. The corresponding flame response mechanism is discussed in Chapter 6. In the bottom image, swirler blades are drawn to demonstrate the generation of inertial waves. Inertial waves modulate the flame surface area similar to kinematic waves.

from upstream is considered. As illustrated in Fig. 1.2, three different operating conditions are studied, i.e. 1) perfectly premixed condition, 2) technically premixed condition with fuel injection close to the flame and 3) technically premixed condition with fuel injection far from the flame. In the first configuration, only the flame response due to flame front kinematics is active. The well-known $n-\tau$ model by Crocco and Cheng [9] is employed to describe the flame transfer function, which reads as

$$F(\omega) = N \exp(-i\omega\tau_f) \,, \tag{1.2}$$

where N is the amplification factor and τ_f is the flame time scale, i.e. the delay between the

unsteady heat release rate and the acoustic velocity. For simplicity, the flame time scale is normalized, hence $\tau_f = 1$. Similarly, a unity amplification $N = 1$ is considered. Note that, the acoustic time delay from the source to the flame is not introduced, since it is negligible for acoustically compact elements. For the second and third cases, the flame response to equivalence ratio waves needs to be considered. This is achieved by employing combined $n - \tau$ model, i.e.

$$F(\omega) = N \exp(-i\omega\tau_f) + N_\phi \exp(-i\omega(\tau_\phi + \tau_f)) \tag{1.3}$$

where N_ϕ is the amplification factor caused by equivalence ratio waves and τ_ϕ is the convective time delay from the fuel injector to the flame. Again, for simplicity, a unity amplification factor $N_\phi = -1$ is assumed. The negative sign is due to the mode conversion process, i.e. $\phi' = -u'$. This is explained in Sec. 6.1 in more detail. Moreover, τ_f is assumed to be the same for both types of perturbation. The distance between the fuel injector to the flame base is decisive for τ_ϕ. In the second case, the length is chosen such that $\tau_\phi = 1$. For the third case, it is $\tau_\phi = 2$. The flame transfer functions are shown in Fig. 1.2 as Bode plots. For the first case, a constant gain of unity and a linearly decaying phase are observed. For the other two cases, the oscillatory gain pattern is observed. This is explained by the superposition between different flame response mechanisms. For the second case, at even multiples of π the superposition of two contributions is destructive, and thus low gain values appear. At these frequencies, phase jumps by π are observed. Conversely, at odd multiples of π the constructive superposition is observed, which results in high gain values around 2. For the third case, similar behavior is observed. However, the frequencies are shifted, since the time delay, τ_ϕ, is doubled. An erroneous or inaccurate estimation of time scales may cause a very different flame transfer function behavior. Thus, the correct estimation of time scales is very important for thermo-acoustics. For inertial waves, analogous analysis may be developed by moving the swirler.

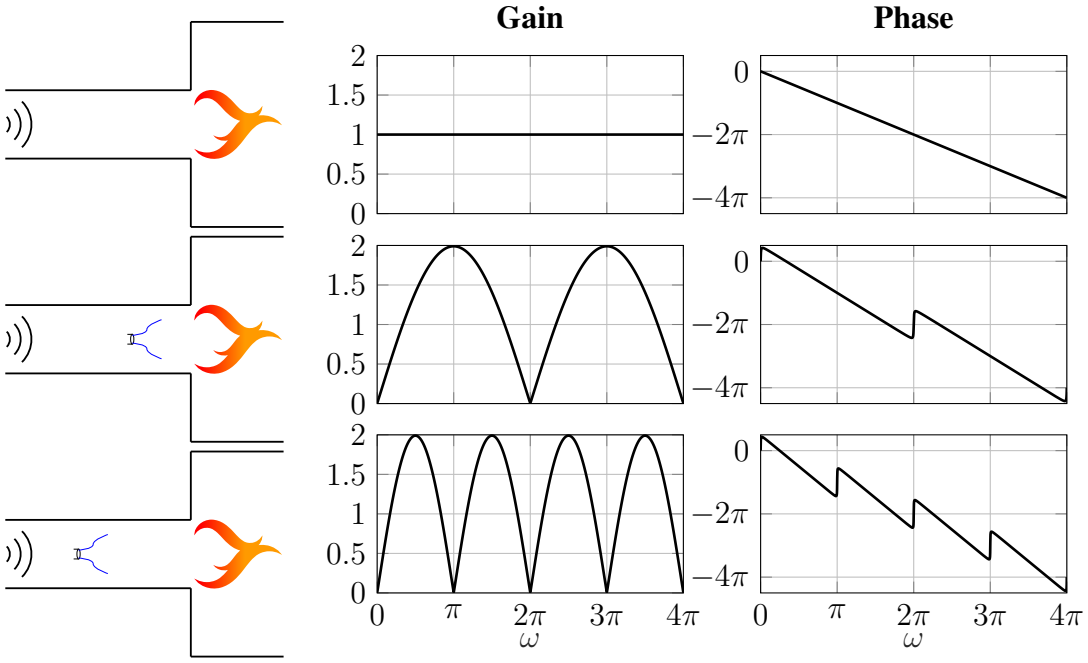

Figure 1.2: Left: Toy model flame configurations (top: perfectly premixed, center: technically premixed with shorter distance, and bottom: technically premixed with longer distance). Right: Corresponding flame transfer functions as Bode plots.

Usually, high fidelity numeric approaches are employed to achieve a quantitative agreement in the flame response (see for example [10, 11]). However, these numeric simulations are computationally expensive and therefore low order flame transfer function models are devised. These models aim at qualitative agreement, but also physical interpretation of relevant flame dynamics. This thesis focuses on low order models, particularly on identifying relevant time delays of perturbation mechanisms and how they affect the flame response. Contributions are made to both mechanisms, i.e. inertial and equivalence ratio waves. In this introduction, corresponding wave mechanisms are very briefly mentioned in the following paragraphs. For better readability, more complete discussions with relevant literature survey are presented in the beginning of the corresponding chapters (see Chapter 5 for inertial waves and Chapter 6 for equivalence ratio waves).

Inertial waves are commonly known as *swirl waves* in the thermo-acoustic community. However, in this thesis, the former designation is preferred and the reason is clarified in the following discussion. To the author's knowledge, Richards and co-workers [12, 13] were the first to mention tangential velocity fluctuations emitted from the swirler that modulate the heat release rate. By varying the swirler position, considerable changes in combustor pressure levels were observed. The generation of these waves was modeled via actuator disk theory by Cumpsty and Marble [14], Palies *et al.* [15]. This is illustrated in the lower part of Fig. 1.1 by blades of an axial swirler. The stream-wise propagation of these perturbations is commonly assumed to be convective. However, recent experimental and numerical studies from different research groups [16–18] suggested that these waves propagate around 40-50% faster than the mean flow speed. This puzzling result causes strong mismatches in the estimation of flame transfer functions unless ad-hoc corrections are provided. In this thesis, by employing linearized Euler equations for a rotating flow as pioneered by Kelvin [19], these waves are designated as inertial waves. Owing to the dispersive nature of propagation, the deviation from the convective propagation is explained. Thus, it is emphasized that inertial waves are relevant for thermo-acoustics.

The other focus of the thesis is equivalence ratio waves. The impact of mixture inhomogeneities on combustion instabilities was recognized back in the 1980s by Keller *et al.* [20] for gas turbines. Lieuwen and Zinn [21] demonstrated that acoustic perturbations across the fuel injector generate convective equivalence ratio waves. This generation mechanism is shown in the middle part of Fig. 1.1 as a schematic illustration of a fuel jet surrounded an air stream. Later, low order models were devised to explain the underlying flame response mechanisms. In Chapter 6, these are discussed in detail. In this thesis, by employing a time domain approach, a physics-based interpretation of flame response mechanisms is introduced, which emphasizes the importance of relevant time scales. Moreover, improvements to the low order flame response model are made.

Five publications are presented in this work. Two publications (Paper IW-Speed and Paper IW-Flame) contribute to the inertial wave subject. The assumption of convective propagation is scrutinized in the non-peer reviewed Paper IW-Speed. The deviation in the propagation speed is explained via dispersive inertial wave propagation. In Paper IW-Flame, the flame response caused by inertial waves are investigated. For an axisymmetric flame, tangential velocity fluctuations generate no heat release rate. The flame response mechanism is explained by the stream-wise and radial velocity fluctuations that are identified from inertial wave eigenmodes. Other two publications (Paper ϕ'-Flame and Paper Local-ϕ') contribute to the equivalence ratio wave subject. In Paper ϕ'-Flame, the time domain representation of the flame impulse response to

equivalence ratio waves is analytically derived. Relevant time scales are discussed and the impact of species diffusion on the flame response is introduced. In Paper Local-ϕ', the analytical framework of the previous publication is extended to account for non-uniform mixture inhomogeneities. This serves as a more realistic model for technically premixed flame configurations. In the final publication (Paper Scaling), the impact of time scales on combustor pressure levels is demonstrated in a lab scale bluff body stabilized perfectly premixed swirl flame. Experiments were conducted a decade ago and several papers were published since then by Tay-Wo-Chong *et al.* [11], Komarek and Polifke [16]. By modifying the swirler position or varying the mass flow rate, strong changes in pressure fluctuation levels and also in dominant oscillation frequency were observed. In Paper Scaling, a convective scaling law for the dominant frequency is introduced, i.e. the frequency changes approximately linear with the convection speed in the mixing duct. For this scaling, the relevance of the superposition of different time scales is pointed out.

This thesis is structured as follows. In chapter 2, two mathematical tools that are relevant for the derivation are introduced, i.e. Sturm-Liouville theorem and the method of steepest descent. In chapter 3, a brief introduction to the linear hydrodynamic stability analysis is given. This analysis forms the mathematical basis to investigate the wave propagation, which is relevant for determining time delays. In chapter 4, a broad introduction to inertial waves in rotating flows is presented by emphasizing other research fields. More detailed introduction within the thermo-acoustic context is given in chapter 5 with relevant references. The actuator disk theory is revisited to explain the mode conversion process. Moreover, a novel analytical solution of the initial value problem is derived, where the response of a swirler to a step acoustic perturbation is considered. The resulting inertial wave structure is characterized. This solution serves as a time lag model to clarify the deviation in propagation speeds and also enlightens the flame response mechanism. In chapter 6, the equivalence ratio waves are discussed. The generation mechanism is revised and the propagation is characterized by employing the advection-diffusion equation. Similar to the inertial waves, the initial value problem is proposed. Moreover, flame response mechanisms are mentioned.

2 Mathematical Tools

In this chapter, two important mathematical tools are briefly introduced, which are necessary for deriving important outcomes for this thesis. In the following section, second order ordinary differential equations that satisfy the Sturm-Liouville conditions are discussed. Such equations can be solved as an eigenvalue problem and the solution forms an orthogonal eigenspace. This is relevant for inertial waves, i.e. the governing flow equations can be written in the Sturm-Liouville form as discussed in sections 4.2 and 5.2. In Sec. 4.2, the orthonogal eigenmode structures are revisited from Kelvin work [19]. In Sec. 5.2, tangential velocity fluctuations that are generated at the swirler are decomposed into these eigenmodes, which is required to characterize the propagation speed of inertial waves. In Sec. 2.2, the second important tool is presented, i.e. the method of steepest descent to estimate the asymptotic behavior of an integral. This method is employed for deriving the solution of initial value problem proposed in Sec. 5.2. A neat analytical expression is obtained for the inertial wave step response.

2.1 Sturm – Liouville Equation

A second order ordinary differential equation of the form

$$\frac{\mathrm{d}}{\mathrm{d}r}\left[a(r)\frac{\mathrm{d}f(r)}{\mathrm{d}r}\right] + \left[b(r) + \lambda w(r)\right] f(r) = 0 \ , \quad r \in [r_i, r_o] \tag{2.1}$$

is called Sturm-Liouville differential equation [22] if the following conditions are satisfied:

- In the given interval, $r \in [r_i, r_o]$, the functions $a(r)$, $\mathrm{d}a/\mathrm{d}r$, $b(r)$ and $w(r)$, are real and continuous.
- The functions $a(r)$ and $w(r)$ are positive for all r in the interval.
- The boundary conditions at r_i and r_o are separated, i.e.

$$\alpha_1 f(r_i) + \alpha_2 \frac{\mathrm{d}f(r_i)}{\mathrm{d}r} = 0 \ , \tag{2.2}$$

$$\alpha_3 f(r_o) + \alpha_4 \frac{\mathrm{d}f(r_o)}{\mathrm{d}r} = 0 \ . \tag{2.3}$$

  where $\alpha_1^2 + \alpha_2^2 > 0$ and $\alpha_3^2 + \alpha_4^2 > 0$.

With these assumptions, a Sturm-Liouville equation is considered as an eigenvalue problem. Infinitely many unique eigenvalues, λ_n, exist, which can be ordered as

$$\lambda_1 < \lambda_2 < \ldots < \lambda_n < \ldots \to \infty \ . \tag{2.4}$$

For each eigenvalue there exists an eigenmode $f_n(r)$, which satisfies the differential equation and the boundary conditions. The eigenmodes form an orthonormal basis, i.e.

$$\int_{r_i}^{r_o} f_n(r) f_m(r) w(r) \mathrm{d}r = \begin{cases} 1, & \text{if } m = n \\ 0, & \text{if } m \neq n \end{cases} \tag{2.5}$$

This is a powerful outcome and is useful for characterizing differential equations. Any solution of this differential equation that satisfies the boundary conditions can be written as a sum of the orthonogal eigenmodes.

Here, a simple example is demonstrated. The solution of the following differential equation is sought

$$\frac{\mathrm{d}^2 f(r)}{\mathrm{d}r^2} + \lambda f(r) = 0 \ , \tag{2.6}$$

where $f(r)$ and λ are unknowns. The boundary conditions are

$$f(0) = 0 \ , \tag{2.7}$$
$$f(\pi) = 0 \ . \tag{2.8}$$

Note that this differential equation satisfies the Sturm-Liouville conditions by setting $a(r) = w(r) = 1$, $b(r) = 0$, $r_i = 0$, $r_o = \pi$, $\alpha_1 = \alpha_3 = 1$ and $\alpha_2 = \alpha_4 = 0$. The solution of the differential equation reads

$$f(r) = a \sin\left(\sqrt{\lambda} r\right) + b \cos\left(\sqrt{\lambda} r\right) \ . \tag{2.9}$$

By applying the boundary condition at $r = 0$, the prefactor is set to $b = 0$, since $\cos(0) = 1$. The other boundary condition at $r = \pi$, gives the following relation

$$a \sin\left(\sqrt{\lambda}\pi\right) = 0 \ . \tag{2.10}$$

The eigenvalues are identified from the solution of this equation, i.e.

$$\lambda_n = n^2 \ , \tag{2.11}$$

where n stands for positive natural numbers. The orthogonal eigenmodes then read as

$$f_n(r) = \sin(n\pi) \ . \tag{2.12}$$

2.2 Method of Steepest Descent

For integrals of the form

$$I(z) = \int_C f(k) e^{zg(k)} \mathrm{d}k \ , \tag{2.13}$$

where $k \in \mathbb{C}$ and $z \in \mathbb{R}$, the method of steepest descent determines the asymptotic behavior of the integral for $z \to \infty$. For a detailed introduction on this subject, the reader may refer to the textbook by Bender and Orszag [23]. The functions, $f(k)$ and $g(k)$, are assumed to be analytic in the integration path, C. The saddle point, k_0, of the exponent function, $g(k)$, is found by

$$\left.\frac{\partial g}{\partial k}\right|_{k=k_0} = 0 \ . \tag{2.14}$$

If this saddle point is a local maximum of $\mathrm{Re}(g(k))$, the steepest descent path, C', indicates the most rapidly decaying path emanating from k_0. As a result of Cauchy-Riemann equations, this path is found by following the constant imaginary part, $\Im(g(k_0))$. In the limit of $z \to \infty$, the contribution around the saddle point is the leading order for the integral, since the real part is maximum. The steepest descent path is approximated by a tangent line at the saddle point as

$$k(s) = k_0 + se^{i\theta} \ , \tag{2.15}$$

where θ indicates the angle of C' at k_0. The order of the steepest descend, $N-1$, indicates

$$\left.\frac{\partial g}{\partial k}\right|_{k=k_0} = \left.\frac{\partial^2 g}{\partial k^2}\right|_{k=k_0} = ... = \left.\frac{\partial^{N-1} g}{\partial k^{N-1}}\right|_{k=k_0} = 0 \text{ and } \left.\frac{\partial^N g}{\partial k^N}\right|_{k=k_0} \neq 0 \ . \tag{2.16}$$

The functions, $f(k)$ and $g(k)$, can be approximated as

$$f(k) \approx f(k_0) \ , \tag{2.17}$$

$$g(k) \approx g(k_0) + \Phi s^N \ , \tag{2.18}$$

where Φ is determined from the Taylor series expansion as

$$\Phi = \frac{e^{iN\theta}}{N!} \left.\frac{\partial^N g}{\partial k^N}\right|_{k=k_0} \ . \tag{2.19}$$

The angle of the steepest descent, θ, is determined by

$$\theta = -\frac{1}{N} \arg\left(\frac{\partial^N g}{\partial k^N}\right) + \frac{2n+1}{N} \ , \quad n = 0, 1, 2, ..., N-1 \ . \tag{2.20}$$

The asymptotic behavior of the integral can be simplified as

$$I(z) \approx f(k_0) e^{zg(k_0)+i\theta} \int_{-\infty}^{\infty} e^{z\Phi s^N} \mathrm{d}s \ . \tag{2.21}$$

Since the path follows the steepest descent, the real part is always negative, i.e. $\mathrm{Re}(\Phi) < 0$. This means that the integral is convergent and for simple saddle point ($N = 2$) the approximate integral reads

$$I(z) \approx f(k_0) e^{zg(k_0)+i\theta} \sqrt{-\frac{\pi}{z\Phi}} \ . \tag{2.22}$$

Here, the integral for the Airy function is demonstrated as an example. The Airy function is defined as the following integral

$$I(z) = \frac{1}{2\pi} \int_{-\infty}^{\infty} e^{i\left(\frac{k^3}{3}+zk\right)} \mathrm{d}k \ . \tag{2.23}$$

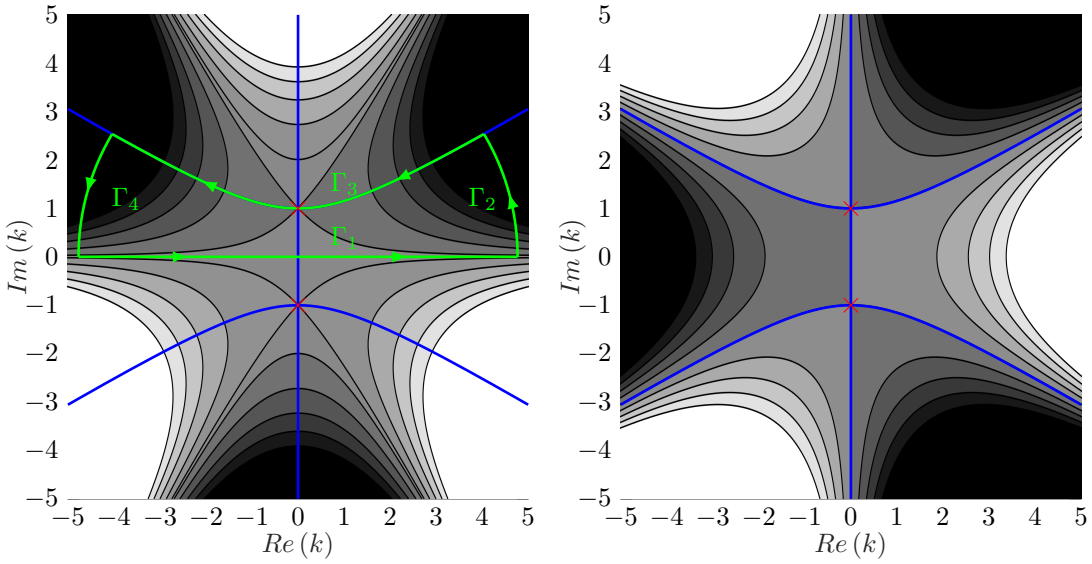

Figure 2.1: For $z = 1$, the contour plot of the real (left) and imaginary (right) part of the integrand is shown. In the gray scale, darker colors indicate lower values. Black lines correspond to constant levels of the plotted variable. Red crosses are saddle points. Blue lines indicate constant levels of the imaginary part of the integrand at saddle points. Green lines indicate the contour integral formed via method of steepest descent.

No closed form solution exists for this integral and the asymptotic behavior for large z is investigated.

The functions, $g(k)$ and $f(k)$, read as

$$g(k) = i\left(\frac{k^3}{3z} + k\right) \quad , \quad f(k) = \frac{1}{2\pi} \, . \tag{2.24}$$

The real and imaginary part of the integrand are shown in Fig. 2.1 for $z = 1$. There exist two simple saddle points at $k_0 = \pm i\sqrt{z}$, which are shown in the figure with red crosses. Only the upper saddle point, $k_0 = i\sqrt{z}$, is a steepest descent, since it is a local maximum for the real part. Hence, the lower saddle point is not used to form the integral path. Blue lines indicate the constant level of the imaginary part at the saddle points. The steepest descent path, Γ_3, is indicated with the green color. This path is parallel to the real axis at the saddle point, i.e. $\theta = 0$. The series expansion for the exponential function at the saddle point reads

$$g(k) \approx -\frac{2\sqrt{z}}{3} - \frac{s^2}{\sqrt{z}} \, . \tag{2.25}$$

Note that the function, $f(k)$, does not depend on k for this particular problem and thus it is not necessary to employ a series expansion. The integral along the steepest descent path, Γ_3, is approximated as

$$S(z) = \int_{\Gamma_3} f(k) e^{zg(k)} \mathrm{d}k \approx -\frac{e^{-\frac{2}{3}z^{3/2}}}{2\sqrt{\pi} z^{1/4}} \, . \tag{2.26}$$

To find an approximation for $I(z)$, the initial integral path, $\Gamma_1 = (-\infty, \infty)$, is connected to Γ_3 via two semi circles, Γ_2 and Γ_4. These paths are shown in Fig. 2.1 with green lines. The integral along this closed path reads

$$\underbrace{\int_{\Gamma_1}}_{I(z)} + \underbrace{\int_{\Gamma_2} + \int_{\Gamma_4}}_{C(z)} + \underbrace{\int_{\Gamma_3}}_{S(z)} = 0 \,, \tag{2.27}$$

where the Cauchy's integral theorem is employed, i.e. the integral along a closed path with no singularities is zero. One can show that the integrals along Γ_2 and Γ_4 vanish as the radius of the semicircle increase, i.e. $C(z) = 0$. Finally, the asymptotic behavior of the integral is $I(z) = -S(z)$, i.e.

$$I(z) \approx \frac{e^{-\frac{2}{3}z^{3/2}}}{2\sqrt{\pi}z^{1/4}} \,. \tag{2.28}$$

The Airy function is shown in Fig. 2.2. As expected the asymptotic approximation shows good agreement only for large z.

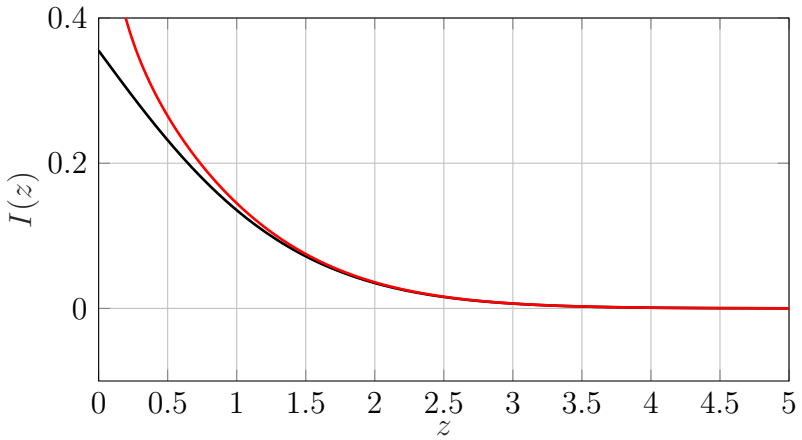

Figure 2.2: Comparison of the Airy function (black) against the asymptotic approximation via method of steepest descent (red).

3 Hydrodynamic Stability Analysis

Hydrodynamic stability analysis is a prominent subject in fluid dynamics. Formally, it deals with the growth of infinitesimal perturbations in laminar flow. The analysis is relevant for fluid systems, where unsteady flow structures and the transition to turbulence are important. It is worth to mention the initiators of hydrodynamic stability analysis with their canonical examples, i.e. Kelvin-Helmholtz instability in two parallel streams with different speeds named after Helmholtz [24] and Kelvin [25], centrifugal instability in rotating annular flow by Rayleigh [26] and the transition to turbulence in a straight pipe flow by Reynolds [27]. For a comprehensive introduction to the subject, books from Drazin and Reid [28], Chandrasekhar [29] can be recommended.

In the hydrodynamics stability analysis, the behavior of Navier-Stokes equations to small perturbations is considered. A commonly employed approach is the linear analysis due to its simplicity. After 1960s, the non-linear approaches have been developed extensively. In this thesis, the analysis is restricted only to the linear theory, since wave structures are easily characterized within the linear framework. Indeed, the main focus of this work is to determine the wave propagation rather than quantifying instabilities.

In the following section, the main steps of the linear stability analysis are briefly formalized. Then, its application is demonstrated on the famous example of transition to turbulence in a plane Poiseuille flow in Sec. 3.2. The temporal stability analysis is performed to estimate the critical Reynolds number, which predicts linear instability. Then, in Sec. 3.3, the inviscid centrifugal instability is discussed, since it is tightly related to inertial waves.

3.1 Linear Normal Mode Formalism

The starting point is the incompressible Navier-Stokes equations in non-dimensional form, which read as

$$\frac{\partial \boldsymbol{u}}{\partial t} + \boldsymbol{u} \cdot \boldsymbol{\nabla} \boldsymbol{u} = -\boldsymbol{\nabla} p + \frac{1}{\mathrm{Re}} \Delta \boldsymbol{u} \ , \tag{3.1}$$

$$\boldsymbol{\nabla} \cdot \boldsymbol{u} = 0 \ . \tag{3.2}$$

First, a steady base flow field is required. Analytical expressions can be found for idealized cases, such as the Poiseuille flow and the Taylor-Couette flow. For more realistic configurations, a numerical simulation is often employed. Formally, the base flow is found by solving the steady Navier-Stokes equations, which read

$$\bar{\boldsymbol{u}} \cdot \boldsymbol{\nabla} \bar{\boldsymbol{u}} = -\boldsymbol{\nabla} \bar{p} + \frac{1}{\mathrm{Re}} \Delta \bar{\boldsymbol{u}} \ , \tag{3.3}$$

$$\boldsymbol{\nabla} \cdot \bar{\boldsymbol{u}} = 0 \ , \tag{3.4}$$

where $\bar{(\cdot)}$ denotes steady quantities. The next step is to linearize the equations around the base flow. The linearization represents an infinitesimal perturbation to the mean flow, i.e.

$$\boldsymbol{u} = \bar{\boldsymbol{u}} + \varepsilon \boldsymbol{u}' \ , \tag{3.5}$$

where ε is an infinitesimally small factor and $(\cdot)'$ indicates perturbations. For the linearization, second and higher order terms for ε are neglected. The resulting equations for the order of ε read

$$\frac{\partial \boldsymbol{u}'}{\partial t} + \bar{\boldsymbol{u}} \cdot \boldsymbol{\nabla} \boldsymbol{u}' + \boldsymbol{u}' \cdot \boldsymbol{\nabla} \bar{\boldsymbol{u}} = -\boldsymbol{\nabla} p' + \frac{1}{\mathrm{Re}} \Delta \boldsymbol{u}' \ , \tag{3.6}$$

$$\boldsymbol{\nabla} \cdot \boldsymbol{u}' = 0 \ . \tag{3.7}$$

Very first attempts were to analyze parallel infinite flows with 1-d base flows, i.e. $\bar{\boldsymbol{u}}(x, y, z) = \bar{u}_z(y)$. Here, z axis indicates the fluid flow direction. The flow velocity varies with the y axis and the configuration is assumed to be infinitely long in the x axis. For such flows, the normal mode ansatz is employed for the perturbed quantities as

$$\boldsymbol{u}'(t, x, y, z) = \hat{\boldsymbol{u}}(y) \mathrm{e}^{-i\omega t + ik_x x + ik_z z} \ . \tag{3.8}$$

This step simplifies partial derivatives into algebraic terms, e.g. $\frac{\partial \boldsymbol{u}'}{\partial t} = i\omega \hat{\boldsymbol{u}}$. The final expression is an ordinary differential equation with respect to y and the unknowns are the angular frequency, ω, and wave numbers, k_x and k_z, which are determined as an eigenvalue problem. The modal ansatz approach is also called as *local* stability analysis. Two methods, namely *temporal* and *spatial* stability analysis, are commonly employed to solve the eigenvalue problem. For the temporal analysis, the complex angular frequency, ω, is determined for given real wave numbers, k_x and k_z. If the imaginary part of the angular frequency is positive, then perturbations grow and the flow is temporally unstable. The spatial analysis follows the opposite approach, i.e. the complex wave numbers are determined for a real angular frequency. In this case, the instability is recognized by the imaginary part of wave numbers. The Briggs-Bers criterion [30, 31] distinguishes between convective and absolute instabilities. The convective instability indicates that perturbations grow but propagate only in the downstream direction, whereas perturbations in an absolute instability grow in both directions. Besides the characterization of stability, the normal mode ansatz introduces traveling waves. The dispersion relation is formed by writing the angular frequency as a function of wave number, i.e. $\omega(k)$. Two important quantities are then introduced, namely the phase speed, c_p, and the group speed, c_g, which are defined as

$$c_p = \frac{\omega}{k} \ , \qquad c_g = \frac{\partial \omega}{\partial k} \ . \tag{3.9}$$

Wave crests move with the phase speed while the envelope of wave moves with the group speed. A wave is called dispersive if $c_p \neq c_g$. The dispersion relation of inertial waves are discussed in Sec. 4.2.

The local analysis is not adequate for non-parallel flows. An extension to the linear stability analysis is proposed by Pierrehumbert and Widnall [32]. The modal ansatz for the space is relaxed as

$$\boldsymbol{u}'(t, x, y, z) = \hat{\boldsymbol{u}}(x, y, z) \mathrm{e}^{-i\omega t} \ . \tag{3.10}$$

In this case, the eigenvalue problem is only solved for ω and corresponding eigenmodes $\hat{\boldsymbol{u}}(x, y, z)$ are found numerically. This approach is called global stability analysis. With the increasing computational power in last decades, this approach became more attractive than the local analysis.

3.2 Stability of Plane Poiseuille Flow

The modal decomposed linearized Navier-Stokes equations for a parallel 1-d base flow can be simplified to the Orr-Sommerfeld equation [33], which reads as

$$\left[(-i\omega + ik_z\bar{u}_z)\left(\frac{\mathrm{d}^2}{\mathrm{d}y^2} - k_z^2\right) - ik_z\frac{\mathrm{d}^2\bar{u}_z}{\mathrm{d}y^2} - \frac{1}{\mathrm{Re}}\left(\frac{\mathrm{d}^2}{\mathrm{d}y^2} - k_z^2\right)^2\right]\hat{u}_y = 0\ , \tag{3.11}$$

where the base velocity of a laminar flow between infinitely long parallel walls is given as $\bar{u}_z = 1 - y^2$. The non-dimensionalized configuration is shown in Fig. 3.1.

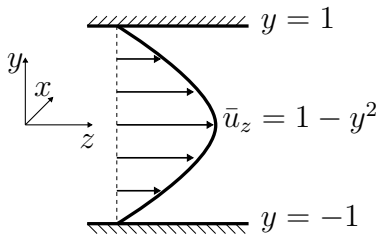

Figure 3.1: Schematic illustration of Poiseuille flow.

No-slip boundary conditions are applied for the perturbed velocity at both walls, i.e. $\hat{u}_y(-1) = \hat{u}_y(1) = 0$. Here, the temporal analysis is performed for the eigenvalue problem following Orszag [34]. As discussed in Sec. 3.1, the wavenumber k_z is assumed to be real. The differential operator $\mathrm{d}/\mathrm{d}y$ is discretized by employing Chebyshev polynomials. The maximum of the growth rate, i.e. the imaginary part of the angular frequency, $\max(\Im(\omega))$, is plotted against the wavenumber for three different Reynolds numbers, $\mathrm{Re} = [3000, 5772.22, 8000]$, in Fig 3.2. As discussed by Orszag [34], the critical Reynolds number is $\mathrm{Re} = 5772.22$, for which the maximum growth rate crosses the zero line. The flow is linearly unstable for higher values. Although the Orr-Sommerfeld equation is famous in literature, it does not capture the correct physics. In experiments, the transition to turbulence occurs at much lower Reynolds numbers around $\mathrm{Re} = 2000$. The discrepancy comes from the transient growth due to the non-normal eigenmodes as discussed in Schmid and Henningson [35]. This growth triggers non-linear behavior of fluids, which is neglected in the linear analysis.

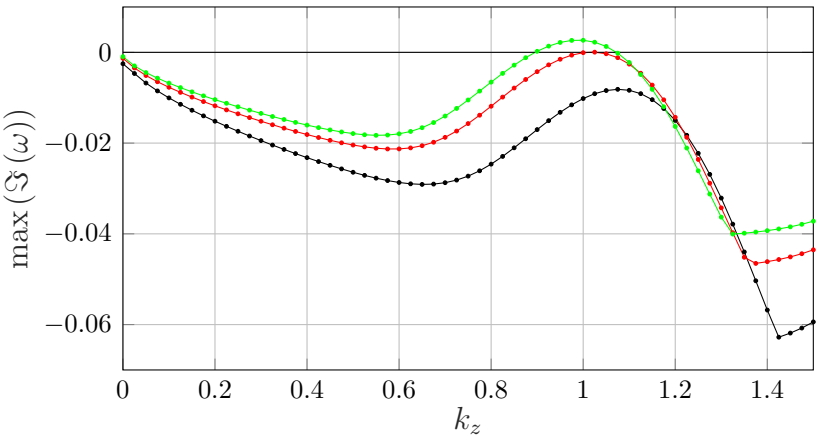

Figure 3.2: Maximum of the growth rate, $\max(\Im(\omega))$, as a function of wave number, k_z, for three Reynolds numbers: Re $= 3000$ (black), 5772.22 (red) and 8000 (green).

3.3 Inviscid Centrifugal Instability

Rayleigh [26] derived the condition for the inviscid centrifugal instability by physically interpreting two fluid particles at different radial positions, say r_1 and r_2 with $r_2 > r_1$ that swap their positions. The conservation of the angular momentum implies that the quantity $H \equiv ru_\theta$ is conserved. The total kinetic energy per volume at the initial state is

$$e_1 = \frac{1}{2}\rho\left(\frac{H_1^2}{r_1^2} + \frac{H_2^2}{r_2^2}\right) . \tag{3.12}$$

After the swap, keeping their angular momentum, the energy becomes

$$e_2 = \frac{1}{2}\rho\left(\frac{H_2^2}{r_1^2} + \frac{H_1^2}{r_2^2}\right) . \tag{3.13}$$

The difference in energy, $\Delta e = e_2 - e_1$, is

$$\Delta e = \frac{1}{2}\rho\left(H_2^2 - H_1^2\right)\left(\frac{1}{r_1^2} - \frac{1}{r_2^2}\right) . \tag{3.14}$$

For an instability, the energy should be released, thus $H_1^2 > H_2^2$. This means that the quantity, H^2, should decrease radially, i.e. $\mathrm{d}H^2/\mathrm{d}r < 0$. The famous Rayleigh criterion for centrifugal instability is

$$\frac{\mathrm{d}(r^2u_\theta^2)}{\mathrm{d}r} < 0 . \tag{3.15}$$

The solid body rotation, $u_\theta = Kr$, does not satisfy this condition, thus is always stable. The marginally stable profile is the free vortex solution, $u_\theta = K/r$. A profile with $u_\theta = K/r^n$, where $n > 1$, is always unstable.

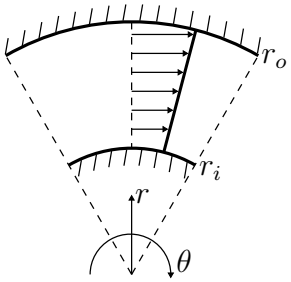

Figure 3.3: Schematic illustration of Taylor-Couette flow.

A more rigorous proof can be achieved by linear stability analysis as described in Sec. 3.1. An arbitrarily rotating base flow $\bar{u}_\theta(r)$ in an annular duct with inner and outer walls respectively at r_i and r_o is considered, see Fig. 3.3. Modal decomposed linearized Euler equations in cylindrical coordinates can be simplified as

$$\frac{\mathrm{d}}{\mathrm{d}r}\left(\frac{1}{r}\frac{\mathrm{d}(r\hat{u}_r)}{\mathrm{d}r}\right) - k^2\hat{u}_r = -\frac{k^2}{\omega^2 r^3}\frac{\mathrm{d}(r^2\bar{u}_\theta^2)}{\mathrm{d}r}\hat{u}_r \ . \tag{3.16}$$

By multiplying this equation with $r\hat{u}_r^\dagger$, where $\dagger$ indicates the complex conjugate, and integrating along radial boundaries yields

$$\int_{r_i}^{r_o} \frac{1}{r}\left|\frac{\mathrm{d}(r\hat{u}_r)}{\mathrm{d}r}\right|^2 \mathrm{d}r + k^2\int_{r_i}^{r_o} r\left|\hat{u}_r\right|^2 \mathrm{d}r = \frac{k^2}{\omega^2}\int_{r_i}^{r_o} \frac{1}{r^2}\frac{\mathrm{d}(r^2\bar{u}_\theta^2)}{\mathrm{d}r}\left|\hat{u}_r\right|^2 \mathrm{d}r \ . \tag{3.17}$$

Note that the integrals on the left hand side are always positive. The temporal instability is observed for $\Im(\omega) > 0$. This is realized if the integral in the right hand side integral is negative, i.e. the condition in Eq. (3.15). This is in line with the interpretation by Rayleigh.

4 Inertial Waves in Rotating Flows

Before the discussion of inertial waves in the context of thermo-acoustics, it is instructive to overview the fundamentals of inertial waves. The intent is not to give a complete description and the reader may refer to standard textbooks by Greenspan [36], Landau and Lifshitz [37], Pedlosky [38]. As pioneered by Kelvin [19] in 1880, inertial waves are a phenomenon in rotating fluids and commonly observed in astro- and geophysics. First laboratory examples of plane inertial waves were devised in 1960s by Oser Hansjörg [39], Fultz [40], McEwan [41]. However, only recently accurate PIV measurements were conducted by Messio *et al.* [42], Cortet *et al.* [43]. To give the reader an impression of the diversity of the inertial wave research, the Rossby waves [44], a subset of inertial waves, are briefly mentioned here. These waves are governed by the restorative Coriolis force due to the Earth's rotation and have a strong impact on the climate by affecting jet stream paths and locations of high and low pressure areas. The sketch in the left part of Fig. 4.1 illustrates eastward propagating jet streams that form a boundary between the hot and cold air on Northern Hemisphere. Meanders are denoted as Rossby waves. Analogous structures are reproduced in lab scale experiments with a rotating cylindrical tank. An exemplary setup is given in the right part of the Fig. 4.1, where similar meander structures are observed in the dye color.

In Sec. 4.1, fundamental plane inertial waves are discussed using the linear hydrodynamic stability formalism from Sec. 3.1. In plane waves, boundary effects are not present. Then, in Sec. 4.2, Kelvin waves, named after work by Kelvin [19], in bounded vortex cores are discussed. Non-planar waves are observed in the presence of boundary effects. These wave modes are used in Chapter 5 to describe the inertial wave propagation downstream of a swirler.

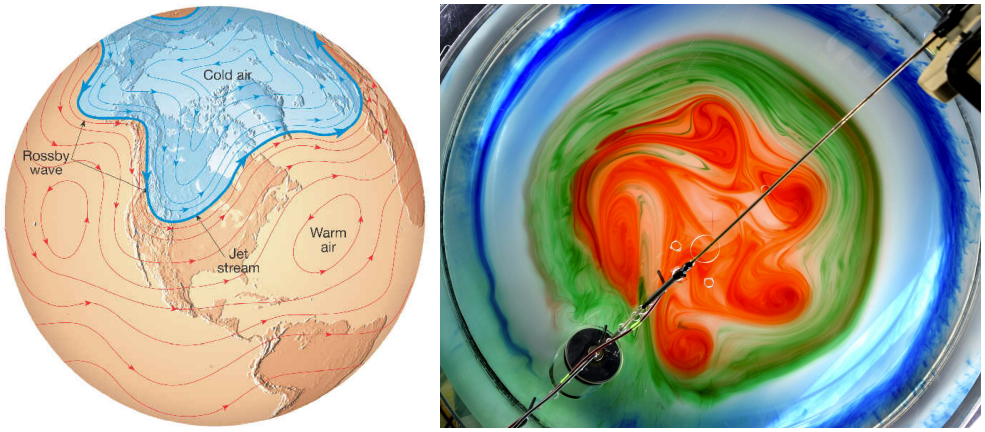

Figure 4.1: Left: Atmospheric Rossby waves in Northern hemisphere. (Image from Department of Geography and computer science, CUNY [45]) Right: Picture of Rossby waves excited by oscillating plunger in a rotating cylindrical tank filled with water (taken from Rhines [46]). Dye is used to identify meandering structures.

4.1 Plane waves

Inertial waves are oscillatory circular flow motions, where the Coriolis force acts as the restoring force. To demonstrate the impact of the Coriolis force, a generic example of plane inertial waves in an unbounded domain is discussed. An inviscid incompressible fluid with a solid body rotation is considered. It is preferred to write the governing fluid equations in the rotating frame of reference, since the fictitious Coriolis force becomes apparent. The velocity vector $\boldsymbol{u}$ in the inertial frame is related to the rotating frame velocity, $\boldsymbol{u}_R$, as

$$\boldsymbol{u} = \boldsymbol{u}_R + (\boldsymbol{\Omega} \times \boldsymbol{r}) \ , \tag{4.1}$$

where $\boldsymbol{\Omega}$ is the angular velocity vector of the rotating system and $\boldsymbol{r}$ is the position vector from the origin of the rotation. The Navier-Stokes equations in rotating coordinates are

$$\boldsymbol{\nabla} \cdot \boldsymbol{u}_R = 0 \ , \tag{4.2}$$

$$\frac{\partial \boldsymbol{u}_R}{\partial t} + (\boldsymbol{u}_R \cdot \boldsymbol{\nabla})\, \boldsymbol{u}_R - \nu \boldsymbol{\nabla}^2 \boldsymbol{u}_R + \frac{1}{\rho} \boldsymbol{\nabla} p_r = -2\boldsymbol{\Omega} \times \boldsymbol{u}_R \ , \tag{4.3}$$

where ν is the kinematic viscosity and ρ is the density. The continuity equation does not change in the rotating frame. In the momentum equation, the right hand side term is the Coriolis force. Note that the cross product indicates that the Coriolis force is always normal to the rotation axis and to the relative flow velocity. The other fictitious force, i.e. the centrifugal force, can be included in the pressure term. The reduced pressure, p_r, reads as

$$p_r = p - 0.5\rho\, (\boldsymbol{\Omega} \times \boldsymbol{r})^2 \ . \tag{4.4}$$

Note that the original Navier-Stokes equations are recovered for the case of zero angular velocity, $\boldsymbol{\Omega} = 0$, where the Coriolis and the centrifugal forces vanish.

According to the Buckhingham π theorem, non-rotating incompressible flows are characterized by a single dimensionless parameter, i.e Reynolds number (Re). For rotating flows, two dimensionless parameters are required and commonly the Rossby (Ro) and Ekman (Ek) numbers are preferred. The former defines a measure between the inertial (advective) force and the Coriolis force and the latter relates the viscous force to the Coriolis force. Mathematically, they are defined as

$$\mathrm{Ro} = \frac{u_z}{\Omega D} \ , \qquad \mathrm{Ek} = \frac{\nu}{\Omega D^2} \ . \tag{4.5}$$

The Reynolds number is related to these parameters as $\mathrm{Re} = \mathrm{Ro}/\mathrm{Ek}$. The non-dimensional momentum equations in rotating coordinates are

$$\frac{\partial \boldsymbol{u}_R^*}{\partial t} + \mathrm{Ro}\, (\boldsymbol{u}_R^* \cdot \boldsymbol{\nabla})\, \boldsymbol{u}_R^* - \mathrm{Ek} \boldsymbol{\nabla}^2 \boldsymbol{u}_R^* + \boldsymbol{\nabla} p_r^* = -2\boldsymbol{e_z} \times \boldsymbol{u}_R^* \, , \tag{4.6}$$

where nondimensional parameters are indicated by $(\cdot)^*$. Without loss of generality, the direction of the rotation is set to the z direction (the unit vector $\boldsymbol{e}_z$), i.e. $\boldsymbol{\Omega} = \Omega \boldsymbol{e}_z$.

The inviscid assumption is realized by setting $\mathrm{Ek} = 0$. Since a flow dominated by the rotation is considered, the advective acceleration is also assumed to be negligible compared to the Coriolis force by setting $\mathrm{Ro} = 0$. Thus, the momentum equation reduces to

$$\frac{\partial \boldsymbol{u}_R}{\partial t} + \frac{1}{\rho} \boldsymbol{\nabla} p_r = -2\Omega \boldsymbol{e}_z \times \boldsymbol{u}_R \, . \tag{4.7}$$

By taking the curl of the momentum equation, the pressure is eliminated from the equation, which reads

$$\frac{\partial \left(\boldsymbol{\nabla} \times \boldsymbol{u}_R \right)}{\partial t} = 2\Omega \left(\boldsymbol{e}_z \cdot \boldsymbol{\nabla} \right) \boldsymbol{u}_R \, , \tag{4.8}$$

where the identity $\boldsymbol{\nabla} \times (\boldsymbol{e}_z \times \boldsymbol{u}_R) = \boldsymbol{e}_z \left(\boldsymbol{\nabla} \cdot \boldsymbol{u}_R \right) - \left(\boldsymbol{e}_z \cdot \boldsymbol{\nabla} \right) \boldsymbol{u}_R$ is employed. The first term on the right hand side vanishes due to the incompressibility. Then, the modal ansatz is introduced as

$$\boldsymbol{u}_R = \hat{\boldsymbol{u}}_R \exp(i\boldsymbol{k} \cdot \boldsymbol{r} - i\omega t) \, , \tag{4.9}$$

where $\boldsymbol{k}$ is the wave number vector and ω is the angular frequency. The continuity equation reduces to the following transversality condition

$$\boldsymbol{k} \cdot \hat{\boldsymbol{u}}_R = 0 \, , \tag{4.10}$$

which indicates that velocity perturbations are perpendicular to the wave number vector. The momentum equation with the modal ansatz yields

$$\omega \left(\boldsymbol{k} \times \hat{\boldsymbol{u}}_R \right) = 2\Omega i \left(\boldsymbol{e}_z \cdot \boldsymbol{k} \right) \hat{\boldsymbol{u}}_R \, . \tag{4.11}$$

Vector multiplication of this equation with $\boldsymbol{k}$ results in

$$-\omega |\boldsymbol{k}|^2 \hat{\boldsymbol{u}}_R = 2\Omega i \left(\boldsymbol{e}_z \cdot \boldsymbol{k} \right) \left(\boldsymbol{k} \times \hat{\boldsymbol{u}}_R \right) \, . \tag{4.12}$$

The above two equations are used to eliminate $\hat{\boldsymbol{u}}_R$ and the dispersion relation is derived as

$$\omega = \frac{2\Omega k_z}{|\boldsymbol{k}|} = 2\Omega \cos(\theta) \, , \tag{4.13}$$

where θ is the angle between $\boldsymbol{k}$ and $\boldsymbol{e}_z$. The relevant vectors are illustrated in the left part of Fig. 4.2. The dispersion relation indicates that the angle of the wave vector is determined from the frequency of oscillation and the angular velocity of the rotation. By substituting Eq. (4.13) into Eq. (4.11), one derives the relation

$$\boldsymbol{k} \times \hat{\boldsymbol{u}}_R = i |\boldsymbol{k}| \hat{\boldsymbol{u}}_R \, . \tag{4.14}$$

By decomposing the modal velocity into its real and imaginary parts, i.e. $\hat{\boldsymbol{u}}_R = \boldsymbol{a} + \boldsymbol{b}i$, one obtains $\boldsymbol{k} \times \boldsymbol{b} = |\boldsymbol{k}| \boldsymbol{a}$, which means that the magnitudes of the real and imaginary parts are equal, i.e. $|\boldsymbol{a}| = |\boldsymbol{b}|$. Moreover, they are perpendicular to each other and also to the wave vector. This behavior is also observed in electromagnetic waves and denoted as circularly polarized waves [37]. Finally, the velocity vector reads

$$\boldsymbol{u}_R = |\boldsymbol{a}| \left[\cos(\omega t - \boldsymbol{k} \cdot \boldsymbol{r}) \boldsymbol{e}_a - \sin(\omega t - \boldsymbol{k} \cdot \boldsymbol{r}) \boldsymbol{e}_b \right] \, , \tag{4.15}$$

where $\boldsymbol{e}_a$ and $\boldsymbol{e}_b$ are the unit vectors in the direction of $\boldsymbol{a}$ and $\boldsymbol{b}$, respectively. The phase and group speeds (defined in Eq. 3.9) read respectively as

$$\boldsymbol{c}_p = 2\Omega \cos(\theta) \frac{\boldsymbol{k}}{|\boldsymbol{k}|^2} \, , \tag{4.16}$$

$$\boldsymbol{c}_g = \pm \frac{2\Omega}{|\boldsymbol{k}|} \left(\boldsymbol{e}_z - \frac{\boldsymbol{k}}{|\boldsymbol{k}|} \cos(\theta) \right) \, . \tag{4.17}$$

Note that the phase and group speeds are normal to each other. In the literature, the plane waves are observed in the canonical experiment of the rotating cylindrical water tank that is forced by a oscillating disk. The setup is first proposed by Oser Hansjörg [39] and also employed by Fultz [40], McEwan [41]. The flow visualization was achieved by the optical contrast from aluminum gilt. Only recently, a quantitative agreement with the theory is achieved via PIV measurements by Messio *et al.* [42], Cortet *et al.* [43]. A snapshot of the vorticity field from [43] is shown in right part of Fig. 4.2. By the forcing frequency of the disk, the direction of inertial waves can be accurately estimated using Eq. (4.13). Note that, waves are admitted only if the disk oscillation frequency is less than twice of the tanks rotation, i.e. $\omega \leq 2\Omega$, since $|cos(\alpha)| \leq 1$.

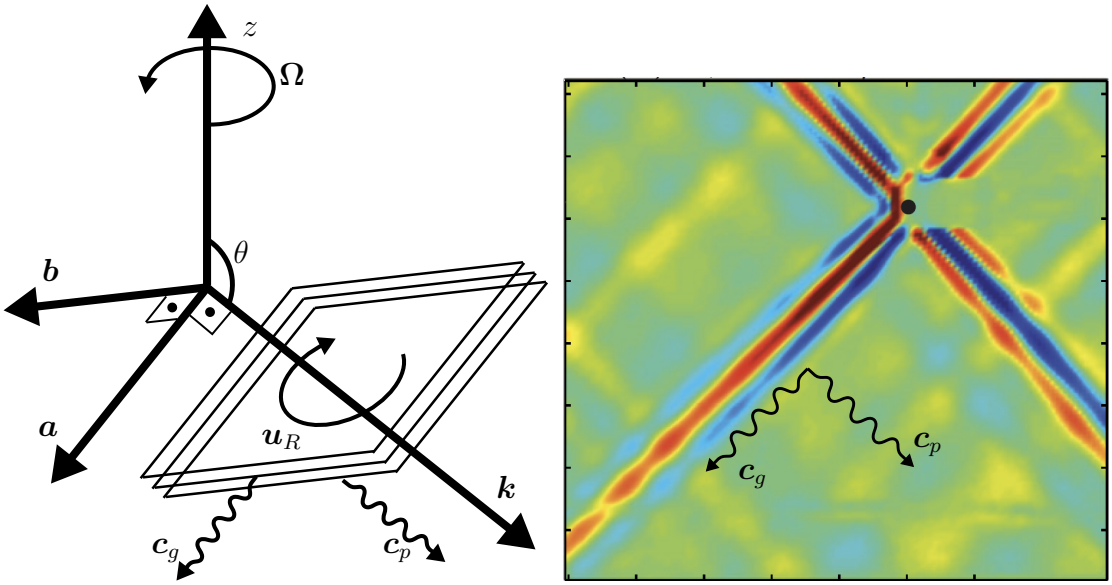

Figure 4.2: Left: Sketch of the relevant vectors of plane inertial waves. Right: Experimental visualization of inertial waves in a rotating tank forced by a oscillating disk (taken from Cortet *et al.* [43]). PIV image of tangential vorticity field, ω_θ, is shown. The phase and group speed directions are added.

4.2 Kelvin Waves

In the previous section, plane inertial waves were introduced. The derivation assumed no boundary conditions because of a large rotating tank compared to inertial wave scales. In the work of Kelvin [19], inertial waves are derived for vortex cores enclosed by a rotating duct, which results in non-planar waves due to boundary effects. These waves are commonly attributed as *Kelvin waves*. For the derivation, the stability analysis discussed in Chapter 3 is employed. The linearized and modal decomposed Euler equation as defined by Eq. (3.16) for centrifugal instabilities is also used here to characterize wave structures. The vortex core is modeled by the solid body rotation, i.e. $\bar{u}_\theta = \Omega r$. This simplifies the differential equation further to

$$\frac{\mathrm{d}}{\mathrm{d}r}\left(\frac{1}{r}\frac{\mathrm{d}(r\hat{u}_r)}{\mathrm{d}r}\right) - \hat{u}_r\left(k^2 - 4\Omega^2\frac{k^2}{\omega^2}\right) = 0\ , \tag{4.18}$$

with impermeable boundary conditions for inner and outer walls (no flow through the solid)

$$\hat{u}_r(r_i) = 0 \,, \tag{4.19}$$
$$\hat{u}_r(r_o) = 0 \,, \tag{4.20}$$

respectively. The second order ordinary differential equation with these boundary conditions is a Sturm-Liouville equation as discussed in Sec. 2.1. Hence, for a real wave number, k, the solution consists of infinitely many eigenvalues, ω_n, and corresponding orthogonal eigenmodes, $\hat{u}_{r,n}$. The solution is identified by Kelvin [19] as

$$\hat{u}_r(r) = \alpha \left[J_1\left(\frac{k\sqrt{4\Omega^2 - \omega^2}}{\omega} r \right) + \beta Y_1\left(\frac{k\sqrt{4\Omega^2 - \omega^2}}{\omega} r \right) \right] \,, \tag{4.21}$$

where α and β are prefactors to be determined from boundary and initial conditions. J_1 and Y_1 are the first and second kind of Bessel functions, respectively. Assuming a positive wave number and employing both boundary conditions, the following dispersion relation is obtained

$$\omega_n = \pm \frac{2\Omega k}{\sqrt{k^2 + \lambda_n^2}} \,, \tag{4.22}$$

where λ_n indicates roots of the following equation

$$J_1(\lambda_n r_o) Y_1(\lambda_n r_i) - J_1(\lambda_n r_i) Y_1(\lambda_n r_o) = 0 \,. \tag{4.23}$$

Corresponding eigenmodes in the radial velocity read as

$$M_{r,n}(r) = \alpha \left[J_1(\lambda_n r) - \frac{J_1(\lambda_n r_i)}{Y_1(\lambda_n r_i)} Y_1(\lambda_n r) \right] \,, \tag{4.24}$$

Here, the prefactor α is left undetermined as no initial condition is posed. In Fig. 4.3, first three eigenmodes are shown. Note that, the normalized radial velocity, $M^*_{r,n}$, is used, so that the maximum value is 1. Similarly, the radius is scaled between 0 and 1, i.e. $r^* = (r - r_i)/(r_o - r_i)$.

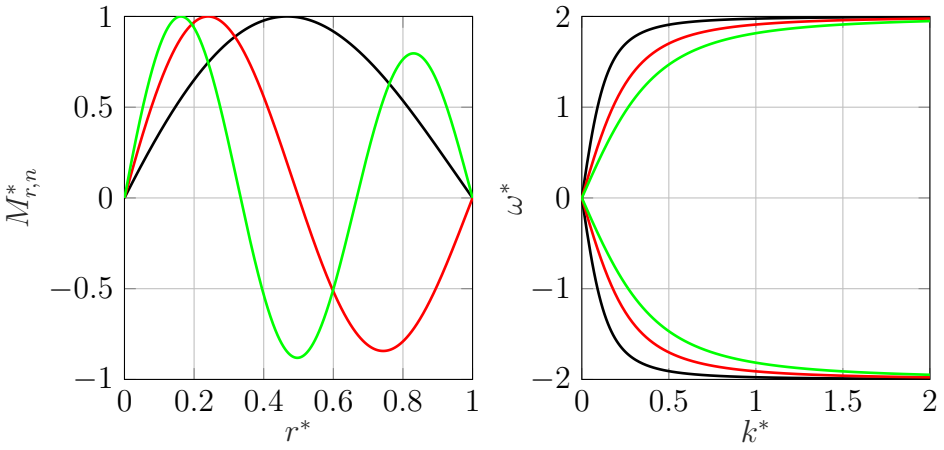

Figure 4.3: Left: First three eigenmode structures of normalized radial velocity as a function of normalized radius. Right: The plot of dispersion relation for the first three eigenmodes. The normalized angular frequency is plotted against the normalized wave number. Black color indicates the first mode ($n = 1$), red the second and green the third mode.

Owing to orthogonality, any function that satisfies the boundary conditions can be formed as a superposition of eigenmodes. In Fig. 4.3, the dispersion relation is shown for the first three eigenmodes in the right plot. The angular frequency is normalized with the circulation, $\omega = \omega^*\Omega$. The wave number is normalized with the first root of Eq. (4.23), $k = k^*\lambda_1$. Since there is a $\pm$ sign in the dispersion relation in Eq. (4.22), for each eigenmode there exist two eigenvalues with opposite propagation directions. Moreover, following the definitions of phase and group speeds in Eq. (3.9), the wave propagation is dispersive, i.e. $c_p \neq c_g$. In Paper IW-Speed, propagation speeds of the inertial waves are further discussed.

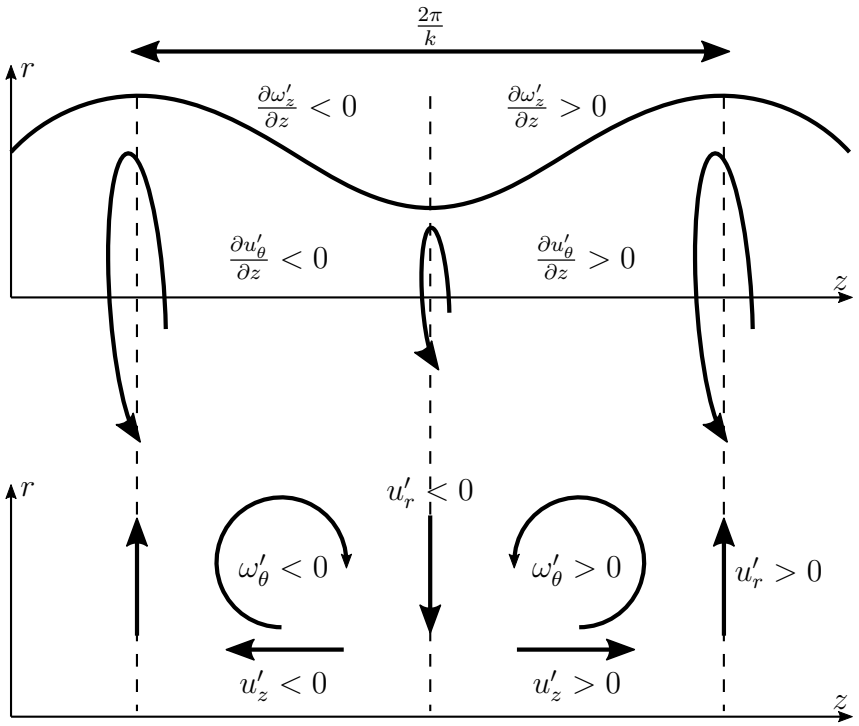

Figure 4.4: A sketch of Kelvin wave dynamics that is generated by the axial vorticity perturbation ω_z'. The figure is adopted from Renac *et al.* [47].

The physical explanation of Kelvin wave propagation in vortex tube was given by Arendt *et al.* [48] via solving an initial value problem for the Rankine vortex. The time evolution of an axisymmetric Gaussian perturbation in the axial vorticity is observed as the twisting of vortex lines. Based on the movement of the vortex core radius, the propagation is interpreted. A similar approach was given by Greitzer *et al.* [49]. Inspired by these works, Renac *et al.* [47] interpreted the wave motion for the solid body rotation. Here, this interpretation is revisited. The governing equation for the linearized vorticity, $\boldsymbol{\omega'} = \boldsymbol{\nabla} \times \boldsymbol{u'}$, reads

$$\frac{\partial \boldsymbol{\omega'}}{\partial t} = 2\Omega \frac{\partial \boldsymbol{u'}}{\partial z} \, , \tag{4.25}$$

which is equivalent to Eq. (4.8) as derived for plane inertial waves in the previous section. The oscillatory line in the upper part of Fig. 4.4 indicates the initial perturbations in the axial vorticity, which is defined as

$$\omega_z' = \frac{\partial r u_\theta'}{\partial r} \, . \tag{4.26}$$

Note that the slopes of axial vorticity perturbations and tangential velocity perturbations, u'_θ, are aligned in the stream-wise direction. Tangential velocity perturbations are illustrated with semicircles (larger indicates stronger perturbation). The axial gradient of tangential velocity fluctuations, $\partial u'_\theta/\partial z$, generates tangential vorticity fluctuations, ω'_θ, via Eq. (4.25). By the definition of the linearized tangential vorticity

$$\omega'_\theta = \frac{\partial u'_r}{\partial z} - \frac{\partial u'_z}{\partial r} \ , \tag{4.27}$$

the radial gradient in axial velocity perturbation is generated. This results in an axial stretching for the minimum of ω'_z and an axial contraction for the maximum of ω'_z as illustrated in the lower part of the Fig. 4.4. Employing Eq. (4.25) in the stream-wise direction, a reverse ω'_z with respect to the initial perturbation is generated as a result. This forms a restoring mechanism, which governs the oscillatory propagation of the initial perturbation in both stream-wise directions.

In literature, the Kelvin wave dynamics is attributed to the axisymmetric vortex breakdown (see Benjamin [50]). A flow with the solid body rotation and uniform stream-wise velocity is considered, i.e. $\boldsymbol{u} = [\bar{u}_z, \Omega r, 0]$. In such cases, the dispersion relation in Eq. (4.22) is simply extended by a Doppler shift. The flow is characterized as a supercritical vortex, if inertial waves only propagate downstream. If upstream propagation occurs, the flow is called as subcritical. The transition is characterized by the critical circulation strength, Ω_c, which satisfies

$$\Omega_c = \frac{\bar{u}_z}{2}\sqrt{k^2 + \lambda_n^2} \tag{4.28}$$

The subcritical vortex is believed to initiate the vortex breakdown.

Kerrebrock [51], Golubev and Atassi [52], Tam and Auriault [53] studied wave modes in swirling turbomachinary ducts. Compressible Euler equations were used to distinguish between acoustic and inertial wave modes. The impact of compressibility and different swirl profiles on wave modes were investigated. These authors employed a modal analysis similar to the Kelvin's approach [19] although the term *inertial waves* was not explicitly mentioned.

5 Inertial Waves in Thermo-acoustics

In this chapter, inertial waves are discussed from the thermo-acoustic perspective. Although inertial waves are not recognized in the thermo-acoustic community, several publications revealed some properties of inertial waves without providing physical explanation. These publications are reviewed in this chapter as a literature survey and the achievements of this dissertation are discussed accordingly.

In combustion applications, rotating flows are extensively employed [54–56]. A common practice is to employ swirl generators to generate rotation. In Fig. 5.1, examples of widely used axial (left) and radial (right) swirl generators are illustrated. The swirl provides several advantages in terms of the flame stability and the mixing. The flame stabilization is enhanced by the central recirculation zone that mixes hot burned products with fresh unburnt reactants. Mixture inhomogeneities are reduced by the improved mixing process between the oxidizer and fuel.

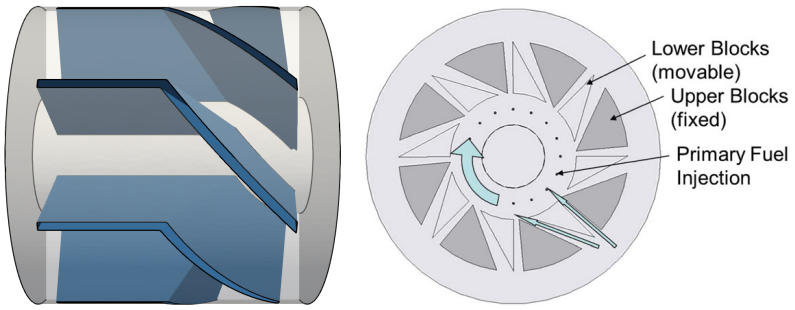

Figure 5.1: Examples of axial (left) and radial (right) swirl generators. The axial swirler is from TU Munchen burner [16] and the image is generated by a CAD drawing. The radial swirler image is taken from TU Berlin burner by Terhaar *et al.* [57], Schimek *et al.* [58]

Other than these preferable properties, swirl generators have also an impact on thermo-acoustics of a combustion system [59, 60]. Experimental studies by Richards and Yip [12], Straub and Richards [13], Komarek and Polifke [16], Palies *et al.* [61], Kim and Santavicca [62] demonstrated that the flame is sensitive to tangential velocity modulations generated at the swirler. They recognized that these modulations propagate with the mean flow speed. Due to the difference in propagation speeds of convective and acoustic waves, strong changes in combustor sound pressure levels were observed by moving the swirler in the stream-wise direction.

In the theoretical framework, the generation of tangential velocity perturbations is attributed to a mode conversion process. Incident plane acoustic waves generate tangential velocity perturbations while passing through the swirler. This process is modeled via the actuator disk theory, which is extensively used for identifying jump conditions across turbomachinery cascades [49, 63]. The jump conditions for tangential velocity perturbations were introduced

by Cumpsty and Marble [14] and later employed by Palies *et al.* [15]. This is revisited in Sec. 5.1.

As discussed in the introduction, convective propagation has been assumed for tangential velocity perturbations. However, recent publications reported puzzling results, i.e. the propagation is around 40-50% faster than the mean flow [16–18]. In Paper IW-Speed, this behavior is explained by the dispersive behavior of Kelvin waves discussed in Sec. 4.2. A more profound approach is presented in Sec. 5.2, i.e. the initial value problem is proposed to characterize the time domain representation of the propagation. The corresponding manuscript has been submitted to Journal of Fluid Mechanics and currently under review.

The flame response to inertial waves was studied by several research groups with different explanations of the relevant mechanism. Hirsch *et al.* [64] modeled the overall flame transfer function by considering the Biot-Savart law for vorticity fluctuations. Komarek and Polifke [16] constructed the flame transfer function by the superposition of acoustic and vortical contributions. Palies *et al.* [61] attributed the flame response to turbulent flame speed modulations caused by tangential velocity fluctuations. Acharya and Lieuwen [18] recognized flow perturbations in all directions caused by the tangential velocity modulations at the swirler. In Paper IW-Flame, the flame response mechanism is discussed by respecting the Kelvin wave eigenmodes.

5.1 Generation: Actuator Disk Theory

The mode conversion process of tangential velocity fluctuations from incident plane acoustic waves across a swirler is modeled via the actuator disk theory by Cumpsty and Marble [14], Palies *et al.* [15]. The swirler is modeled as a thin disk, which generates azimuthal momentum instantly. The jump condition across the swirler is schematically illustrated in Fig. 5.2. The upstream condition of the swirler is indicated by the subscript 1 and downstream by 2. Black and red arrows indicate the base and perturbed flow quantities, respectively. In a low Mach number flow, the jump across the swirler for mean flow quantities is assumed to be isentropic and incompressible. The base axial velocity across the swirler is constant, since there is no area change in the duct. The base tangential velocity is modeled via the Kutta condition, i.e. the flow angle at the swirler exit does not change. These jump conditions for the base flow read mathematically

$$\bar{s}_1 = \bar{s}_2 \ , \tag{5.1}$$

$$\bar{\rho}_1 = \bar{\rho}_2 \ , \tag{5.2}$$

$$\bar{u}_{z,1} = \bar{u}_{z,2} \ , \tag{5.3}$$

$$\bar{u}_{\theta,2} = \bar{u}_{z,2} \tan \bar{\theta}_2 \ , \tag{5.4}$$

where $\bar{\theta}_2$ is the swirler angle as illustrated in the Fig. 5.2. The upstream flow is assumed uniform and parallel to the stream-wise direction, hence $\bar{\theta}_1 = 0$.

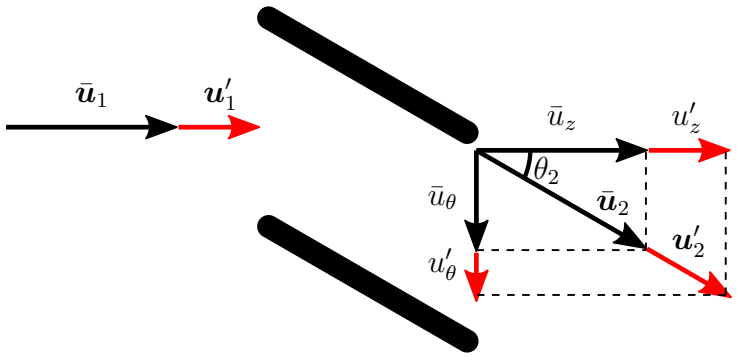

Figure 5.2: Base and perturbed flow vectors across the swirler.

For perturbed quantities, linearized compressible equations are employed to describe the jump across the swirler. Following conditions are derived from isentropic assumption, linearized continuity and energy equation, respectively

$$s'_1 = s'_2 \ , \tag{5.5}$$

$$\frac{\rho'_1}{\bar{\rho}_1} + \frac{u'_1}{\bar{u}_1} - \theta'_1 \tan\bar{\theta}_1 = \frac{\rho'_2}{\bar{\rho}_2} + \frac{u'_2}{\bar{u}_2} - \theta'_2 \tan\bar{\theta}_2 \ . \tag{5.6}$$

$$\frac{p'_1}{\gamma\bar{p}_1} + \frac{s'_1}{(\gamma-1)c_p} = \frac{p'_2}{\gamma\bar{p}_2} + \frac{s'_2}{(\gamma-1)c_p} \ , \tag{5.7}$$

where the specific heat, c_p, and the ratio of specific heat ratio, γ, are assumed to be constant across the swirler. Moreover, assuming that the pressure drop across the swirler is negligible, $\bar{p}_1 = \bar{p}_2$, and the swirler is acoustically transparent yield the following simplified conditions

$$p'_1 = p'_2 \ , \tag{5.8}$$

$$u'_{z,1} = u'_{z,2} \ , \tag{5.9}$$

$$u'_{\theta,2} = u'_{z,1} \tan\bar{\theta}_2 \ . \tag{5.10}$$

Physically interpreting these conditions reveals that incident plane acoustic waves are transmitted lossless across the swirler and generate tangential velocity perturbations depending on the swirler blade angle. At this point, mere convection has been taken for granted and no attempt has been made to characterize the subsequent propagation of tangential velocity perturbations. This is investigated in the following section.

5.2 Propagation: Initial Value Problem

In Paper IW-Speed, the frequency response of inertial waves is constructed from Kelvin eigenmodes. The input of the frequency response was selected as the tangential velocity perturbation at the swirler exit. As the output, the tangential velocity perturbation at a downstream position of the mixing duct was chosen. This section introduces an alternative approach to characterize the propagation. An initial value problem is proposed, where a step perturbation in the acoustic plane wave is introduced upstream of the swirler. Corresponding inertial wave motion is derived

analytically via the method of steepest descent as discussed in Sec. 2.2. The following results are new material, submitted to Journal of Fluid Mechanics and currently under review [65].

An annular duct is considered with the inner and outer radii indicated by r_i and r_o, respectively. Following Kerrebrock [51] the base flow downstream of a swirler is approximated by a solid body rotation with uniform plug flow, $\bar{\boldsymbol{u}} = [\bar{u}_z, \Omega r, 0]$. To propose an initial value problem, modal ansatz is only applied to the stream-wise direction. For the time, the Laplace transformation is applied so that initial conditions are respected. The transformation and its inverse read

$$\hat{u}(s,k,r) = \int_{-\infty}^{\infty}\int_{0}^{\infty} u'(t,z,r)\exp(-st-ikz)\mathrm{d}t\mathrm{d}z \ , \tag{5.11}$$

$$u'(t,z,r) = \frac{1}{(2\pi)^2 i}\int_{-\infty}^{\infty}\int_{\gamma-i\infty}^{\gamma+i\infty} \hat{u}(s,k,r)\exp(st+ikz)\mathrm{d}s\mathrm{d}k \ , \tag{5.12}$$

where γ is a real number, which is greater than all singularities of $\hat{u}(s,k,r)$. The transformation is applied on linearized incompressible axisymmetric Euler equations

$$\frac{\partial \hat{u}_r}{\partial r} + \frac{\hat{u}_r}{r} + ik\hat{u}_z = 0 \ , \tag{5.13}$$

$$s\hat{u}_z - \hat{u}_z(t=0) + ik\bar{u}_z\hat{u}_z = -\frac{ik}{\bar{\rho}}\hat{p} \ , \tag{5.14}$$

$$s\hat{u}_r - \hat{u}_r(t=0) + ik\bar{u}_z\hat{u}_r - 2\Omega\hat{u}_\theta = -\frac{\partial \hat{p}}{\partial r} \ , \tag{5.15}$$

$$s\hat{u}_\theta - \hat{u}_\theta(t=0) + ik\bar{u}_z\hat{u}_\theta + 2\Omega\hat{u}_r = 0 \ . \tag{5.16}$$

As an initial condition, a step acoustic perturbation is employed. The corresponding acoustic velocity perturbation reads

$$u'_{z,a}(t=0,z,r) = H(-z)\bar{u}_z\varepsilon \ , \tag{5.17}$$

where ε is a small number and the Heaviside step function, $H(z)$, indicates a step perturbation. Note that, since the focus of this analysis is the inertial wave dynamics, the incompressible form of the Euler equations is employed. Hence, acoustic perturbation in Eq. (5.17) is not included in Euler equations. Following the actuator disk theory, the tangential velocity fluctuations are generated across the swirler via acoustic velocity perturbation. The initial condition for the tangential velocity fluctuation reads

$$u'_\theta(t=0,z,r) = H(-z)f(r) \ , \tag{5.18}$$

where the perturbation profile, $f(r)$, is calculated via Eq. (5.10) as $f(r) = \bar{u}_z\varepsilon\tan(\bar{\theta}_2)$. It is also assumed that no radial velocity fluctuations are generated across the swirler due to the acoustic perturbation. As discussed in Sec. 4.2, orthogonal Kelvin wave eigenmodes can be used to reconstruct any perturbation. The eigenmode profile for the radial and azimuthal velocity is denoted by $M_{r,n}$ and the profile for the axial velocity and the pressure by $M_{z,n}$. Mathematically, the eigenmodes read

$$M_{r,n}(r) = J_1(\lambda_n r) - \frac{J_1(\lambda_n r_i)}{Y_1(\lambda_n r_i)}Y_1(\lambda_n r) \ , \tag{5.19}$$

$$M_{z,n}(r) = J_0(\lambda_n r) - \frac{J_1(\lambda_n r_i)}{Y_1(\lambda_n r_i)}Y_0(\lambda_n r) \ , \tag{5.20}$$

where λ_n indicates eigenvalues, which are obtained by solving

$$J_1(\lambda_n r_o)Y_1(\lambda_n r_i) - J_1(\lambda_n r_i)Y_1(\lambda_n r_o) = 0 \ . \tag{5.21}$$

The initial condition can be written as a sum of these eigenmodes

$$u'_\theta(t=0,z,r) = H(-z)\sum_{n=1}^{\infty}\alpha_n M_{r,n}(r) \ , \tag{5.22}$$

where α_n is the modal coefficient of the n^{th} eigenmode as

$$\alpha_n = \frac{\int_{r_i}^{r_o} f(r)M_{r,n}(r)\mathrm{d}r}{\int_{r_i}^{r_o} M_{r,n}^2(r)\mathrm{d}r} \ . \tag{5.23}$$

The Fourier transformed initial condition reads as

$$\hat{u}_\theta(t=0) = \left(\pi\delta(k) + \frac{i}{k}\right)\sum_{n=1}^{\infty}\alpha_n M_{r,n}(r) \ . \tag{5.24}$$

Similar to Eq. (4.18) for describing Kelvin waves in the previous chapter, the set of equations can be simplified to a second order ordinary differential equation as

$$\frac{\mathrm{d}}{\mathrm{d}r}\left(\frac{1}{r}\frac{\mathrm{d}(r\hat{u}_r)}{\mathrm{d}r}\right) - \hat{u}_r\left(k^2 + \left(\frac{2\Omega k}{s+ik\bar{u}_z}\right)^2\right) = -\frac{2\Omega k^2}{\left(s+ik\bar{u}_z\right)^2}\left(\pi\delta(k)+\frac{i}{k}\right)\sum_{n=1}^{\infty}\alpha_n M_{r,n}(r) \ . \tag{5.25}$$

Note that, the left-hand-side is the homogeneous part, which is equivalent to the eigenvalue problem proposed in Eq. (4.18). The right-hand-side is the non-homogeneous part, which results from the initial condition. The solution can be formed via the undetermined coefficients method as

$$\hat{u}_r(r) = \hat{u}_{r,F} + \hat{u}_{r,P} \ , \tag{5.26}$$

where $\hat{u}_{r,F}$ is the fundamental solution of the homogeneous part and $\hat{u}_{r,P}$ is the particular solution obtained by a guess. The fundamental solution reads

$$\hat{u}_{r,F} = \alpha J_1\left(\frac{k\sqrt{-\left(s+ik\bar{u}_z\right)^2 - 4\Omega^2}}{s+ik\bar{u}_z}r\right) + \beta Y_1\left(\frac{k\sqrt{-\left(s+ik\bar{u}_z\right)^2 - 4\Omega^2}}{s+ik\bar{u}_z}r\right) \ . \tag{5.27}$$

For the particular solution, the same form as the initial condition is employed as a guess, which reads

$$\hat{u}_{r,P} = \sum_{n=1}^{\infty}\kappa_n M_{r,n}(r) \ , \tag{5.28}$$

where the coefficient κ_n is determined by substituting the particular solution into Eq. (5.25). This yields

$$\kappa_n = \frac{2\Omega k^2}{(s+ik\bar{u}_z)^2}\left(\pi\delta(k)+\frac{i}{k}\right)\frac{\alpha_n}{\lambda_n^2+k^2+\left(\frac{2\Omega k}{s+ik\bar{u}_z}\right)^2}\,. \tag{5.29}$$

Impermeability boundary conditions as defined in Eq. (4.19) are applied to the general solution, i.e. the sum of the homogeneous and particular parts. This is only satisfied if α and β vanish. Non-zero coefficients would only be possible for eigenvalues, however this is not satisfied due to the denominator of the particular solution, which becomes zero. Thus, the particular solution is also the general solution. Employing Eqs. (5.13)-(5.16), the complete solution reads

$$\hat{u}_r(s,k,r) = \frac{2\Omega k^2}{(s+ik\bar{u}_z)^2}\left(\pi\delta(k)+\frac{i}{k}\right)\sum_{n=1}^{\infty}\frac{\alpha_n M_{r,n}(r)}{\lambda_n^2+k^2+\left(\frac{2\Omega k}{s+ik\bar{u}_z}\right)^2}\,, \tag{5.30}$$

$$\hat{u}_\theta(s,k,r) = \frac{1}{s+ik\bar{u}_z}\left(\pi\delta(k)+\frac{i}{k}\right)\sum_{n=1}^{\infty}\frac{\alpha_n\left(\lambda_n^2+k^2\right)M_{r,n}(r)}{\lambda_n^2+k^2+\left(\frac{2\Omega k}{s+ik\bar{u}_z}\right)^2}\,, \tag{5.31}$$

$$\hat{u}_z(s,k,r) = \frac{2i\Omega k}{(s+ik\bar{u}_z)^2}\left(\pi\delta(k)+\frac{i}{k}\right)\sum_{n=1}^{\infty}\frac{\alpha_n\lambda_n M_{z,n}(r)}{\lambda_n^2+k^2+\left(\frac{2\Omega k}{s+ik\bar{u}_z}\right)^2}\,, \tag{5.32}$$

$$\hat{p}(s,k,r) = -\frac{2\rho\Omega}{s+ik\bar{u}_z}\left(\pi\delta(k)+\frac{i}{k}\right)\sum_{n=1}^{\infty}\frac{\alpha_n\lambda_n M_{z,n}(r)}{\lambda_n^2+k^2+\left(\frac{2\Omega k}{s+ik\bar{u}_z}\right)^2}\,. \tag{5.33}$$

The solution in time domain can be recovered by employing inverse Laplace transform from standard conversion tables as

$$\hat{u}_r(t,k,r) = \left(\pi\delta(k)+\frac{i}{k}\right)ke^{-ikt\bar{u}_z}\sum_{n=1}^{\infty}\frac{\alpha_n M_{r,n}(r)}{\sqrt{\lambda_n^2+k^2}}\sin\left(\frac{2\Omega kt}{\sqrt{\lambda_n^2+k^2}}\right)\,, \tag{5.34}$$

$$\hat{u}_\theta(t,k,r) = \left(\pi\delta(k)+\frac{i}{k}\right)e^{-ikt\bar{u}_z}\sum_{n=1}^{\infty}\alpha_n M_{r,n}(r)\cos\left(\frac{2\Omega kt}{\sqrt{\lambda_n^2+k^2}}\right)\,, \tag{5.35}$$

$$\hat{u}_z(t,k,r) = \left(\pi\delta(k)+\frac{i}{k}\right)ie^{-ikt\bar{u}_z}\sum_{n=1}^{\infty}\frac{\alpha_n\lambda_n M_{z,n}(r)}{\sqrt{\lambda_n^2+k^2}}\sin\left(\frac{2\Omega kt}{\sqrt{\lambda_n^2+k^2}}\right)\,, \tag{5.36}$$

$$\hat{p}(t,k,r) = -2\Omega\bar{\rho}\left(\pi\delta(k)+\frac{i}{k}\right)e^{-ikt\bar{u}_z}\sum_{n=1}^{\infty}\frac{\alpha_n\lambda_n M_{z,n}(r)}{\lambda_n^2+k^2}\cos\left(\frac{2\Omega kt}{\sqrt{\lambda_n^2+k^2}}\right)\,. \tag{5.37}$$

However, to the author's knowledge, no analytical inverse Fourier transformation is available for the wave number. Two possible treatments are presented in the following subsections.

5.2.1 Non-dispersive approximation

An approximate solution for low wave-number is derived by assuming $k << \lambda_n$. This assumption yields the following dispersion relation

$$\omega_n \approx \left(\bar{u}_z \pm \frac{2\Omega}{\lambda_n} \right) k \, . \tag{5.38}$$

Note that, the simplified dispersion relation is non-dispersive, since $\partial\omega/\partial k = \omega/k$. The propagation is analogous to plane acoustic waves. The speed of sound is replaced by the Coriolis parameter. In a supercritical flow, the stream-wise flow velocity is greater than this parameter, $\bar{u}_z > 2\Omega/\lambda_n$. Thus, both waves propagate downstream. With this assumption, the inverse Fourier transform can be performed analytically and the resulting set of equations read

$$\hat{u}_r(t,z,r) = 0.5 \sum_{n=1}^{\infty} \frac{\alpha_n M_{r,n}}{\lambda_n} \left[\delta\left(z - \bar{u}_z t - \frac{2\Omega t}{\lambda_n} \right) - \delta\left(z - \bar{u}_z t + \frac{2\Omega t}{\lambda_n} \right) \right] \, , \tag{5.39}$$

$$\hat{u}_\theta(t,z,r) = 0.5 \sum_{n=1}^{\infty} \alpha_n M_{r,n} \left[2 - H\left(z - \bar{u}_z t - \frac{2\Omega t}{\lambda_n} \right) - H\left(z - \bar{u}_z t + \frac{2\Omega t}{\lambda_n} \right) \right] \, , \tag{5.40}$$

$$\hat{u}_z(t,z,r) = 0.5 \sum_{n=1}^{\infty} \alpha_n M_{z,n} \left[H\left(z - \bar{u}_z t - \frac{2\Omega t}{\lambda_n} \right) - H\left(z - \bar{u}_z t + \frac{2\Omega t}{\lambda_n} \right) \right] \, , \tag{5.41}$$

$$\hat{p}(t,z,r) = -\Omega\bar{\rho} \sum_{n=1}^{\infty} \frac{\alpha_n M_{z,n}}{\lambda_n} \left[2 - H\left(z - \bar{u}_z t - \frac{2\Omega t}{\lambda_n} \right) - H\left(z - \bar{u}_z t + \frac{2\Omega t}{\lambda_n} \right) \right] \, . \tag{5.42}$$

These equations analytically describe the swirler response to the step perturbation in the acoustic velocity. The convective propagation assumption can be simply replaced by these results for low order thermo-acoustic network models. Since a step response fully characterizes linear systems, other type of perturbations such as harmonic and impulse forcing, can be easily derived from these equations. For example, performing a time derivate yields the impulse response. In the next section, the interpretation of these results are further discussed.

5.2.2 Asymptotic Solution by Method of Steepest Descent

A more rigorous solution is achieved by applying the method of steepest descent as described in Sec. 2.2. Here, only the solution of the tangential velocity $\hat{u}_\theta$ is presented. Other components can be derived similarly. The Eq. (5.35) is re-written in its exponential form as

$$\hat{u}_\theta(t,k,r) = 0.5 \left(\pi\delta(k) + \frac{i}{k} \right) e^{-ikt\bar{u}_z} \sum_{n=1}^{\infty} \alpha_n M_{r,n}(r) \left(e^{-\frac{2i\Omega kt}{\sqrt{\lambda_n^2 + k^2}}} + e^{\frac{2i\Omega kt}{\sqrt{\lambda_n^2 + k^2}}} \right) \, , \tag{5.43}$$

where the first term in the bracket indicates the fast propagating wave. The integral for the inverse Fourier transformation reads

$$u'_\theta(t,z,r) = \frac{1}{2\pi} \int_{-\infty}^{\infty} \hat{u}_\theta(t,k,r) e^{ikz} \mathrm{d}k \, . \tag{5.44}$$

For simplicity, the method of steepest descent is demonstrated only for the fast propagating wave. Moreover, the bulk velocity $\bar{u}_z$ is neglected for the ease of the derivation. Similarly, other terms, which do not depend on k, are neglected. However, in the final expression, Eq. (5.48), the most general form is presented. The integral for the inverse Fourier transform with the given simplification is written in the form introduced in Sec. 2.2 as

$$I(z) = \int_{-\infty}^{\infty} f(k) e^{zg(k)} = \int_{-\infty}^{\infty} \left(\pi\delta(k) + \frac{i}{k} \right) e^{z\left(ik - \frac{2i\Omega k}{\eta\sqrt{\lambda_n^2 + k^2}} \right)} \mathrm{d}k \ , \tag{5.45}$$

where $\eta = z/t$. Real and imaginary parts of the exponent function, $g(k)$, are shown in Fig. 5.3 as contour plots. Columns correspond to the real and imaginary part, respectively. Darker colors indicate lower values. The singularities are marked with red circles at $k = \pm\lambda_n$. Corresponding branch cuts are on the imaginary axis, i.e $k > i\lambda_n$ and $k < -\lambda_n$. Blue contours indicate constant levels of imaginary part, $\Im(g(k))$.

Saddle points are determined as

$$k_0 = \pm j_n \sqrt{\left(\frac{2\Omega}{\eta j_n} \right)^{\frac{2}{3}} - 1} \ . \tag{5.46}$$

Observing the form of saddle point relation, three different branches are recognized as $\eta > 2\Omega/j_n$, $\eta = 2\Omega/j_n$ and $\eta < 2\Omega/j_n$. The first branch is shown in the first row of the figure. Two non-degenerate saddle points marked with red cross are located on the imaginary axis. Similarly, there exists two saddle points for the branch, $\eta < 2\Omega/j_n$, which is shown in the last row. The saddle points lie on the real axis. For $\eta = 2\Omega/j_n$, there exist a single degenerate saddle point at the origin.

For each branch, the initial integral path, $k = (-\infty, \infty)$ is constructed by additional paths from the steepest descent method. Cauchy's integral theorem is employed, which states that the integral along a closed path with no singularities is zero. The closed integral paths are indicated with the green color. As an example, the first branch is discussed in detail. The closed integral path reads

$$\underbrace{\int_{\Gamma_1} + \int_{\Gamma_2}}_{I(z)} + \underbrace{\int_{\Gamma_3} + \int_{\Gamma_6}}_{C(z)} + \underbrace{\int_{\Gamma_4} + \int_{\Gamma_5}}_{S(z)} = 0 \ , \tag{5.47}$$

where $S(z)$ is the contribution by steepest descent path, which follows the constant level of $\Im(g(k))$ as discussed in Sec. 2.2. Note that the saddle point in the negative imaginary axis is a local minimum and does not define a steepest descent path. Thus, only the saddle point in the positive imaginary axis is employed. The circular paths, $C(z)$, enclose the contour so that the Cauchy's integral theorem can be employed. As the radius of the circular path grows to infinity, its contribution vanishes, $C(z) = 0$. Hence, the integral, $I(z)$, can be related to the steepest descent integral, $I(z) = -S(z)$. Similar explanations also work for the other two branches of η. The leading term for steepest descent integral, defined in Eq. (2.22), results into the general

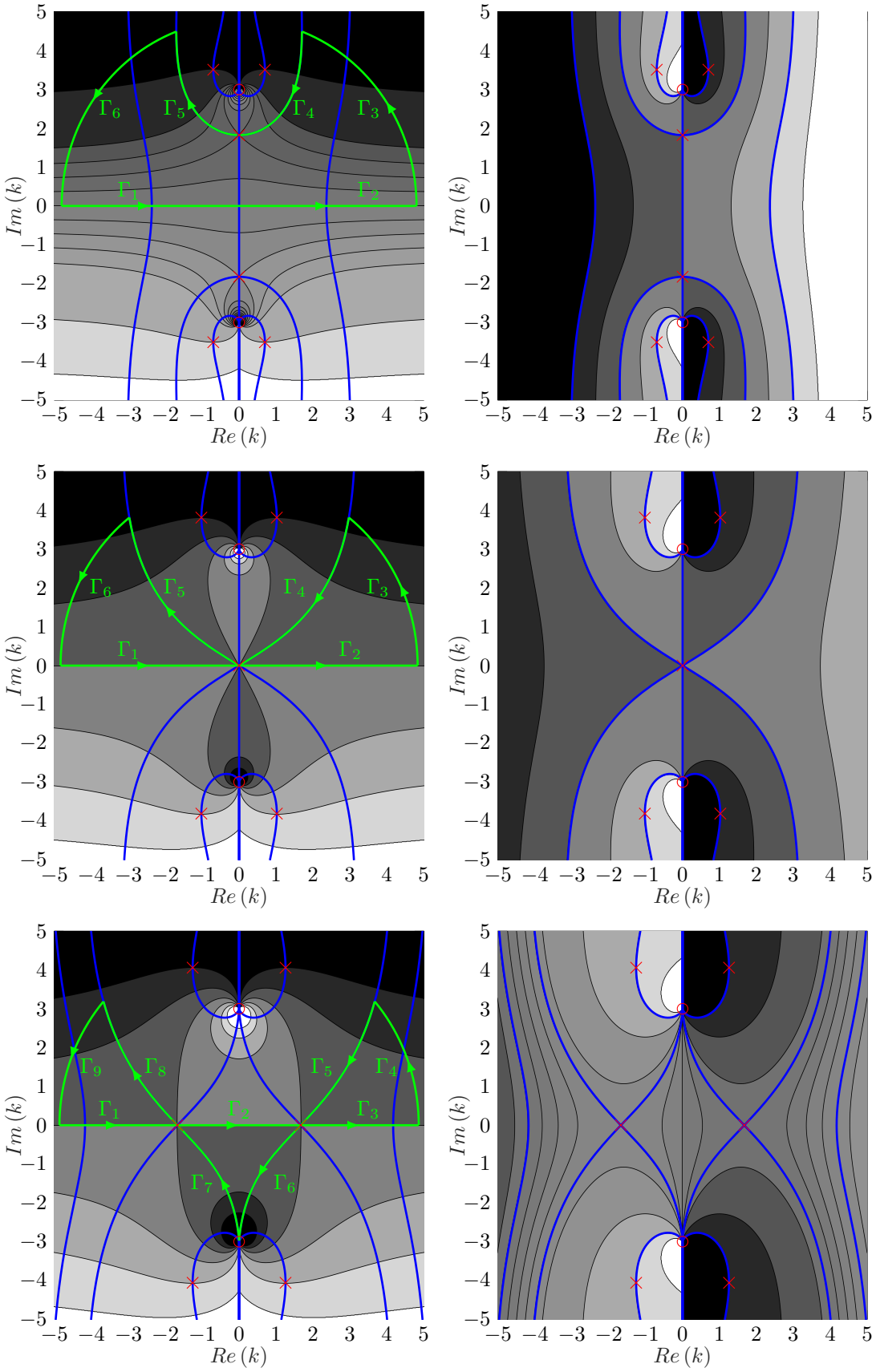

Figure 5.3: Contour plots of real (left) and imaginary (right) parts of $g(k)$. From top to bottom, three branches are plotted, $\eta > 2\Omega/j_n$, $\eta = 2\Omega/j_n$ and $\eta < 2\Omega/j_n$.

expression for tangential velocity perturbations as

$$u'_\theta(t,z,r) \approx \sum_{n=1}^{\infty} \alpha_n M_{r,n} \times \begin{cases} 1 - \left(\frac{2\Omega t}{j_n(\bar{u}_z t - z)}\right)^{\frac{1}{3}} \frac{e^{-j_n(-c_-)^{\frac{3}{2}}}}{2\sqrt{6\pi j_n}(-c_-)^{\frac{3}{4}}}, & \text{if } \eta < \bar{u}_z - \frac{2\Omega}{j_n} \\ \frac{5}{6}, & \text{if } \eta = \bar{u}_z - \frac{2\Omega}{j_n} \\ \frac{1}{2} + \left(\frac{2\Omega t}{j_n(\bar{u}_z t - z)}\right)^{\frac{1}{3}} \frac{\cos\left(j_n c_-^{\frac{3}{2}}\right) - \sin\left(j_n c_-^{\frac{3}{2}}\right)}{2\sqrt{3\pi j_n} c_-^{\frac{3}{4}}}, & \text{if } \bar{u}_z - \frac{2\Omega}{j_n} < \eta < \bar{u}_z \\ \frac{1}{2} - \left(\frac{2\Omega t}{j_n(z - \bar{u}_z t)}\right)^{\frac{1}{3}} \frac{\cos\left(j_n c_+^{\frac{3}{2}}\right) - \sin\left(j_n c_+^{\frac{3}{2}}\right)}{2\sqrt{3\pi j_n} c_+^{\frac{3}{4}}}, & \text{if } \bar{u}_z < \eta < \bar{u}_z + \frac{2\Omega}{j_n} \\ \frac{1}{6}, & \text{if } \eta = \bar{u}_z + \frac{2\Omega}{j_n} \\ \left(\frac{2\Omega t}{j_n(z - \bar{u}_z t)}\right)^{\frac{1}{3}} \frac{e^{-j_n(-c_-)^{\frac{3}{2}}}}{2\sqrt{6\pi j_n}(-c_-)^{\frac{3}{4}}}, & \text{if } \eta > \bar{u}_z + \frac{2\Omega}{j_n} \end{cases} \tag{5.48}$$

where

$$c_+ = \left(\frac{2\Omega t}{j_n}\right)^{\frac{2}{3}} - (z - \bar{u}_z t)^{\frac{2}{3}} \ , \tag{5.49}$$

$$c_- = \left(\frac{2\Omega t}{j_n}\right)^{\frac{2}{3}} - (\bar{u}_z t - z)^{\frac{2}{3}} \ . \tag{5.50}$$

The regions, $\bar{u}_z - 2\Omega/j_n > \eta > \bar{u}_z + 2\Omega/j_n$, correspond to the last row in the Fig. 5.3. The first region converges exponentially to 1. Similarly, the other one exponentially decays to 0. This is inline with the non-dispersive solution derived in the previous section, which predicts no fluctuations in these regions. The region, $\bar{u}_z - 2\Omega/j_n < \eta < \bar{u}_z + 2\Omega/j_n$, correspond to the first row in the Fig. 5.3. The oscillatory dispersive behavior is predicted as a combination of trigonometric functions. Note that the non-dispersive model does not capture the oscillatory behavior and estimates a constant value. All these four regions diverge as $\eta \to \bar{u}_z \pm 2\Omega/j_n$. The middle row in the Fig. 5.3 corresponds to these limits. The solution for these points are computed as $5/6$ and $1/6$ for $\eta = \bar{u}_z - 2\Omega/j_n$ and $\eta = \bar{u}_z + 2\Omega/j_n$, respectively.

In Fig. 5.4, inverse fast Fourier transformed results of equations (5.34)-(5.37) are shown as a numerical validation. Perturbations are plotted against the stream-wise direction downstream of the swirler for three different snapshots at $t = [5\ 15\ 25]$ms. The configuration of Komarek and Polifke [16] is demonstrated here. The annular duct radii are $r_i = 8$mm and $r_o = 20$mm. The bulk stream-wise velocity is 11.3m/s. The design point swirl angle is $\theta_2 = 45°$. Following Kerrebrock [51], the tangential velocity profile quickly develops into the stable solid body rotation. Thus, the azimuthal momentum is redistributed to the solid body rotation as

$$\int_{r_i}^{r_o} 2\pi r \Omega r \mathrm{d}r = \int_{r_i}^{r_o} 2\pi r \bar{u}_z \tan(\theta_2) \mathrm{d}r \tag{5.51}$$

The corresponding design point circulation strength is around $\Omega = 760\mathrm{s}^{-1}$. Here, only the first inertial wave eigenvalue is considered as it causes the greatest deviation in the propagation. By employing Eq. (5.21), the eigenvalue is computed as $\lambda_1 = 269.56\mathrm{m}^{-1}$. The resulting deviation in the propagation is quantified by

$$\frac{2\Omega/\lambda_n}{\bar{u}_z} \times 100 \approx 50\% \ , \tag{5.52}$$

which matches well with the experimental observation from Komarek and Polifke [16].

In left top part of Fig. 5.4, tangential velocity perturbations, $u'_\theta(t, z, r)$, are presented. Black lines indicate numerical inverse fast Fourier transformation results. Blue lines indicate the non-dispersive solution proposed in the previous section. Red lines indicate the asymptotic solution derived in this section. The oscillatory behavior is well captured by the asymptotic approach. The non-dispersive solution shows quantitative agreement. With both approaches the deviation in the propagation speed is apparent. These results also clarify the 40-50% deviation observed in literature. Although the initial perturbation is only in the tangential velocity, it generates fluctuations in other velocity components and also in pressure. The corresponding numerical inverse fast Fourier transformation results are shown in Fig. 5.4. Similar oscillatory behavior as tangential velocity perturbations is observed. This outcome motivated Paper IW-Flame, i.e. the flame response is attributed to axial and radial velocity perturbations, respectively $u'_z(t, z, r)$ and $u'_r(t, z, r)$.

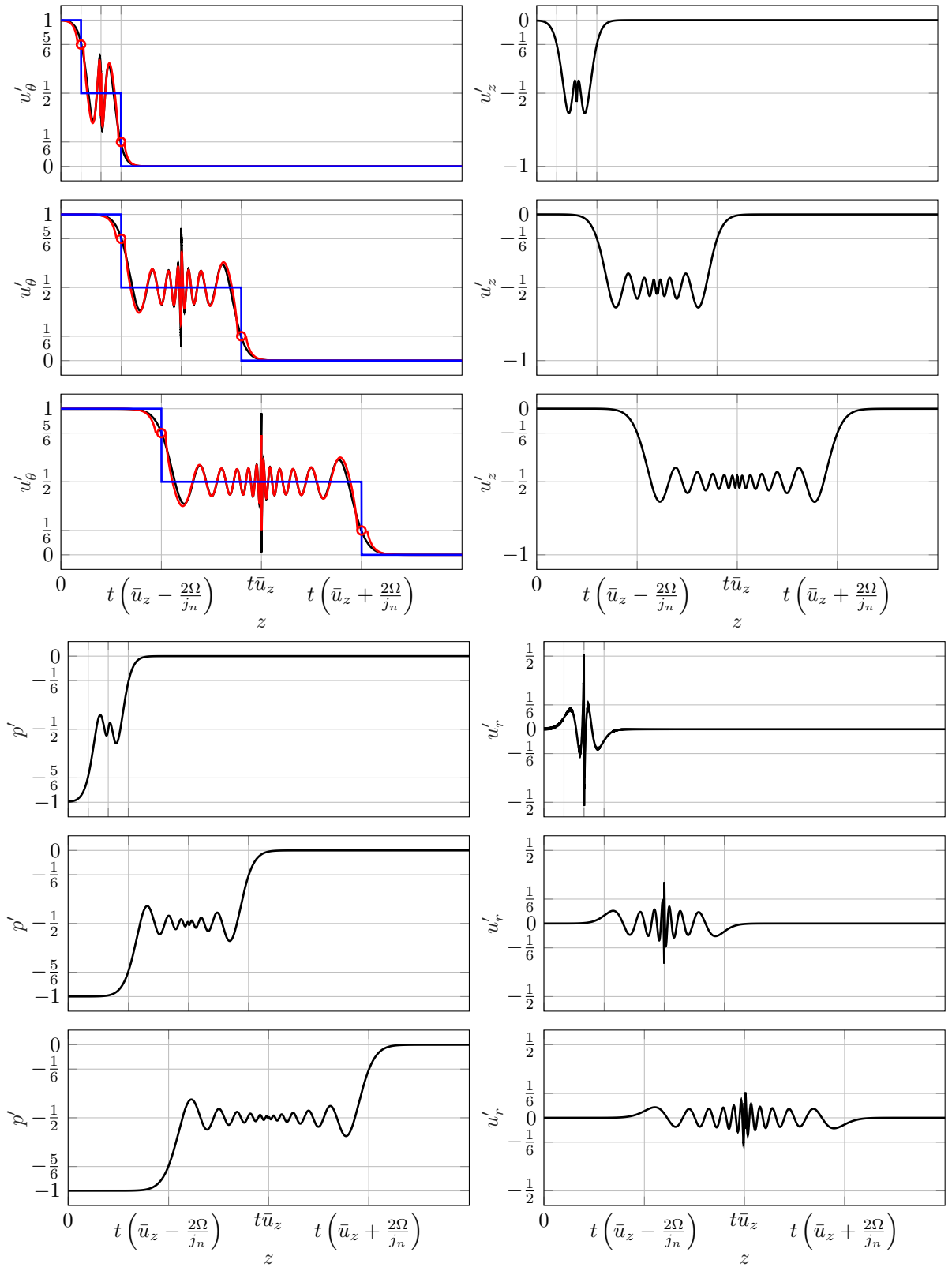

Figure 5.4: Snapshots of the inertial wave fields downstream of a swirler at $t = [5\ 15\ 25]$ms. Top images: $u'_\theta(t, z, r)$ (left) and $u'_z(t, z, r)$ (right). Bottom images: $u'_r(t, z, r)$ (left) and $p'(t, z, r)$ (right). p' is multiplied by $j_n/(2\Omega\bar{\rho})$. Black line corresponds to the numerical solution by inverse fast Fourier transformation. Blue line corresponds to the non-dispersive solution. Red lines and circles correspond to the asymptotic solution by the method of steepest descent.

6 Equivalence Ratio Waves

In this chapter, equivalence ratio waves are discussed with respect to thermo-acoustics. The impact of the equivalence ratio waves on the flame response was recognized decades ago. Since then, different research groups showed interest in this subject by devising models for predicting and understanding the flame response mechanism. Here, major contributions to this subject are reviewed. Achievements of this dissertation are discussed with respect to the relevant literature.

In industrial application, it is not feasible to achieve perfect mixing of air and fuel. This type of combustion process is recognized as technically/partially premixed in literature. For such flames, unsteady heat release rate is not only sensitive to the flow velocity, but also to equivalence ratio fluctuations as introduced by Keller *et al.* [20], Keller [66]. This is also confirmed by the experiments from Straub and Richards [67], Richards and Janus [68]. The impact of equivalence ratio fluctuations on the flame response becomes even stronger for the lean combustion, since the sensitivity of the heat of reaction to equivalence ratio perturbations increases with leaner premixture as discussed by Lieuwen *et al.* [69].

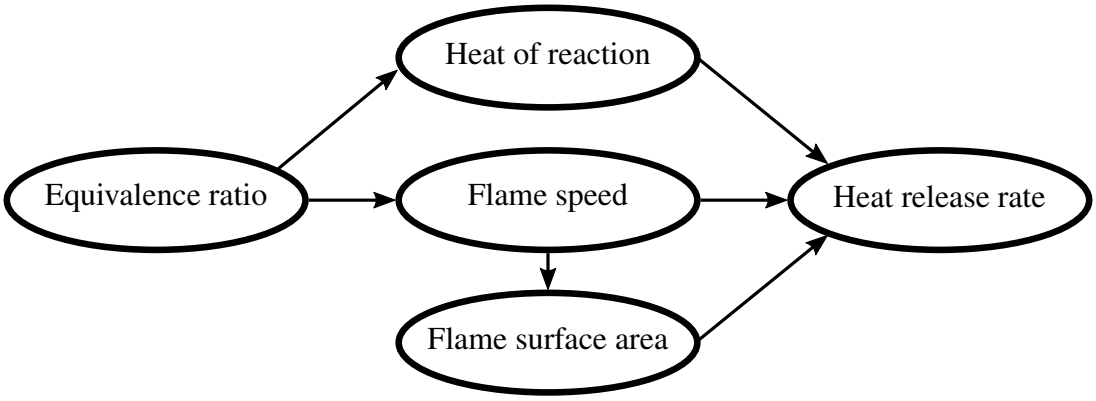

Figure 6.1: Schematic illustration of flame response contributions caused by equivalence ratio waves [70].

The equivalence ratio fluctuations are caused by the imperfect mixing through the mixing duct (see Shih *et al.* [71]), but more importantly by the air velocity and pressure fluctuations at the fuel injector (see Lieuwen and Zinn [21]). The latter contribution is directly related to the acoustics of the system and strongly affects the thermo-acoustic instability. This contribution is frequently addressed as ongoing research in literature. Further theoretical works were pioneered by Lieuwen and coauthors [21, 72] and Schuermans *et al.* [73] to understand the flame response mechanism and to develop simple flame transfer function models for equivalence ratio perturbations. These models identified heat of reaction contribution and the convective nature of the equivalence ratio fluctuations. The flame response contribution was modeled accordingly by a time lag model. The impact of the flame speed contribution to the flame transfer function

is introduced by Dowling and Hubbard [74]. The importance of diffusive processes is discussed by Polifke *et al.* [75], Bobusch *et al.* [76]. More complete model was proposed by Cho and Lieuwen [70], Lawn and Polifke [77], which also include the flame surface area contribution caused by flame speed modulations as illustrated in Fig. 6.1.

In Sec. 6.1, the generation mechanism of equivalence ratio waves from plane acoustic waves is presented. In Sec. 6.2, the convective propagation of the equivalence ratio waves is demonstrated.

6.1 Generation

The generation of equivalence ratio waves is analyzed by considering the mass conservation across the fuel injector. For a chemical reaction

$$\nu_F F + \nu_O O \rightarrow \text{Products} \,, \tag{6.1}$$

the equivalence ratio, ϕ, is defined for the unburnt region as

$$\phi = s\frac{\dot{m}_F}{\dot{m}_O} \,, \tag{6.2}$$

where F, O stand for fuel and oxidizer, respectively. The mass flow rate is indicated by $\dot{m}$. The stoichiometric coefficient is ν. The mass stoichiometric ratio, s, is defined as

$$s = \frac{\nu_O M_O}{\nu_F M_F} \,, \tag{6.3}$$

where M stands for the molar mass.

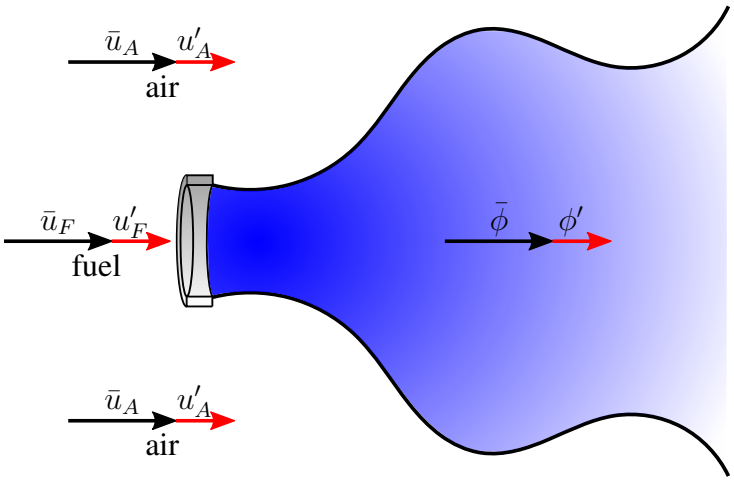

Figure 6.2: Schematic illustration of equivalence ratio wave generation. The upstream velocity perturbations modulate the mass flow rates of air and fuel. The fuel-air ratio changes and equivalence ratio waves are generated.

In the linearized framework, the equivalence ratio waves read

$$\frac{\phi'}{\bar{\phi}} = \frac{m'_F}{\bar{m}_F} - \frac{m'_O}{\bar{m}_O} \,. \tag{6.4}$$

This equation indicates that perturbations in the mass flow rate of fuel and air generate equivalence ratio fluctuations. This equation can be further simplified by considering the mass flow rate at the position of the fuel injector. This scenario is shown in Fig. 6.2, where co-axial jet flow is schematically illustrated. The fuel injector is located in the center of the duct and surrounded by the annular air stream. The mass flow rates at the position of the fuel injector is determined by $\dot{m} = \rho u A$, where ρ is the density, u is the flow velocity and A is the surface area. Surface areas of the fuel and air streams are constant. The mass flow rate modulations are therefore related to the density and flow velocity fluctuations. The former is relevant in the case of intake temperature inhomogeneities. However, in the thermo-acoustic perspective, only acoustics related flow velocity fluctuations are relevant. These assumptions simplify Eq. (6.4) further to

$$\frac{\phi'}{\bar{\phi}} = \frac{u'_F}{\bar{u}_F} - \frac{u'_O}{\bar{u}_O} \ . \tag{6.5}$$

Note that, a positive change in the air flow velocity causes a decrease in equivalence ratio. For fuel flow velocity, the opposite is true.

If the fuel injection is choked or acoustically fully reflective, then the injector is called stiff. This is achieved by a large pressure drop across the fuel injector. For stiff injector, acoustic pressure variations at the fuel injector do not cause equivalence ratio fluctuations, hence $u'_F = 0$. The only mechanism that causes equivalence ratio fluctuations is the acoustic velocity perturbations at the fuel injector.

6.2 Propagation: Initial Value Problem

In order to analyze the propagation of the equivalence ratio waves, the local definition based on mass fractions is employed

$$\phi = s\frac{Y_F}{Y_O} \ , \tag{6.6}$$

where the mass fraction of fuel Y_F and oxygen Y_O are determined from the transport equations, i.e.

$$\frac{\partial\left(\rho Y_F\right)}{\partial t} + \boldsymbol{\nabla}\cdot\left(\boldsymbol{u}\rho Y_F\right) = \boldsymbol{\nabla}\cdot\left(\rho D_F \boldsymbol{\nabla} Y_F\right) + \omega_F \ , \tag{6.7}$$

$$\frac{\partial\left(\rho Y_O\right)}{\partial t} + \boldsymbol{\nabla}\cdot\left(\boldsymbol{u}\rho Y_O\right) = \boldsymbol{\nabla}\cdot\left(\rho D_O \boldsymbol{\nabla} Y_O\right) + s\omega_F \ . \tag{6.8}$$

Assuming that the fluctuations in species mass fractions are small compared to the mean values, the equations can be linearized. Moreover, assuming a single species diffusion coefficient $D = D_O = D_F$ for all species, the transport equation for the equivalence ratio waves can be derived. First, Eq. (6.7) is multiplied by $s/\bar{Y}_O$ and Eq. (6.8) by $-s\bar{Y}_F/\bar{Y}_O^2$. Then, the summation of two yields the well known scalar transport equation, i.e.

$$\frac{\partial \rho\phi'}{\partial t} + \boldsymbol{\nabla}\left(\boldsymbol{u}\rho\phi'\right) = \boldsymbol{\nabla}\cdot\left(\rho D\boldsymbol{\nabla}\phi'\right) \ . \tag{6.9}$$

The source term ω_F drops from the derivation, because the equivalence ratio is defined for the unburnt condition. The convective nature of equivalence ratio waves are evident from Eq. (6.9).

To derive an analytical low order model, the equation is further simplified for 1-d flow by assuming density, species diffusion coefficient and velocity to be uniform. The simplified equation reads

$$\frac{\partial \phi'}{\partial t} + \bar{u}_z \frac{\partial \phi'}{\partial z} - D \frac{\partial^2 \phi'}{\partial z^2} = 0 \tag{6.10}$$

Similar to the inertial waves in Sec. 5.2, the initial value problem is proposed to quantify the propagation of equivalence ratio waves. Again, the step response approach is employed by considering a sudden jump in the upstream acoustic velocity as an initial condition. Mathematically,

$$u'_{z,a}(t = 0, z) = \bar{u}_z \varepsilon H(-z) \ . \tag{6.11}$$

For a stiff injector configuration as discussed in the previous section, this yields a negative fluctuation in the equivalence ratio

$$\phi'(t = 0, z) = -\bar{\phi} \varepsilon H(-z) \tag{6.12}$$

Eq. (6.10) is transformed into an algebraic equation by employing modal ansatz for the stream-wise direction and Laplace transformation for the time. This reads as

$$\hat{\phi}(s, k) = -\frac{\bar{\phi} \varepsilon (\pi \delta(k) + \frac{i}{k})}{s + ik\bar{u}_z + Dk^2} \ . \tag{6.13}$$

The time-space domain solution is retrieved by inverse Laplace transformation for the time and inverse Fourier transformation for the stream-wise direction. The final expression is

$$\phi'(t, z) = -0.5 \bar{\phi} \varepsilon \left(1 - \ \text{erf} \left(\frac{z - \bar{u}_z t}{\sqrt{4Dt}} \right) \right) \ . \tag{6.14}$$

Similar to the Fig. 5.4, the solution is plotted in the stream-wise direction for three different instances $t = [5\ 10\ 15]$ms in Fig. 6.3. The configuration from Paper ϕ'-Flame is considered. The base axial flow velocity is $\bar{u}_z = 1$m/s. The molecular diffusivity is $D = 0.22 \times 10^{-4}$m^2/s. The well-known behavior of advection-diffusion problem is observed, i.e. the perturbation propagates with the mean flow and diffuses in the stream-wise direction at the same time.

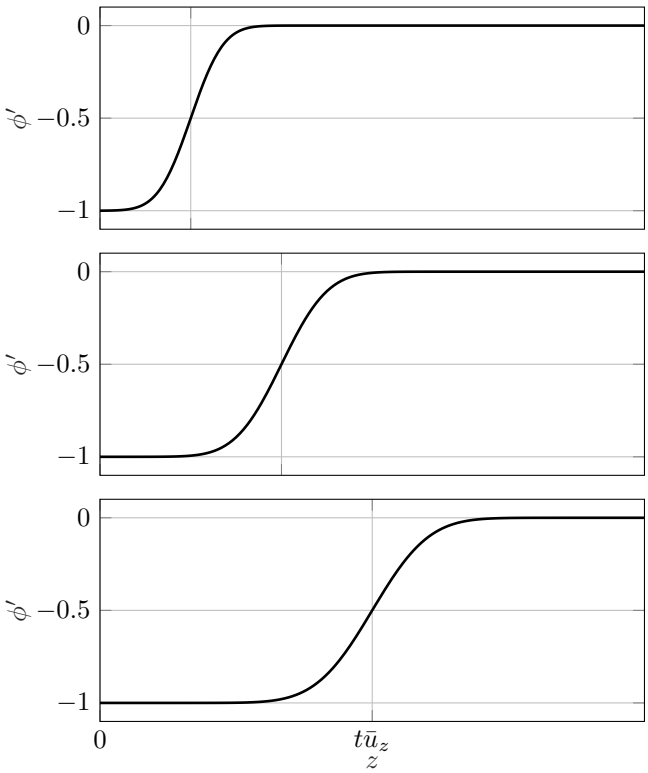

Figure 6.3: Snapshots of the equivalence ratio fluctuation field downstream of a fuel injector. The generation mechanism is the step acoustic velocity perturbation. Hence, equivalence ratio fluctuations are negative.

7 Summary and Discussion of Achievements

In this chapter, publications are summarized individually. Achievements of each publication are discussed with respect to their impact on the relevant literature.

The first publication in Sec. 7.1 recognizes the dispersive inertial wave propagation as a thermo-acoustic time delay. As revealed by several research groups [16–18], swirl fluctuations propagates faster than the convection speed. This unexpected outcome causes prediction errors in thermo-acoustic models. The dispersive propagation of inertial waves is employed to explain this speed difference. Moreover, swirl fluctuations are recognized as inertial waves. In the second publication in Sec. 7.2, these findings are further developed to explain the flame response to swirl fluctuations. In the literature, there exist different physical interpretations of the flame response mechanism [18, 61, 64]. None of these authors recognized the impact of the inertial wave. In the second publication, inertial wave eigenmode structures are used to interpret the flame response dynamics.

In the third and fourth publications (respectively in Sec. 7.3 and 7.4), improvements to the flame response models for equivalence ratio waves are introduced. Equivalence ratio fluctuations are known to be relevant for the thermo-acoustic instabilities as they cause strong heat release rate fluctuations [20, 66]. In the literature, there exist frequency domain models to predict and understand the flame response mechanisms [70, 74]. In the third publication, a time domain approach is employed to reveal characteristic time scales and the model is extended to account for the effect of molecular diffusion. In the fourth publication, the model is further improved for more realistic technically premixed flame configurations, where mixture inhomogeneities may occur in the radial direction.

The fifth publication in Sec. 7.5 introduces a convective scaling of the dominant instability frequency with the power rating in a lab scale swirl stabilized flame. Experiments were conducted a decade ago by Komarek and Polifke [16], where the dominant instability frequency changed significantly with power rating while equivalence ratio was held constant. At that time, this behavior could not be explained, as the system acoustics barely changes with power rating. In the fifth publication, the flame characteristic time scales are employed to explain these convective scaling. This publication is a good example that stresses the relevance of time scales for combustion instabilities.

7.1 Paper IW-Speed

This non-peer reviewed paper consists of a preliminary analysis of the dispersive inertial wave propagation in an axial swirler. More advanced approach is given in chapter 5. Here, the aim was to scrutinize the convective assumption for swirl waves. In several publications [16–18], it was observed that the propagation speed is faster than the convection. This unexpected behavior causes errors in thermo-acoustic models. To compensate the deviation in the propagation speed, authors added ad-hoc corrections. However, the cause remained unknown. In this paper, it was revealed that the dispersive propagation of inertial waves is the reason for deviations in the propagation speed. The seminal work by Kelvin [19] on inertial waves provides the mathematical modeling, i.e. the incompressible linearized Euler equations are used. Moreover, by employing a frequency response analysis, the propagation speed of inertial waves is quantitatively compared against a pure convective process.

The swirling flow downstream of the swirler is modeled by a solid body rotation superimposed with uniform axial velocity. By employing the modal ansatz on the linearized Euler equations, the inertial wave eigenmodes are revealed. The corresponding eigenvalues are investigated as propagation speeds. It is revealed that for each eigenmode, there exist two eigenvalues. One of them propagates faster than convection and the other one is slower than convection. The deviation from the convection speed depends linearly on the circulation strength. Higher circulation means more deviation. Moreover, each eigenmode propagates with a different level of deviation. The propagation of the first eigenmode deviates most from the convection. As the order of the eigenmode increases, the propagation approaches to convection.

The frequency response is derived for simplicity only for the first eigenmode. A downstream location is selected as a measurement plane for the tangential velocity perturbations. The pure convection process results in a unity constant gain with a linearly decaying phase. The slope of the phase corresponds to the convection speed. In an inertial wave propagation, since there exists fast and slow waves, the superposition is decisive for the gain. For particular frequencies, a destructive superposition occurs and zero gain is observed. A constructive superposition results in unity gain. Obviously, changing the location of the measurement plane varies the frequencies of constructive/destructive superposition. The results are also validated against numerical simulations.

Besides the correct characterization of the propagation speed, a precaution is mentioned for the commonly employed approach [16, 18] to identify the flame response to inertial waves. The tangential velocity perturbations measured at a plane is used as an input and the corresponding heat release rate fluctuations are used to calculate the flame transfer function. This publication reveals that this approach is not accurate. The worst case for the identification is the following: a destructive superposition occurs at the measurement plane and no tangential velocity perturbations are measured. However, the heat release rate shows finite oscillations. By the definition of the flame transfer function, the finite value (heat release rate fluctuation amplitude) is divided by a very small number (tangential velocity amplitude). The resulting gain values are unrealistic.

Contribution

The unexpected results in the propagation speed of swirl waves was recognized by Prof. Wolfgang Polifke, who suggested the research question. By employing the modal ansatz on linearized equations, accurate estimation of wave speed is conducted by myself. Moreover, I performed the numerical simulations. The draft is written by me with suggestions and corrections of Prof. Wolfgang Polifke.

7.2 Paper IW-Flame

Although experimental results [12, 13, 62] suggest that the tangential velocity perturbations generated at the swirler cause heat release rate fluctuations, these perturbations cannot be the leading mechanism. Because, no heat release rate fluctuation is generated by tangential velocity perturbations for an axisymmetric flame. Several approaches exist in literature to describe the response mechanism. Hirsch *et al.* [64] employed Biot-Savart law on the azimuthal momentum equation to derive a flame response. Based on experimental observations a black-box Gauss distribution model is proposed by Komarek and Polifke [16]. Parameters of this model were related to physical quantities of the configuration such as bulk flow velocity, flame length and the distance of the swirler from the flame base. Palies *et al.* [61] attributed the unsteady heat release rate to the turbulent flame speed variations due to the tangential velocity fluctuations. Acharya and Lieuwen [18] recognized from numerical simulations that tangential velocity perturbations generate velocity fluctuation in other directions.

In Paper IW-Speed, besides the characterization of the propagation speed of inertial waves, the eigenmode structures are recognized. Initial perturbations in tangential velocity generate also flow oscillations in other directions. This outcome is used to characterize the flame dynamics.

To perform a quantitative analysis on the interaction between inertial waves and unsteady heat release, the linearized reactive flow equations are implemented in a numerical framework with finite element method. The method is demonstrated on an idealized axisymmetric laminar swirling flame. The computed flame impulse response is then physically interpreted by considering inertial wave eigenmodes in stream-wise and radial directions. The resulting flame impulse response is similar to the turbulent flame studied by Komarek and Polifke [16]. It is revealed that only the faster propagating wave interacts with the flame. The impact of the slower wave possibly dissipates more due to viscosity, since it take much longer to reach the flame. This explains why in all publications [16, 18, 61], the observed time delays are around 40-50% less than the convective delay.

Contribution

The research question was proposed by myself. The linearized reactive flow solver is implemented by Deniz Bezgin based on preliminary template generated by me. The interpretation of results in terms of inertial wave–flame dynamics interaction is conducted by myself with the help of Deniz Bezgin. The manuscript is written by me with suggestions and corrections of the

co-authors.

7.3 Paper ϕ'-Flame

The flame response of a laminar conical Bunsen flame to equivalence ratio perturbations is investigated. The linearized level set G-equation is employed to derive the flame impulse response analytically. A time domain approach is employed, where the flame base is subject to an impulsive equivalence ratio perturbation. Three major contributions discussed by Cho and Lieuwen [70] are also identified, namely the heat of reaction contribution, laminar flame speed contribution and finally the flame surface area contribution, which indirectly results from flame front deflection caused by laminar flame speed variations. The flame response is then validated against the direct numerical simulation with reduced 2-step global chemical kinetics.

It is revealed that the flame impulse response has two relevant time scales: 1) τ_c is related to the convection of the perturbation along the flame and 2) τ_r is related to the propagation of the hypothetical restoration line that brings the perturbed flame to its original position. The restoration process is always slower than the convective process. The restoration mechanism was suggested by Blumenthal *et al.* [5] for the flame response caused by velocity fluctuations. Since it is a kinematic mechanism, it also applies to equivalence ratio fluctuations. It is demonstrated that the heat of reaction and laminar flame speed contributions have only the perturbation time scale, τ_c. The indirect flame surface area contribution has both time scales, i.e. τ_c and τ_r.

By applying Fourier transform in time to the flame impulse response, the expression for the flame transfer function in the frequency domain is retrieved. The resulting expression is identical to the one derived by Cho and Lieuwen [70] via the frequency domain approach. The advantage of the time domain approach is that the relevant time scales are revealed. The interpretation of time scales is not trivial in the frequency domain approach. Moreover, the time domain approach enables an interpretation of the superposition of contributions: Both direct contributions have always positive impulse response for a lean premixed flame, whereas the indirect contribution always results in a negative response. Since the restoration time scale affects only the indirect contribution, the global impulse response has a positive part in early times, but also a negative part in the later times, i.e. $\tau_c < t < \tau_r$. The constructive superposition of the positive and negative responses is responsible for the high gain values observed in the flame transfer function.

In the work from Cho and Lieuwen [70], 1-D advection equation is employed for modeling the propagation of the equivalence ratio perturbations. In the first part of the paper, the same model is employ to validate these results. Then, the propagation is replaced by a more realistic advection-diffusion equation model, which also accounts for the molecular diffusion of the perturbation. This model is especially relevant for the cases, where the fuel injector is positioned far from the flame. Sharp features of the flame impulse response smear out with the impact of the molecular diffusion, which improves the agreement between the model and the numerical simulation results.

Contribution

The research question was proposed jointly by all authors. The derivation of analytical models and the numerical simulations was conducted by myself. The manuscript is written by me with suggestions and corrections of co-authors.

7.4 Paper Local-ϕ'

In Paper ϕ'-Flame and also in Cho and Lieuwen [70], equivalence ratio fluctuations are assumed to be uniform over the radius. This is a strong assumption, which is not realized in practice. The analytical framework described in Paper ϕ'-Flame is extended to account for an arbitrary radial profile of equivalence ratio perturbations. This is done by assuming an impulsive perturbation localized at a given radius. The local flame impulse response is derived analytically with variable perturbation source radius. This approach is validated by integrating the local flame impulse for the uniform perturbation profile, which retrieves the expression presented in Paper ϕ'-Flame.

The local flame impulse response reveals that the heat of reaction and laminar flame speed contributions to the flame impulse response are local mechanisms. A response occurs only at the instant, when the perturbation reaches the flame. For a conical Bunsen flame, a local perturbation imposed at the center will travel the longest distance and thus yields a long convective time scale τ_c, whereas a perturbation imposed at duct walls instantly acts on the flame base and thus doesn't introduce a time lag. The indirect response from the flame surface area fluctuations is not a local process. As discussed in Paper ϕ'-Flame, it is generated by the flame speed variations, hence activated locally at τ_c. Then, the wrinkled flame surface is advected through the flame tip. The time for the wrinkle to leave the flame is related to the local restoration process and denoted as τ_r. For a conical Bunsen flame, a local perturbation imposed at the center will not introduce any restorative time scale, as it immediately leaves the flame. However, for a perturbation imposed at close to the duct walls generates a wrinkle at the flame base, which propagates till the flame tip. This causes the longest restoration time. The time scales derived in Paper ϕ'-Flame should be interpreted as global time scales that result from the weighted summation of the local time scales varying from the center to the radius of the burner duct.

By exploiting the local framework, two perturbation profiles resulting from different fuel injection systems of technically premixed flames are studied. Perturbations at the center are higher for one case and lower for the other. Corresponding flame responses are calculated analytically for these cases. The flame transfer functions show considerable difference due to the differently weighted time scales. The phase of the flame transfer function is less steep for the case with higher perturbation at the side walls.

Contribution

A need for an extended framework was recognized after the discussions with Prof. Wolfgang Polifke and Dr. Kilian Oberleithner in the framework of the FVV project (Forschungsvere-

inigung Verbrennungskraftmaschinen — Research Association for Combustion Engines). The derivation of analytical models is conducted by myself. The manuscript is written by me with suggestions and corrections of Prof. Wolfgang Polifke.

7.5 Paper Scaling

The convective scaling of peaks in the combustion noise spectrum of a bluff body stabilized turbulent swirl flame is studied. Experiments were conducted a decade ago and presented in publications by Polifke and coauthors [11, 16]. Measurement campaigns were conducted for several configurations by varying the power rating and the stream-wise location of the swirler. The noise spectrum was obtained via pressure sensors in the combustion chamber. Moreover, corresponding flame transfer functions were measured. The spectrum showed that the peak frequency scales linearly with power rating, i.e. the mean flow speed. However, this was an unexpected result, since the acoustic mode barely changes with the power rating.

In this paper, the peaks are shown to be related to burner-flame intrinsic thermo-acoustic feedback, which strongly depend on the phase of the flame transfer function. A mathematical framework is introduced to prove the convective scaling. A new criterion is derived to estimate the instability potentiality at frequencies, where the flame transfer function phase crosses $-\pi/2$. Note that this criterion differs from solely flame intrinsic thermo-acoustic criterion [78], which estimates the frequency at $-\pi$. This difference is attributed to the very large burner flow inertia due to great area jumps across mixing duct to the plenum and combustion chamber.

An increase in the bulk flow velocity due to the power rating decreases the characteristic flame time scale. This causes a less steep phase of the flame transfer function and the crossing with $-\pi/2$ phase occurs at a later frequency. This explains linear convective scaling. Similar behavior is also observed for the swirler position variation. This paper serves as good example for the impact of flame related time scales on thermo-acoustic instabilities.

Contribution

The research question was formulated in the course of discussions of all authors. The unpublished experimental results from Thomas Komarek are used. The extended criterion for the intrinsic thermo-acoustic instability is derived by me. The convective scaling was introduced by Thomas Steinbacher. The interpretation via phase diagrams and impedances was introduced by Prof. Wolfgang Polifke. The manuscript is preparation by myself, Thomas Steinbacher and Prof. Wolfgang Polifke. We kindly acknowledge the anonymous reviewers for this paper. The extended criterion was derived following their constructive comments.

8 Outlook

In Paper IW-Flame, it is observed that the flame responds to the fast propagating inertial waves, but not to the slow one. This trend should be investigated further. Two possible approaches are: 1) including the viscous dissipation of inertial waves and 2) studying the dynamics of inertial waves across the dump plane. The former is justified by the fact it takes more time for the slow propagating inertial waves to reach flame base compared to fast waves. Hence, they are more prone to the viscous dissipation. The strong area jump of the combustion chamber might have an impact on the inertial wave dynamics. This motivates the proposed second approach. The analytical framework of Paper IW-Speed can be extended to match inertial wave modes across the dump plane. Eigenmodes of the combustion chamber region can be derived by employing linearized Euler equations on simplified mean flow profiles such as the Rankine vortex. The inertial wave solution from the mixing duct region can be used as the initial condition at the dump plane and the spatio-temporal evolution inside the combustion chamber can be investigated.

The linearized reactive flow equations are demonstrated for an idealized 2-d configuration. This approach can be extended to analyze a more realistic configuration with a 3-d swirler geometry. For such cases, inertial wave structures can be studied in detail. Moreover, the numerical solution of linearized equations is much more efficient than solving non-linear equations. For 2-d cases, a perfect agreement was achieved for the linear flame response. The accuracy of the linearized framework for 3-d turbulent cases can be analyzed. Time averaged flow fields of a numerical simulation can be employed as the base flow for the linearization, where turbulence and turbulent combustion models should also be linearized appropriately.

Instead of time domain analysis of the linearized reactive flow equations, a frequency domain analysis can be performed with few modifications of the code structure. This approach is similar to the hydrodynamic global stability analysis. Yet, this reveals not only the flow instabilities but also flame instabilities and thermo-acoustic instabilities. Also, the sensitivity analysis and/or design optimization can be studied by using adjoints method, e.g. the swirler blade shape can be modified such that the flame transfer function at particular frequency is maximized or minimized.

In most of the technically premixed flame studies, stiff fuel injection is considered. As a result, equivalence ratio fluctuations are only generated by the air flow perturbations. However, if the fuel injector is not choked, the pressure fluctuations at the injector become important and the fuel velocity fluctuations generate heat release rate oscillations. For such cases, the properties of the flame response should be further studied as a multiple input system.

The equivalence ratio wave generation mechanism is modeled by the crude 1-d framework, i.e.

$$\frac{\phi'}{\bar{\phi}} = \frac{u'_F}{\bar{u}_F} - \frac{u'_O}{\bar{u}_O} \,. \tag{8.1}$$

High fidelity numerical simulations of the well-studied jet in cross-flow setup can be employed

to derive more realistic equivalence ratio generation mechanism. Similar to the flame transfer function calculations, the fuel injector transfer functions can be derived, i.e. the frequency dependent models can be achieved as

$$\frac{\phi'}{\bar{\phi}} = F_F(\omega)\frac{u'_F}{\bar{u}_F} - F_O(\omega)\frac{u'_O}{\bar{u}_O} \ . \tag{8.2}$$

This might have strong impact on the flame dynamics.

The flame response to equivalence ratio waves is derived for laminar flames. A straightforward extend is to study turbulent configurations. One interesting point is the sensitivity of the laminar flame speed. As discussed in chapter 6, the laminar flame speed fluctuation, $s'_L\left(\phi'\right)$, is one of the major contributions to the flame response. For a turbulent flame, the flame speed does not depend only on the equivalence ratio but also turbulent velocity fluctuations, i.e. $s'_T\left(\phi', u'_T\right)$. The sensitivity of the turbulent flame speed should be further investigated to correctly estimate the flame response.

List of Figures

Bibliography

[1] J. W. S. Rayleigh. The Explanation of Certain Acoustical Phenomena. *Nature*, 18:319–321, 1878. doi: 10.1038/018319a0.

[2] M. L. Munjal. *Acoustics of Ducts and Mufflers*. Wiley, Chichester, West Sussex, United Kingdom, 2nd edition, 2014. ISBN 978-1-118-44312-5.

[3] A. Fleifil, A. M. Annaswamy, Z. A. Ghoneim, and A. F. Ghoniem. Response of a Laminar Premixed Flame to Flow Oscillations: A Kinematic Model and Thermoacoustic Instability Results. *Combustion and Flame*, 106:487–510, 1996. doi: 10.1016/0010-2180(96)00049-1.

[4] T. Schuller, D. Durox, and S. Candel. A Unified Model for the Prediction of Laminar Flame Transfer Functions: Comparisons Between Conical and V-Flame Dynamics. *Combustion and Flame*, 134(1,2):21–34, 2003. doi: 10.1016/S0010-2180(03)00042-7.

[5] R. S. Blumenthal, P. Subramanian, R. Sujith, and W. Polifke. Novel Perspectives on the Dynamics of Premixed Flames. *Combustion and Flame*, 160(7):1215–1224, 2013. doi: 10.1016/j.combustflame.2013.02.005.

[6] T. Steinbacher, A. Albayrak, A. Ghani, and W. Polifke. Response of Premixed Flames to Irrotational and Vortical Velocity Fields Generated by Acoustic Perturbations. *Proceedings of the Combustion Institute*, 37(4):5367–5375, 2019. doi: 10.1016/j.proci.2018.07.041.

[7] W. Polifke. Combustion Instabilities. In J. Anthoine and A. Hirschberg, editors, *Advances in Aeroacoustics and Applications*, VKI LS 2004-05. Von Karman Institute, Rhode-St-Genèse, BE, advances i edition, March 15 - 19 2004. ISBN 2-930389-54-0.

[8] T. C. Lieuwen. *Unsteady Combustor Physics*. Cambridge University Press, New York, N.Y., USA, 2012. ISBN 978-1-107-01599-9.

[9] L. Crocco and S. I. Cheng. *Theory of Combustion Instability in Liquid Propellant Rocket Motors*. Number 8 in AGARDograph. Butterworths Science Publication, 1956.

[10] A. Giauque. *Fonctions de Transfert de Flamme et Energies Des Perturbations Dans Les Ecoulements Reactifs*. PhD Thesis, L'Institut National Polytechnique de Toulouse, Toulouse, France, 2007.

[11] L. Tay-Wo-Chong, S. Bomberg, A. Ulhaq, T. Komarek, and W. Polifke. Comparative Validation Study on Identification of Premixed Flame Transfer Function. *J. of Engineering for Gas Turbines and Power*, 134(2):021502–1–8, 2012. doi: 10.1115/1.4004183.

[12] G. A. Richards and M. J. Yip. Oscillating Combustion from a Premix Fuel Nozzle. In *Comb. Inst. / American Flame Research Committe Meeting*, San Antonio, TX, 1995.

[13] D. L. Straub and G. A. Richards. Effect of Axial Swirl Vane Location on Combustion Dynamics. In *Volume 2: Coal, Biomass and Alternative Fuels; Combustion and Fuels; Oil and Gas Applications; Cycle Innovations*, page V002T02A014, Indianapolis, Indiana, USA, 1999. ASME. doi: 10.1115/99-GT-109.

[14] N. A. Cumpsty and F. E. Marble. The Interaction of Entropy Fluctuations with Turbine Blade Rows; A Mechanism of Turbojet Engine Noise. *Proceedings of the Royal Society A: Mathematical, Physical and Engineering Sciences*, 357(1690):323–344, 1977. doi: 10.1098/rspa.1977.0171.

[15] P. Palies, D. Durox, T. Schuller, and S. Candel. Acoustic–Convective Mode Conversion in an Aerofoil Cascade. *Journal of Fluid Mechanics*, 672:545–569, 2011. doi: 10.1017/S0022112010006142.

[16] T. Komarek and W. Polifke. Impact of Swirl Fluctuations on the Flame Response of a Perfectly Premixed Swirl Burner. *Journal of Engineering for Gas Turbines and Power*, 132(6):061503, 2010. doi: 10.1115/1.4000127.

[17] P. Palies, D. Durox, T. Schuller, and S. Candel. Experimental Study on the Effect of Swirler Geometry and Swirl Number on Flame Describing Functions. *Combustion Science and Technology*, 183(7):704–717, 2011. doi: 10.1080/00102202.2010.538103.

[18] V. S. Acharya and T. C. Lieuwen. Role of Azimuthal Flow Fluctuations on Flow Dynamics and Global Flame Response of Axisymmetric Swirling Flames. In *52nd Aerospace Sciences Meeting*, National Harbor, Maryland, 2014. American Institute of Aeronautics and Astronautics. doi: 10.2514/6.2014-0654.

[19] W. Thomson. XXIV. Vibrations of a Columnar Vortex. *Philosophical Magazine*, 10(61): 155–168, 1880. doi: 10.1080/14786448008626912.

[20] J. J. Keller, W. Egli, and J. Hellat. Thermally Induced Low-Frequency Oscillations. *Zeitschrift für angewandte Mathematik und Physik (ZAMP)*, 36(2):250–274, 1985. doi: 10.1007/BF00945460.

[21] T. C. Lieuwen and B. T. Zinn. The Role of Equivalence Ratio Oscillations in Driving Combustion Instabilities in Low Nox Gas Turbines. *Symposium (International) on Combustion*, 27(2):1809–1816, 1998. doi: 10.1016/S0082-0784(98)80022-2.

[22] G. Teschl. *Ordinary Differential Equations and Dynamical Systems*. Number v. 140 in Graduate Studies in Mathematics. American Mathematical Society, Providence, R.I, 2012. ISBN 978-0-8218-8328-0.

[23] C. M. Bender and S. A. Orszag. *Advanced Mathematical Methods for Scientists and Engineers*. Springer, New York, 1999. ISBN 978-0-387-98931-0.

[24] H. von Helmholtz. *Über Discontinuirliche Flüssigkeits-Bewegungen*. Akademie der Wissenschaften zu Berlin, 1868.

[25] W. Thomson. XLVI. Hydrokinetic Solutions and Observations. *The London, Edinburgh, and Dublin Philosophical Magazine and Journal of Science*, 42(281):362–377, 1871. doi: 10.1080/14786447108640585.

[26] L. Rayleigh. On the Stability, or Instability, of certain Fluid Motions. *Proceedings of the London Mathematical Society*, s1-11(1):57–72, 1880. doi: 10.1112/plms/s1-11.1.57.

[27] O. Reynolds. An Experimental Investigation of the Circumstances Which Determine Whether the Motion of Water Shall Be Direct or Sinuous, and of the Law of Resistance in Parallel Channels. *Philosophical Transactions of the Royal Society of London*, 174: 935–982, 1883. doi: 10.1098/rstl.1883.0029.

[28] P. G. Drazin and W. H. Reid. *Hydrodynamic Stability*. Cambridge University Press, 1982.

[29] S. Chandrasekhar. *Hydrodynamic and Hydromagnetic Stability*. Oxford University Press, 1961. ISBN 0-486-31920-2.

[30] R. J. Briggs. *Electron-Stream Interaction with Plasmas*. Res. Mono. MIT, Cambridge, MA, 1964.

[31] A. Galeev and R. N. Sudan, editors. *Basic Plasma Physics*. Number v. 1-2 in Handbook of Plasma Physics. North-Holland Pub. ; Sole distributors for the U.S.A. and Canada, Elsevier Science Pub, Amsterdam ; New York : New York, N.Y, 1983. ISBN 978-0-444-86427-7 978-0-444-86645-5.

[32] R. T. Pierrehumbert and S. E. Widnall. The Two- and Three-Dimensional Instabilities of a Spatially Periodic Shear Layer. *Journal of Fluid Mechanics*, 114:59–82, 1982. doi: 10.1017/S0022112082000044.

[33] C. C. Lin. *The Theory of Hydrodynamic Stability*. Cambridge Monographs on Mechanics and Applied Mathematics. Cambridge University Press, 2 edition, 1966.

[34] S. A. Orszag. Accurate Solution of the Orr–Sommerfeld Stability Equation. *Journal of Fluid Mechanics*, 50(4):689–703, 1971. doi: 10.1017/S0022112071002842.

[35] P. Schmid and D. Henningson. *Stability and Transition in Shear Flows*. Springer, 2001.

[36] H. P. Greenspan. *The Theory of Rotating Fluids*. CUP Archive, 1968.

[37] L. D. Landau and E. M. Lifshitz. *Fluid Mechanics*, volume 6 of *Course of Theoretical Physics*. Pergamon Press, 1987.

[38] J. Pedlosky. *Geophysical Fluid Dynamics*. Springer New York, New York, NY, 1987. doi: 10.1007/978-1-4612-4650-3.

[39] Oser Hansjörg. Experimentelle Untersuchung über harmonische Schwingungen in rotierenden Flüssigkeiten. *ZAMM - Journal of Applied Mathematics and Mechanics / Zeitschrift für Angewandte Mathematik und Mechanik*, 38(9-10):386–391, 1958. doi: 10.1002/zamm.19580380909.

[40] D. Fultz. A Note on Overstability and the Elastoid-Inertia Oscillations of Kelvin, Solberg, and Bjerknes. *Journal of Meteorology*, 16(2):199–208, 1959. doi: 10.1175/1520-0469(1959)016¡0199:ANOOAT¿2.0.CO;2.

[41] A. D. McEwan. Inertial Oscillations in a Rotating Fluid Cylinder. *Journal of Fluid Mechanics*, 40(3):603–640, 1970. doi: 10.1017/S0022112070000344.

[42] L. Messio, C. Morize, M. Rabaud, and F. Moisy. Experimental observation using particle image velocimetry of inertial waves in a rotating fluid. *Experiments in Fluids*, 44(4): 519–528, 2008. doi: 10.1007/s00348-007-0410-3.

[43] P.-P. Cortet, C. Lamriben, and F. Moisy. Viscous spreading of an inertial wave beam in a rotating fluid. *Physics of Fluids*, 22(8):086603, 2010. doi: 10.1063/1.3483468.

[44] C.-G. Rossby and Collaborators. Relation Between Variations in the Intensity of the Zonal Circulation of the Atmosphere and the Displacements of the Semi-Permanent Centers of Action. *Journal of Marine Research*, 2(1):38–55, 1939. doi: 10.1357/002224039806649023.

[45] http://www.geography.hunter.cuny.edu/tbw/wc.notes/7.circ.atm/rossby_waves.htm.

[46] P. B. Rhines. Jets and Orography: Idealized Experiments with Tip Jets and Lighthill Blocking. *Journal of the Atmospheric Sciences*, 64(10):3627–3639, 2007. doi: 10.1175/JAS4008.1.

[47] F. Renac, D. Sipp, and L. Jacquin. Criticality of Compressible Rotating Flows. *Physics of Fluids*, 19(1):018101, 2007. doi: 10.1063/1.2427090.

[48] S. Arendt, D. C. Fritts, and o. Andreassen. The Initial Value Problem for Kelvin Vortex Waves. *Journal of Fluid Mechanics*, 344:181–212, 1997. doi: 10.1017/S0022112097005958.

[49] E. Greitzer, C. S. Tan, and M. B. Graf. *Internal Flows*. Cambridge Univ. Press, 2004.

[50] T. B. Benjamin. Theory of the Vortex Breakdown Phenomenon. *Journal of Fluid Mechanics*, 14(04):593, 1962. doi: 10.1017/S0022112062001482.

[51] J. L. Kerrebrock. Small Disturbances in Turbomachine Annuli with Swirl. *AIAA Journal*, 15(6):794–803, 1977. doi: 10.2514/3.7370.

[52] V. Golubev and H. Atassi. Acoustic–Vorticity Waves in Swirling Flows. *Journal of Sound and Vibration*, 209(2):203–222, 1998. doi: 10.1006/jsvi.1997.1049.

[53] C. K. W. Tam and L. Auriault. The Wave Modes in Ducted Swirling Flows. *Journal of Fluid Mechanics*, 371:1–20, 1998. doi: 10.1017/S0022112098002043.

[54] J. Beér and N. Chigier. *Combustion Aerodynamics*. Fuel and Energy Science Series. Krieger Publishing Company, 1972. ISBN 978-0-89874-545-0.

[55] N. Syred and J. Beér. Combustion in Swirling Flows: A Review. *Combustion and Flame*, 23(2):143–201, 1974. doi: 10.1016/0010-2180(74)90057-1.

[56] A. Gupta, W. Cowden, C. Strasheim, D. Lilley, and N. Syred. *Swirl Flows*. Taylor & Francis, 1984. ISBN 978-0-9961004-2-7.

[57] S. Terhaar, C. B. Bobusch, and C. O. Paschereit. Effects of Outlet Boundary Conditions on the Reacting Flow Field in a Swirl-Stabilized Burner at Dry and Humid Conditions. *J. Eng. Gas Turbines Power*, 134:111501–1 – 9, 2012. doi: 10.1115/1.4007165.

[58] S. Schimek, J. P. Moeck, and C. O. Paschereit. An Experimental Investigation of the Nonlinear Response of an Atmospheric Swirl-Stabilized Premixed Flame. *J. Eng. Gas Turbines Power*, 133(10):101502–101502, 2011. doi: 10.1115/1.4002946.

[59] Y. Huang and V. Yang. Dynamics and Stability of Lean-Premixed Swirl-Stabilized Combustion. *Progress in Energy and Combustion Science*, 35(4):293 – 364, 2009. doi: 10.1016/j.pecs.2009.01.002.

[60] S. Candel, D. Durox, T. Schuller, J. F. Bourgouin, and J. P. Moeck. Dynamics of Swirling Flames. *Annual Review of Fluid Mechanics*, 46(1):147–173, 2014. doi: 10.1146/annurev-fluid-010313-141300.

[61] P. Palies, D. Durox, T. Schuller, and S. Candel. The Combined Dynamics of Swirler and Turbulent Premixed Swirling Flames. *Combustion and Flame*, 157(9):1698–1717, 2010. doi: 10.1016/j.combustflame.2010.02.011.

[62] K. T. Kim and D. A. Santavicca. Interference Mechanisms of Acoustic/Convective Disturbances in a Swirl-Stabilized Lean-Premixed Combustor. *Combustion and Flame*, 160 (8):1441–1457, 2013. doi: 10.1016/j.combustflame.2013.02.022.

[63] S. Kaji and T. Okazaki. Propagation of Sound Waves Through a Blade Row: I. Analysis Based on the Semi-Actuator Disk Theory. *Journal of Sound and Vibration*, 11(3):339–353, 1970. doi: 10.1016/S0022-460X(70)80038-4.

[64] C. Hirsch, D. Fanaca, P. Reddy, W. Polifke, and T. Sattelmayer. Influence of the Swirler Design on the Flame Transfer Function of Premixed Flames. In *Volume 2: Turbo Expo 2005*, pages 151–160, Reno, Nevada, USA, 2005. ASME. doi: 10.1115/GT2005-68195.

[65] A. Albayrak, M. Juniper, and W. Polifke. Propagation speed of inertial waves in cylindrical swirling flows. *Manuscript submitted for publication*, 2019.

[66] J. J. Keller. Thermoacoustic Oscillations in Combustion Chambers of Gas Turbines. *AIAA Journal*, 33(12):2280–2287, 1995. doi: 10.2514/3.12980.

[67] D. L. Straub and G. A. Richards. Effect of Fuel Nozzle Configuration on Premix Combustion Dynamics. In *Int'l Gas Turbine and Aeroengine Congress & Exposition*, 98-GT-492, Stockholm, Sweden, 1998. ASME. doi: 10.1115/98-GT-492.

[68] G. Richards and M. Janus. Characterization of Oscillations During Premix Gas Turbine Combustion. *J. Eng. for Gas Turbines and Power*, 120(2):294–302, 1998. doi: 10.1115/1.2818120.

[69] T. Lieuwen, Y. Neumeier, and B. Zinn. The Role of Unmixedness and Chemical Kinetics in Driving Combustion Instabilities in Lean Premixed Combustors. *Combustion Science and Technology*, 135(1-6):193–211, 1998. doi: 10.1080/00102209808924157.

[70] J. H. Cho and T. C. Lieuwen. Laminar Premixed Flame Response to Equivalence Ratio Oscillations. *Combustion and Flame*, 140(1-2):116–129, 2005. doi: 10.1016/j.combustflame.2004.10.008.

[71] W.-P. Shih, J. G. Lee, and D. A. Santavicca. Stability and Emissions Characteristics of a Lean Premixed Gas Turbine Combustor. *Symposium (International) on Combustion*, 26 (2):2771–2778, 1996. doi: 10.1016/S0082-0784(96)80115-9.

[72] T. Lieuwen, H. Torres, C. Johnson, and B. T. Zinn. A Mechanism of Combustion Instability in Lean Premixed Gas Turbine Combustors. *J Eng Gas Turb Power*, 123(1):182–189, 2001. doi: 10.1115/1.1339002.

[73] B. B. H. Schuermans, W. Polifke, and C. O. Paschereit. Modeling Transfer Matrices of Premixed Flames and Comparison with Experimental Results. In *ASME 1999 International Gas Turbine and Aeroengine Congress and Exhibition*, ASME 99-GT-132, Indianapolis, Indiana, USA, 1999. ASME. doi: 10.1115/99-GT-132.

[74] A. P. Dowling and S. Hubbard. Instability in Lean Premixed Combustors. *Proceedings of the Institution of Mechanical Engineers, Part A: Journal of Power and Energy*, 214(4): 317–332, 2000. doi: 10.1243/0957650001537903.

[75] W. Polifke, J. Kopitz, and A. Serbanovic. Impact of the Fuel Time Lag Distribution in Elliptical Premix Nozzles on Combustion Stability. In *7th AIAA/CEAS Aeroacoustics Conference*, AIAA 2001-2104, Maastricht, The Netherlands, 2001. doi: 10.2514/6.2001-2104.

[76] B. C. Bobusch, B. Ćosić, J. P. Moeck, and C. Oliver Paschereit. Optical Measurement of Local and Global Transfer Functions for Equivalence Ratio Fluctuations in a Turbulent Swirl Flame. *J Eng Gas Turb Power*, 136(2):021506–021506, 2013. doi: 10.1115/1.4025375.

[77] C. J. Lawn and W. Polifke. A Model for the Thermoacoustic Response of a Premixed Swirl Burner, Part II: The Flame Response. *Combustion Science and Technology*, 176(8): 1359–1390, 2004. doi: 10.1080/00102200490461623.

[78] M. Hoeijmakers, V. Kornilov, I. Lopez Arteaga, P. de Goey, and H. Nijmeijer. Intrinsic Instability of Flame-Acoustic Coupling. *Combustion and Flame*, 161(11):2860–2867, 2014. doi: 10.1016/j.combustflame.2014.05.009.

A Reproduction of Publications

The paper ”Propagation velocity of inertial waves in cylindrical swirling flow” was submitted to and was presented at the 23rd International Congress on Sound and Vibration (ICSV23) held in Athens, Greece, from 10 to 14 July 2016. It was published in the ICSV23 Congress Proceedings under the copyright of the International Institute of Acoustics and Vibration (IIAV.)

23rd International Congress on Sound & Vibration
Athens, Greece 10-14 July 2016
ICSV23

PROPAGATION VELOCITY OF INERTIAL WAVES IN CYLINDRICAL SWIRLING FLOW

Alp Albayrak and Wolfgang Polifke
Professur für Thermofluiddynamik, Technische Universität München,
Boltzmannstr. 15, D-85748 Garching, Germany

email: albayrak@tfd.mw.tum.de

Inertial waves are observed in swirl burners, due to the acoustic waves crossing the swirl generators. These waves can significantly modify the flame response in terms of flame transfer function because the propagation mechanisms are different for acoustic and inertial waves. Acoustic waves propagate at the speed of sound, whereas inertial waves travel with convection. Small changes in burner configuration may convert the constructive superposition of flame responses to a destructive one, or vice versa, which may change the flame transfer function. Therefore, it is necessary to identify the propagation mechanisms correctly. The aim of this paper is to re-examine the assumption that inertial waves travel with convection. An analytical approach is combined with numerical simulations to determine and validate the propagation speed with emphasis on the impact of different swirl strengths.

1. Introduction

Lower emission of pollutants in gas turbines requires leaner fuel mixture for combustion process. This increases the likelihood of occurrence of combustion instability, which is caused by a feedback mechanism between acoustic waves and heat release rate fluctuations from the flame. In order to design safer and more reliable gas turbines, it is necessary to investigate the interaction between acoustic/hydrodynamic perturbation and flame dynamics.

Swirl burners are ubiquitous in combustion technology, because swirl promotes fuel/air mixing and flame stabilization. This work focuses on inertial waves generated by acoustic waves that propagate across the swirl generator. Inertial waves are understood to have a significant impact on the dynamic response of swirl flames to flow perturbations.

Richards and co-workers [1, 2, 3] studied the effects of the swirl vane location on thermo-acoustic stability. The sensitivity of the flame was credited to the phase lag between pressure and heat release rate. A convective time lag model is introduced for the tangential velocity perturbations that are generated at the swirler and propagate towards the flame front. In other words, overall flame response is the superposition of responses to tangential velocity and acoustic perturbations.

Komarek and Polifke [4] confirmed this scenario and showed individual Flame Transfer Functions (FTF) for the swirl waves and the acoustic axial velocity perturbations at burner mouth. The phase difference between these FTFs is then used to investigate how strongly constructive / destructive superposition can strongly modulate the gain of the overall FTF. Palies *et al.* [5, 6] modeled the generation and the propagation of these waves by the actuator disk theory by Cumpsty and Marble [7], where the tangential velocity perturbations are assumed to travel with convection. Kim and Santavicca [8] also confirmed the interference mechanism by FTF measurements.

However, it was noted already by Straub and Richards [3] that the convective time lag model leads to poor agreement against experiments. Similarly, Polifke and co-workers [4, 9] argued that the propagation speed of the swirl (inertial) waves differs from the convective speed.

The convective propagation assumption is scrutinized in this paper. Kerrebrock [10], Golubev and Atassi [11], and Tam and Auriault [12] investigated the interaction mechanism between the acoustic and inertial waves using space–time Fourier transformed linearized compressible Euler equations. They found non-convective behavior of the inertial waves, which is not influenced strongly by the compressibility in the range of Mach number 0.3.

In this work, an analytical expression for the inertial wave propagation is proposed by neglecting the compressibility. Using space–time Fourier transformed linearized incompressible Euler equations, an analytical description of the inertial wave propagation is proposed. Distinct modes appear, since the inertial waves are dispersed. These distinct modes propagate faster and slower than the convective speed. It is shown that the strength of the swirl affects the deviation from the convection. The analytical approach is then validated against the CFD simulations using OpenFOAM.

In Sec. 2.1, the space–time Fourier transform is applied to advection equation. The same approach is then applied to linearized Euler equations in Sec. 2.2 to investigate the inertial wave propagation. In Sec. 3 a simple example is shown for a solid body rotation in a duct, where the inertial wave propagation is quantified by a transfer function. Finally, in Sec. 4 the approach is validated against CFD simulations with a non-linear incompressible Navier-Stokes solver by OpenFoam.

2. Theory

The cylindrical swirling flows in most burners are incompressible. The interaction between acoustic and hydrodynamic waves is negligible and both can be investigated separately. Linearized incompressible Euler equations are employed in this work to describe the inertial wave propagation.

For all derivations there are common assumptions, i.e. the mean radial velocity being zero $\bar{u}_r = 0$, the mean axial velocity being uniform $\bar{u}_z(r) = \bar{u}_z$, the flow being axisymmetric $\partial(.)/\partial\theta$ and developed $\partial(.)/\partial z$.

The theory section is divided into two. In the first subsection, the assumption of the convective propagation mechanism for tangential velocity perturbations is revisited. The space–time Fourier transform is applied to advection equation. The propagation is quantified by a transfer function between the area averaged perturbations sampled at the upstream and downstream locations. In the second subsection, same approach is applied to linearized Euler equations that govern inertial waves.

2.1 Propagation of convective perturbations

The axisymmetric linearized advection equation for the tangential velocity perturbations u'_θ reads as

$$\frac{\partial u'_\theta}{\partial t} + \bar{u}_z \frac{\partial u'_\theta}{\partial z} = 0\,, \tag{1}$$

where $(.)'$ denotes perturbed and $\bar{(.)}$ mean quantities, u is velocity and (z, r, θ, t) are axial, radial and tangential coordinates and time, respectively.

Although this equation can directly be solved in time domain, the space–time Fourier transformation $(.)' = \hat{(.)}\exp(-i\omega t + ikz)$ is performed in order to be consistent with Sec. 2.2. This transformation leads to an algebraic equation as dispersion relation $D(k, \omega) = 0$ that reads as

$$k(\omega) = \omega/\bar{u}_z, \tag{2}$$

where ω is the angular frequency and k is the axial wave-number. The perturbation in space–time

domain can be reconstructed by inverse Fourier transform as

$$u'_\theta(z,t) = \int_{-\infty}^{\infty} \left[\sum_{n=1}^{N} \hat{u}_\theta \exp\left(ik_n(\omega) z \right) \right] \exp(-i\omega t)\, \mathrm{d}\omega \,, \tag{3}$$

where N is the number of characteristic waves resulting from dispersion relation. For the advection equation there is only one characteristic wave $N = 1$ with convective phase speed $c_p = w/k = \bar{u}_z$.

A transfer function $T(\omega)$ can be introduced to quantify the propagation. The area averaged tangential velocity perturbation is measured at particular upstream 'z_u' and downstream 'z_d' positions and used as input and output, respectively. The transfer function reads

$$T(\omega) = \frac{\int_0^{r_o} 2\pi r \left[\sum_{n=1}^{N} \hat{u}_{\theta,n} \exp(ik_n z_d) \right] \mathrm{d}r}{\int_0^{r_o} 2\pi r \left[\sum_{n=1}^{N} \hat{u}_{\theta,n} \exp(ik_n z_u) \right] \mathrm{d}r} \,. \tag{4}$$

The input plane is chosen as $z_u = 0$ without loss of generality. The transfer function for the advection equation can be written as

$$T(\omega) = \exp\left(\frac{i\omega z_d}{\bar{u}_z} \right) \,, \tag{5}$$

whose gain and phase are $|T(\omega)| = 1$ and $\angle T(\omega) = \omega z_d / \bar{u}_z$, respectively (see Fig. 2 in Sec. 3).

2.2 Propagation of inertial waves

The linearized Euler equations in cylindrical coordinates read as

$$\frac{u'_r}{r} + \frac{\partial u'_r}{\partial r} + \frac{\partial u'_z}{\partial z} = 0 \,, \tag{6}$$

$$\frac{\partial u'_z}{\partial t} + \bar{u}_z \frac{\partial u'_z}{\partial z} + u'_r \frac{\partial \bar{u}_z}{\partial r} = -\frac{1}{\rho} \frac{\partial p'}{\partial z} \,, \tag{7}$$

$$\frac{\partial u'_r}{\partial t} + \bar{u}_z \frac{\partial u'_r}{\partial z} - \frac{2\bar{u}_\theta u'_\theta}{r} = -\frac{1}{\rho} \frac{\partial p'}{\partial r} \,, \tag{8}$$

$$\frac{\partial u'_\theta}{\partial t} + \bar{u}_z \frac{\partial u'_\theta}{\partial z} + u'_r \frac{\partial \bar{u}_\theta}{\partial r} + \frac{u'_r \bar{u}_\theta}{r} = 0 \,, \tag{9}$$

where p is pressure. Other variables are defined in Sec. 2.1. Space–time Fourier transformed equations can be written as a second order ODE for $\hat{u}_r$ as

$$\frac{d^2 \hat{u}_r}{dr^2} + \frac{1}{r} \frac{d\hat{u}_r}{dr} - \hat{u}_r \left(\frac{1}{r^2} + k^2 - \frac{2k^2 \bar{u}_\theta}{(w - \bar{u}_z k)^2 r^2} \frac{\partial(\bar{u}_\theta r)}{\partial r} \right) = 0 \,. \tag{10}$$

This equation requires prescribed mean tangential velocity $\bar{u}_\theta(r)$. For particular cases such as solid body rotation $\bar{u}_\theta(r) = Kr$, free vortex $\bar{u}_\theta(r) = K/r$ or uniform tangential velocity $\bar{u}_\theta(r) = K$, the analytical solution can be found.

Two boundary conditions are required for $\hat{u}_r(r)$, which define the dispersion relation $D(k,\omega) = 0$. The phase speed c_p corresponds to the propagation speed of the inertial waves. The propagation can be quantified by the transfer function defined in Eq. (4).

3. Illustrative example: Solid body rotation in a duct

For the ease of illustration, the analysis is carried out for a duct with radius of $r_o = 5$ mm. The uniform constant axial velocity profile is used $\bar{u}_z = 10$ m/s. The tangential velocity is prescribed as a solid body rotation $\bar{u}_\theta(r) = Kr$, where $K = 2000$ s^{-1}. The corresponding Reynolds Number is $Re = 6667$ lying in turbulent regime.

The symmetry condition at center is translated to a boundary condition $\hat{u}_r(0) = 0$. Second boundary condition $\hat{u}_r(r_o) = 0$ is from the impermeability condition at duct wall. The analytical solution reads as

$$\hat{u}_{\theta,n}(r) = c_n J_1(A_n r) + d_n Y_1(A_n r) \ , \tag{11}$$

$$\hat{u}_{r,n}(r) = \frac{\bar{u}_z k_n - \omega}{2Ki} \left[c_n J_1(A_n r) + d_n Y_1(A_n r) \right] \ , \tag{12}$$

$$\hat{u}_{z,n}(r) = \frac{A_n(\bar{u}_z k_n - \omega)}{2K k_n} \left[c_n J_0(A_n r) + d_n Y_0(A_n r) \right] \ , \tag{13}$$

$$\hat{p}_n(r) = -\frac{A_n(\bar{u}_z k_n - \omega)^2 \rho}{2K k_n^2} \left[c_n J_0(A_n r) + d_n Y_0(A_n r) \right] \ , \tag{14}$$

where $A_n = k_n \sqrt{4K^2 - (\bar{u}_z k_n - \omega)^2} / (\bar{u}_z k_n - \omega)$ and J and Y are the Bessel functions of first and second kind, respectively. J and Y are orthogonal functions, which form complete solution.

Since Y_1 goes to infinity at $r = 0$, the boundary condition $\hat{u}_r(0) = 0$ cannot be satisfied unless the coefficients of Y vanish $d_n = 0$. Applying the second boundary condition $\hat{u}_r(r_o) = 0$, the dispersion relation $D(k, \omega)$ can be formed as

$$J_1(A_n r_o) = 0 \Rightarrow A_n r_o = j_n \ , \forall n \in \mathbb{N}^+ \ , \tag{15}$$

where j_n are the roots of Bessel function of first kind J_1. Axial wave-numbers $k_n(\omega)$ can be determined explicitly by solving fourth order polynomial. This indicates that for each n there exist four axial wave-numbers that have the same mode shape. Two of them propagate upstream while one grows and the other decays, which are assumed to be unphysical (see Sec. 3.1).

Other two waves are addressed as inertial waves and propagate downstream (neither growing nor decaying) at different speeds, one is faster '+' and the other is slower '−' than the convection. In left part of Fig. 1, the dispersion relation defined in Eq. (15) is represented. Roots indicate eigenvalues as axial wave-numbers, where x-axis is the normalized phase velocity $c_p^* = \omega / (k\bar{u}_z)$.

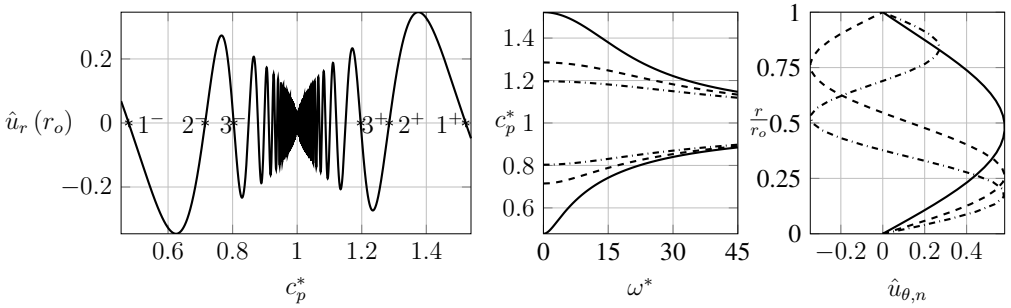

Figure 1: Left: Second boundary condition $\hat{u}_{r,n}(r_0) = 0$ as a function of normalized phase speed $c_p^* = \omega / (k\bar{u}_z)$ for $\omega = 100$ rad/s, $U_z = 10$ m/s, $K = 2000$ s^{-1} and $r_o = 5$ mm. Zeros corresponds to the eigenvalues: '+' and '−' indicating faster and slower waves than convection $c_p^* = 1$, respectively. Middle: Normalized phase speeds for the first three modes including both '+' and '−' as a function of normalized angular frequency $\omega^* = \omega z_d / \bar{u}_z$. Right: The eigenvectors of tangential velocity perturbation component $\hat{u}_{\theta,n}$ for the first three slower '−' modes. $n = 1$ (——), $n = 2$ (- · - · -), $n = 3$ (- - -).

The normalized phase speed can be written explicitly as

$$c^*_{p,n} = 1 \pm \frac{2K}{\bar{u}_z} \frac{r_o}{\sqrt{k^2 r_o^2 + j_n^2}} \,, \tag{16}$$

which shows the effect of the circulation strength K on the propagation of inertial waves. As circulation strength increases, the deviation from convection increases too. The normalized phase speed as a function of normalized angular frequency $\omega^* = \omega z_d / \bar{u}_z$ for the first three modes $n = 1, 2, 3$ is shown in the middle part of Fig. 1. As n increases, the phase speed approaches the convective speed. Moreover, the phase speed depends on the angular frequency. At low frequencies the propagation deviates from the convection the most. For high frequencies, both fast '+' and slow '−' propagation speeds approach the convection. Additionally, the inertial waves are not only perturbations in tangential velocity, but also in radial and axial directions. This is evident from Eqs. (11), (12) and (13).

The eigenvectors of the tangential velocity perturbation component $\hat{u}_{\theta,n}$ related to three outermost slower waves '−' are illustrated in the right part of Fig. 1 as a function of radius. Although the modes corresponding to the faster waves '+' are not plotted, they are equal to the negative of the slower wave modes. As n increases, the modes become more oscillatory.

3.1 Construction of boundary condition regarding number of characteristics

Linearized compressible Euler equations for perfect gas can be described by five field variables $[\rho', p', u'_z, u'_r, u'_\theta]$ and corresponding five transport equations. Related to the transport equations there are five characteristic waves, namely two acoustic waves (propagating downstream and upstream), the convective entropy wave and two inertial waves. The latter are studied in this paper.

Assuming the flow is incompressible, the energy equation is decoupled from the system of equations and therefore, the entropy wave is eliminated. The incompressible system is described by four field variables $[u'_z, u'_r, u'_\theta, p']$ and four partial differential equations. The type of pressure equation changes from hyperbolic to elliptic. The non-local behavior of the elliptic equation modifies the nature of the acoustic waves making their propagation speed infinite. The incompressible equations have, therefore, only two inertial waves as characteristics, which contradicts Eq. (15) that has four characteristics. In this paper, the upward propagating waves are postulated to be unphysical and related to modified spurious acoustic waves.

In order to construct a well-posed problem, the boundary condition at inlet $z = 0$ should be defined for each variable $[u'_z, u'_r, u'_\theta, p']$. As there exist only two characteristics, the variables cannot be chosen freely, otherwise non-local waves (spurious acoustic waves) are triggered, which cannot be described as space–time Fourier transform. However, in order to be consistent with the actuator disk theory [5, 6, 7], a perturbation in tangential velocity $\hat{u}_\theta = f_\theta(r)$ is imposed. Other components of the velocity perturbation are set to zero and the pressure perturbation is set as Neumann boundary condition.

For simplicity, the tangential velocity perturbation at the inlet is assumed as the first mode shape $f_\theta(r) = J_1(j_1 r / r_o)$ shown with solid line in the right part of Fig. 1. Since Bessel functions form an orthogonal basis, the modes other than $n = 1$ are not excited. In this case, the coefficients are calculated as the following set of equations for $\hat{u}_\theta, \hat{u}_r, \hat{u}_z$ respectively

$$1 = -c_{1_+} + c_{1_-} + c_{1_u} \,, \tag{17}$$

$$0 = -\frac{\bar{u}_z k_{1_+} - \omega}{2Ki} c_{1_+} + \frac{\bar{u}_z k_{1_-} - \omega}{2Ki} c_{1_-} + \frac{\bar{u}_z k_{1_u} - \omega}{2Ki} c_{1_u} \,, \tag{18}$$

$$0 = \frac{A_{1_+}(\bar{u}_z k_{1_+} - \omega)}{2K k_{1_+}} c_{1_+} + \frac{A_{1_-}(\bar{u}_z k_{1_-} - \omega)}{2K k_{1_-}} c_{1_-} + \frac{A_{1_u}(\bar{u}_z k_{1_u} - \omega)}{2K k_{1_u}} c_{1_u} \,, \tag{19}$$

where subscript "u" stands for the upward propagating growing wave. The upward propagating decaying wave is neglected, because in downstream direction, it acts as if the wave is growing, which

ruins the transfer function. Since three characteristics are used for construction of perturbation, the pressure boundary condition is neglected too. The resulting coefficients are frequency dependent and can be approximated by $c_{1+} \approx -0.5$, $c_{1-} \approx 0.5$ and $c_{1u} \approx 0$. It is straightforward to construct any type of perturbation similarly, which can be expressed as a summation of Bessel function of first kind J_1.

The perturbation in space–time domain at a downstream location can be constructed by considering only inertial waves

$$u'_\theta(z,r,t) = J_1\left(j_1\frac{r}{r_o}\right)\int_{-\infty}^{\infty}\Big[-c_{1+}\exp\left(ik_{1+}z\right)+c_{1-}\exp\left(ik_{1-}z\right)\Big]\exp\left(-i\omega t\right)\mathrm{d}\omega\ . \tag{20}$$

3.2 Derivation of transfer function

The transfer function defined in Eq. (4) can be simplified as

$$T\left(\omega\right) = -c_{1+}\exp\left(ik_{1+}z_d\right)+c_{1-}\exp\left(ik_{1-}z_d\right)\ . \tag{21}$$

In Fig. 2 the gain and the phase are plotted at downstream position $z_d = 3r_o = 15$mm with the solid line (——) and compared against the convective model with the dashed line (- - - -). The CFD results are indicated with the (◦) symbol and explained in Sec. 4. In the first two columns, the slow and fast modes are analyzed separately. Each mode independently shows a constant gain $|T\left(\omega\right)| = 1$ and a phase deviating from the convective phase as expected. For fast mode, the phase is steeper than the convection at low frequencies and becomes parallel for higher frequencies. This agrees well with phase speeds shown in the middle part of Fig. 1, where the phase speeds approach the convective speed as frequency increases. The similar arguments can be made for the slow mode. The complete inertial wave propagation is described by the superposition of the two modes as shown in the third column. The constructive superposition results in gain values around $|T\left(\omega\right)| \approx 1$ and the destructive superposition results around $|T\left(\omega\right)| \approx 0$. The superposition in the phase results in almost convective phase. This might be misleading, since the propagation is far from being convective.

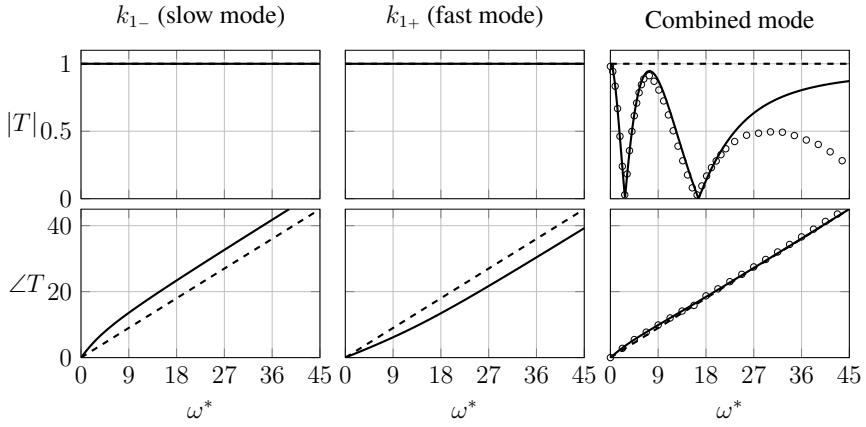

Figure 2: Comparison of the Bode plots for inertial wave (——), convective wave (- - - -) and CFD results (◦). First two columns show slower k_1^- and faster k_1^+ modes, respectively and the third column shows the combined mode.

The Fig. 3 shows the gain plots $|T\left(\omega\right)|$ for output locations, $z_d = 3r_o = 15$ mm and $z_d = 6r_o = 30$ mm. As the downstream position z_d increases, more destructive superpositions exist and the frequencies shift. This characteristic of inertial waves is very crucial for experiments and CFD simulations of real swirl generators, where the source of the inertial wave is not well known. Since

the tangential velocity perturbations measured at upstream location z_u is the denominator in Transfer Function $T(\omega)$, a destructive superposition results in $T(\omega) \to \infty$. This behavior is not observed in the case presented in this paper, because the upstream reference position is located at inlet $z_u = 0$, where the perturbations are generated and there is no possibility for destructive superposition.

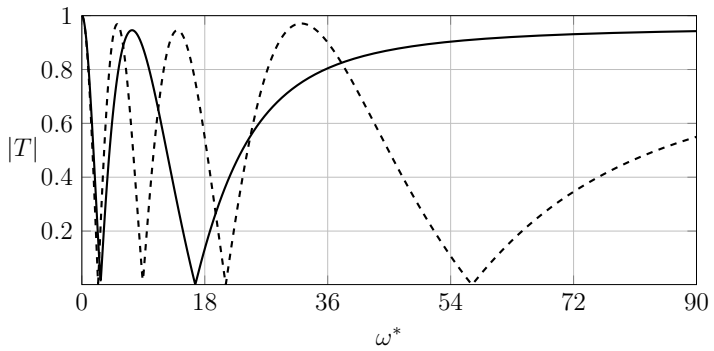

Figure 3: Gain plot for $z_d = 3r_o = 15$mm (——) and $z_d = 6r_o = 30$mm (- · - · -).

4. Comparison against CFD results

The CFD simulations are performed for the same configuration as described in Sec. 3 using OpenFOAM. The transient incompressible Navier-Stokes equations are solved using PIMPLE algorithm. The slip wall boundary conditions are used to match the inviscid analytical approach. The tangential velocity perturbations are generated at the inlet boundary condition by broad-band excitation. Then, the transfer function is constructed by Wiener-Hopf inversion [13].

As shown in Fig. 2, a good agreement is achieved between CFD results and analytical model for the low and moderate frequencies. For high frequencies, the CFD simulations show low pass behavior due to the viscous dissipation, which is not present in the analytical approach. However, very high frequencies are not relevant for the linear combustion dynamics. Therefore, those frequencies can be neglected and reliable results can still be obtained.

5. Conclusion

In order to investigate the inertial wave propagation, space–time Fourier transformation is applied to linearized incompressible Euler equations. The transformed equations are solved analytically as a second order ODE, where infinite number of waves with phase speeds diverging from convection are revealed. It is shown that the phase speed of the inertial waves depends on mean tangential velocity. As mean tangential velocity increases, the deviation from convection increases too. By defining a transfer function between tangential velocity perturbations at different locations, the inertial wave propagation is compared against the convective propagation by considering a solid body rotation in a duct. The analytical model is successfully validated against numerical simulations. The model can be coupled with low order models for more reliable estimation of thermo-acoustic stability. It is also possible to build a velocity perturbation model that can be used to study the impact of inertial waves on the flame dynamics.

Acknowledgments

The presented work is part of the Marie Curie Initial Training Network Thermo-acoustic and aero-acoustic nonlinearities in green combustors with orifice structures (TANGO). We gratefully acknowledge the financial support from the European Commission under call FP7-PEOPLE-ITN-2012.

REFERENCES

1. Richards, G. A. and Yip, M. Oscillating combustion from a premix fuel nozzle, *The Combustion Institute/ American Flame Research Committee Meeting, San Antonio, TX (United States)*, (1995).

2. Straub, D. L., Richards, G. A., Yip, M. J., Rogers, W. A. and Robey, E. H. Importance of axial swirl vane location on combustion dynamics for lean premix fuel injectors, *34th AIAA/ASME/SAE/ASEE Joint Propulsion Conference and Exhibit*, Cleveland, OH, USA, Jul., (1998).

3. Straub, D. L. and Richards, G. A. Effect of axial swirl vane location on combustion dynamics, *ASME 1999 International Gas Turbine and Aeroengine Congress and Exhibition*, pp. V002T02A014–V002T02A014, American Society of Mechanical Engineers, (1999).

4. Komarek, T. and Polifke, W. Impact of Swirl Fluctuations on the Flame Response of a Perfectly Premixed Swirl Burner, *Journal of Engineering for Gas Turbines and Power*, **132** (6), 061503–1,7, (2010).

5. Palies, P., Durox, D., Schuller, T. and Candel, S. The combined dynamics of swirler and turbulent premixed swirling flames, *Combustion and Flame*, **157**, 1698–1717, (2010).

6. Palies, P., Schuller, T., Durox, D. and Candel, S. Modeling of premixed swirling flames transfer functions, *Proceedings of the Combustion Institute*, **33** (2), 2967 – 2974, (2011).

7. Cumpsty, N. and Marble, F. The interaction of entropy fluctuations with turbine blade rows; a mechanism of turbojet engine noise, *Proceedings of the Royal Society of London A: Mathematical, Physical and Engineering Sciences*, vol. 357, pp. 323–344, The Royal Society, (1977).

8. Kim, K. T. and Santavicca, D. A. Interference mechanisms of acoustic/convective disturbances in a swirl-stabilized lean-premixed combustor, *Combustion and Flame*, **160** (8), 1441–1457, (2013).

9. Tay-Wo-Chong, L., Komarek, T., Kaess, R., Föller, S. and Polifke, W. Identification of flame transfer functions from LES of a premixed swirl burner, *Proceedings of ASME Turbo Expo 2010*, Glasgow, UK, Jun., GT2010-22769, ASME, (2010).

10. Kerrebrock, J. L. Small disturbances in turbomachine annuli with swirl, *AIAA Journal*, **15** (6), 794–803, (1977).

11. Golubev, V. V. and Atassi, H. M. Acoustic-Vorticity Waves in Swirling Flows, *Journal of Sound and Vibration*, **209** (2), 203–222, (1998).

12. Tam, C. K. and Auriault, L. The wave modes in ducted swirling flows, *Journal of Fluid Mechanics*, **371**, 1–20, (1998).

13. Polifke, W. Black-box system identification for reduced order model construction, *Annals of Nuclear Energy*, **67C**, 109–128, (2014).

Special Issue – TANGO

International journal of spray and combustion dynamics

International Journal of Spray and Combustion Dynamics
0(0) 1–10

DOI: 10.1177/1756827717747201
journals.sagepub.com/home/scd
SAGE

Response of a swirl flame to inertial waves

Alp Albayrak, Deniz A Bezgin and Wolfgang Polifke

Abstract

Acoustic waves passing through a swirler generate inertial waves in rotating flow. In the present study, the response of a premixed flame to an inertial wave is scrutinized, with emphasis on the fundamental fluid-dynamic and flame-kinematic interaction mechanism. The analysis relies on linearized reactive flow equations, with a two-part solution strategy implemented in a finite element framework: Firstly, the steady state, low-Mach number, Navier–Stokes equations with Arrhenius type one-step reaction mechanism are solved by Newton's method. The flame impulse response is then computed by transient solution of the analytically linearized reactive flow equations in the time domain, with mean flow quantities provided by the steady-state solution. The corresponding flame transfer function is retrieved by fitting a finite impulse response model. This approach is validated against experiments for a perfectly premixed, lean, methane-air Bunsen flame, and then applied to a laminar swirling flame. This academic case serves to investigate in a generic manner the impact of an inertial wave on the flame response. The structure of the inertial wave is characterized by modal decomposition. It is shown that axial and radial velocity fluctuations related to the eigenmodes of the inertial wave dominate the flame front modulations. The dispersive nature of the eigenmodes plays an important role in the flame response.

Keywords

Flame response, inertial waves, swirling flows, linearized Navier–Stokes equations, finite element method, reactive flows

Date received: 15 May 2017; accepted: 20 November 2017

1. Introduction

Thermo-acoustic combustion instabilities have been a subject of intensive studies, with important applications in power and propulsion systems. One important aspect is the flame transfer function (FTF), which describes the response of the flame heat release rate to flow perturbations. In the literature, a wide variety of studies can be found, ranging from low order models[1–3] to high fidelity numerical simulations,[4,5] with the objective to determine the FTF and to understand the underlying physics.

For premixed swirling flames, the flame dynamics comprises several acoustic-flow-flame interaction mechanisms, see e.g. the overview given in Section 5 of the lecture notes by Polifke.[6] *Rotational waves* – also known as *inertial waves*[7] in fluid dynamics – generated by acoustic waves propagating across the swirl generator have received increased attention in recent years.[8–13]

The overall flame dynamics results from superposition of the various interaction mechanisms. Straub and Richards[8] demonstrated the importance of this superposition by changing the axial position of the swirler within a fuel nozzle, which resulted in a significant alteration of the combustor stability. The corresponding sensitivity of the FTF to swirler position was confirmed experimentally and numerically by Komarek and Polifke[10] and explained in terms of the different time scales of acoustic and inertial waves. Simple models for the response functions of the respective contributions to the overall FTF were formulated in terms of distributed delays, but the fluid-dynamic mechanism by which inertial waves modulate the heat release rate of the flame was not analyzed.

Hirsch et al.[9] modeled the overall FTF of a swirl flame by considering the transport equation for

Faculty of Mechanical Engineering, Technical University of Munich, Munich, Germany

Corresponding author:
Alp Albayrak, Thermo-Fluid Dynamics Group, Technical University of Munich, Boltzmannstr. 15, Garching D-85748, Germany.
Email: albayrak@tfd.mw.tum.de

perturbations of azimuthal vorticity. Effective *secondary* velocity fluctuations, which result from vorticity fluctuations, were then computed with the Biot–Savart law. Palies et al.[11,12] modeled inertial waves as convective tangential velocity perturbations, adopting actuator disk theory proposed by Cumpsty et al.[14] and Cumpsty and Marble.[15] The corresponding flame response was modeled by the level set method. It was argued that the tangential velocity perturbations change the turbulent burning speed, thus causing heat release rate fluctuations. Acharya and Lieuwen[13] observed in numerical simulations that tangential velocity perturbations generate axial as well as radial flow fluctuations, which contribute to the flame response.

The objective of the present study is to gain further insight into the fluid mechanics of swirl flame response to flow perturbations. An academic configuration, i.e. a laminar swirling flame is investigated. Linearized reactive flow (LRF) equations are formulated and solved to compute the respective impulse responses (IRs) to perturbations of axial and tangential velocity. Axisymmetric inertial waves with three-dimensional modal structure[16,17] are observed to have a significant impact on the flame shape and overall surface area.

In the first part of this paper, we propose a method for accurate and fast estimation of FTFs based on LRF equations. Linearized Navier–Stokes equations are commonly used for stability analysis of non-reactive flows. Recently, Qadri[18] extended this approach for reactive flows by including the linearized species transport equation with Arrhenius type one-step chemistry. A slightly different approach was proposed by Blanchard et al.[19] to estimate the flame response by direct numerical linearization over a steady state solution of a reactive flow simulation. Qualitative agreement with experiments was achieved. In both studies, steady state solutions were achieved via transient simulation combined with selective frequency damping.

In the present work, Newton's method is employed to obtain the steady state solution. Instead of relying on direct numerical linearization, the governing equations are linearized analytically. Transient simulations are performed to obtain the IRs. The corresponding FTFs are retrieved by fitting a discrete finite IR model to the time series data. Results are quantitatively validated against the experiment from Kornilov et al.[5] for a laminar Bunsen flame.

In the second part, the LRF-based method for computation of FTFs is applied to a swirling laminar flame. IRs for both flame response contributions are computed, the interaction between inertial waves and the flame front kinematics is explicated with the help of snapshots of the flow fields. Following Albayrak and Polifke,[17] a modal decomposition is applied and the perturbation structures are characterized as dispersive waves with non-zero components in axial, radial and azimuthal coordinate directions. Their distinct Bessel function type eigenmodes are shown to be important for the flame response. In particular, the structure of the inertial wave eigenmodes implies that a tangential velocity perturbation induces axial as well as radial velocity perturbations, which modulate the flame front and thus generate heat release rate perturbations.

2. LRF model for the flame response

This section presents the approach for FTF computations based on LRF equations. The set of governing equations for a low Mach number flow reads as

$$\nabla \cdot \boldsymbol{u} = \frac{1}{\rho c_p T}[\nabla \cdot (\lambda \nabla T) + \dot{\omega}_T] \tag{1a}$$

$$\frac{\mathrm{D}\boldsymbol{u}}{\mathrm{D}t} = -\frac{1}{\rho}\nabla p + \frac{1}{\rho}\nabla \cdot (\mu \nabla \boldsymbol{u}) \tag{1b}$$

$$\frac{\mathrm{D}Y_F}{\mathrm{D}t} = \frac{1}{\rho c_p}[\nabla \cdot (\lambda \nabla Y_F) + \dot{\omega}_F] \tag{1c}$$

$$\frac{\mathrm{D}T}{\mathrm{D}t} = \frac{1}{\rho c_p}[\nabla \cdot (\lambda \nabla T) + \dot{\omega}_T] \tag{1d}$$

$$p_0 = \rho R T \tag{1e}$$

where $\boldsymbol{u}$ is flow velocity vector, ρ is density, c_p is heat capacity at constant pressure, λ is the thermal conductivity, μ is the dynamic viscosity, T is temperature, $\dot{\omega}_T$ is the heat release rate, $\dot{\omega}_F$ is the reaction rate, Y_F is the mass fraction of fuel, R is the specific gas constant, p_0 is the thermodynamic pressure, p is hydrodynamic pressure.

The above set of equations was derived for binary air-fuel mixture under the following assumptions: In lean hydrocarbon/air flames, the properties of air dominate the mixture and the heat capacity of the mixture is close to that of air. Furthermore, the value of heat capacity is changing only slightly over a wide temperature range. Therefore, heat capacity of air and fuel is assumed to be equal and independent of temperature. In hydrocarbon/air flames, Lewis number changes only slightly across the flame front. In many theoretical approaches, the Lewis number of all species is set to unity, see Poinsot and Veynante.[20] Accordingly, we assume the Lewis number of fuel to be unity. Majda and Lamb[21] proposed a low Mach number assumption for combustion at low Mach numbers and strong heat release. The low Mach number assumption splits the pressure into a thermodynamic and a hydrodynamic pressure component.[22] Following Williams[23] and Poinsot and Veynante,[20] the reaction rate term $\dot{\omega}_F$ for

a premixed flame is modeled by an irreversible one-step Arrhenius law

$$\dot{\omega}_F = -A\rho Y_F \exp^{-\beta/\alpha} \exp\left(-\frac{\beta(1-C)}{1-\alpha(1-C)}\right) \quad (2)$$

where $C = (T - T_1)/(T_2 - T_1)$ is the normalized temperature and α, β and the preexponential factor A are model parameters. Further explanation of the model parameters is given in the Appendix. The heat release rate $\dot{\omega}_T = -\Delta h^0_{f,F}\dot{\omega}_F$ is calculated with the mass enthalpy of formation of fuel $\Delta h^0_{f,F}$. Sutherland's viscosity model is made use of

$$\mu = \frac{A_s T^{3/2}}{T + S} \quad (3)$$

The temperature dependence of the thermal conductivity λ is modeled as

$$\lambda = \lambda_1 \frac{T}{T_1} \quad (4)$$

where λ_1 is the thermal conductivity of the fluid at inflow temperature T_1, see Williams.[23]

The steady state solution of equation (1) is computed using Newton's method. Using these base solutions, the linearized equations (see equation (15) in Appendix) are solved in time domain. The goal is to compute the linear flame dynamics, in particular the flame IR.

The sets of equations (1) and (15) were implemented in the finite element method framework Freefem++.[24] P2-P1 Taylor-Hood elements are used, i.e. velocity, temperature and mass fraction are discretized by second order polynomials, while first-order polynomials are used for pressure. Solution algorithms for the steady state case and the linearized unsteady dynamics are described in the next subsections.

The numerical methods were validated against CFD simulations (OpenFOAM) and experiments on a Bunsen flame by Kornilov et al.[5] and Duchaine et al.[25] results are presented below. Further information on the FreeFem++ model constants, OpenFOAM simulations and the experimental setup can be found in the Appendix.

2.1. Steady state computations

The governing equations are nonlinear due to the convective terms and the combustion model. Newton's method finds a solution for a nonlinear system of equations of type $F(\boldsymbol{x}) = 0$ by an iterative process, which starts from an initial guess $\boldsymbol{x}_0$

$$\boldsymbol{x}_{n+1} = \boldsymbol{x}_n - (J_F(\boldsymbol{x}_n))^{-1} F(\boldsymbol{x}_n) \quad n = 0, 1, 2, \ldots, \quad (5)$$

where $\boldsymbol{x} = [\boldsymbol{u}, T, Y_F, p]$ denotes the field variables and J_F stands for the Jacobian matrix of $F(\boldsymbol{x})$.

Newton's method converges if the initial guess is sufficiently close to the solution, i.e. within the convergence radius of the problem. To provide such an initial guess, we employ the low Reynolds and low Peclet number limit ($Re, Pe \to 0$) of the governing equations. In this limit, the Navier–Stokes equations reduce to Stokes equations, while the energy and species transport equations reduce to pure diffusion equations. The use of Stokes equation as an initial guess for solving the Navier–Stokes equations NSE via Newtons method is well documented in the literature, see Kim et al.[26] Furthermore, the convergence radius is enlarged by artificially increasing the values of viscosity μ and thermal conductivity λ by a factor of ten. Once the convergence is achieved, the diffusive coefficients are decreased by 5% and Newton's method is re-started. This loop is carried on until the correct values of viscosity and thermal conductivity are retrieved.

Convergence of Newton's method is checked by evaluating the error

$$err = \sum \frac{|\delta \boldsymbol{x}|_\infty}{|\boldsymbol{x}|_\infty} \quad (6)$$

where $|\cdot|_\infty$ is the L-infinity norm and δ is the increment between two consecutive iteration steps in Newton's method. The diffusive coefficients are reduced, whenever $err < 0.1$. Iterations cease once the viscous terms μ, λ attain their physical values and the error $err < 10^{-5}$.

The resulting mean flow fields and flame shapes compare well against OpenFOAM results, see Figures 1 and 2, which show the spatial distributions of axial velocity and heat release rate, respectively. Both figures show normalized quantities, i.e. $u_z/\max(u_z)$ and $\dot{\omega}_T/\max(\dot{\omega}_T)$, thus the colormap ranges from 0 to 1. Simulations with fixed wall temperature – see the right plot – show a slight deviation in flame shape, because combustion parameters of the one-step chemistry model were fitted to the adiabatic case, while OpenFOAM uses a two-step chemistry model from the literature.[27] Further information on the OpenFOAM simulation setup is given in the Appendix.

2.2. Linearized dynamics computations

A linearization of equation (1) is described in the Appendix. As in the steady case, P2-P1 Taylor-Hood elements are employed for the spatial discretization of these equations. Implicit Backwards Euler scheme is used to advance in time. The convective terms are discretized with Characteristic Galerkin method.[28]

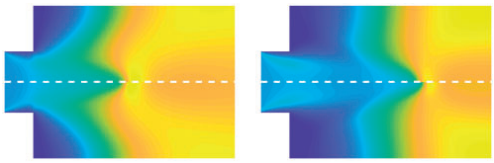

Figure 1. Comparison of the normalized axial velocity field. Left: Adiabatic. Right: Fixed temperature walls. Upper half: OpenFOAM. Lower half: FreeFEM++.

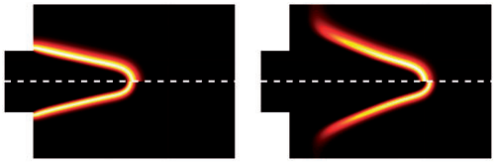

Figure 2. Comparison of the normalized heat release rate. Left: Adiabatic. Right: Fixed temperature walls. Upper half: OpenFOAM. Lower half: FreeFEM++.

In the LRF framework, there exists no noise contribution as the initial state is stationary. Therefore, the flame response is simply obtained by an impulsive perturbation in inlet flow velocity $u'_z = \bar{u}_z \varepsilon \delta(t)$. It is important to note that this perturbation is equivalent to an acoustic wave in a compressible framework. The Dirac impulse is approximated by a normal distribution, i.e.

$$\delta(t) \approx \frac{1}{a\sqrt{\pi}} \exp^{-(t/a)^2} \tag{7}$$

where a is the standard deviation and should be close to zero to approximate the Dirac function accurately. However, very small values are not feasible numerically. In this work, the value of $a = 0.1$ ms is chosen such that $a < \tau_{IR}/20$, where τ_{IR} indicates the IR length. This is appropriate for the frequency range of 0–1000 Hz.

By definition, the flame IR $h(t)$ is the normalized heat release rate fluctuations caused by the impulsive velocity perturbation and reads as

$$h(t) \equiv \frac{\dot{Q}'(t)}{\bar{\dot{Q}}\varepsilon} \tag{8}$$

where $\dot{Q} = \int \dot{\omega}_T \mathrm{d}V$ is the global heat release rate. The IR contains the same information as FTF. It is also possible to retrieve the corresponding FTF by fitting a discrete-time finite IR model to the IR.

Figures 3 and 4 prove that the FreeFEM++ simulation of the linearized dynamics achieves good quantitative agreement for both IR and FTF. For the

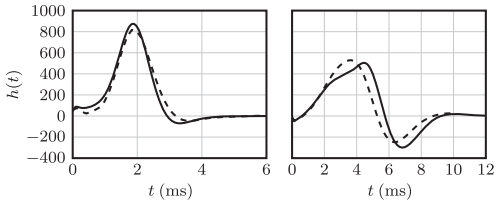

Figure 3. IR of the laminar flame with adiabatic (left) and isothermal (right) walls. The adiabatic flame OpenFOAM (- - -) and FreeFEM++ (——).

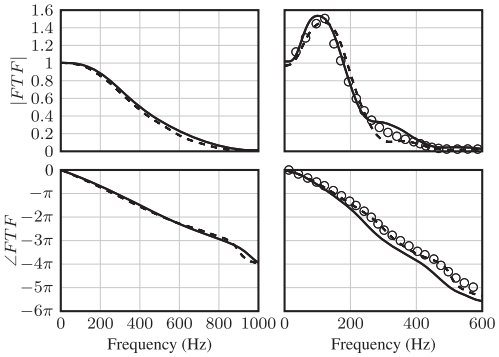

Figure 4. FTF of Kornilov flame.
Left: Adiabatic. Right: Fixed wall temperature. OpenFOAM (- - -), FreeFEM++ (——) and experiments [5] (○).

isothermal walls, the FTF results match well with the experiments[5] and also the OpenFOAM simulations. For the cases with adiabatic walls, good agreement is also met. Here, the comparison is only shown against the OpenFOAM simulations, as there are no experimental data available.

3. Case study: A swirling flame

After validation of the proposed numerical method with the example of slit flames, we proceed to a laminar swirling V-flame stabilized on a bluff body, see Figure 5. A 2D domain with cylindrical symmetry is considered, with inner and outer radii of the annular duct $r_i = 1$ mm and $r_o = 2$ mm, respectively. The duct length between the swirler – which is not included in the computational domain, but assumed to be located just upstream of the inlet boundary – and the combustion chamber is 5 mm.

Following Kerrebrock,[16] the flow profile at the inlet is approximated by an uniform axial velocity and a solid body rotation, i.e.

$$\bar{\boldsymbol{u}} = [\bar{u}_z, 0, Kr] \tag{9}$$

where $K = 1000\mathrm{s}^{-1}$ is the circulation and $\bar{u}_z = 2$ m/s.

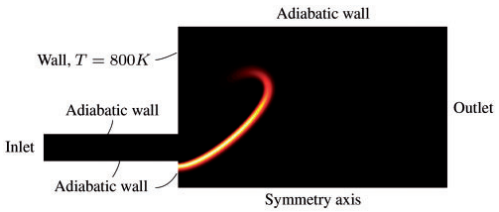

Figure 5. Normalized heat release rate of swirling V-flame.

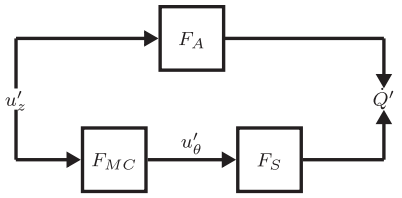

Figure 6. Major contributions to the response of a swirl flame to an acoustic perturbation, c.f. Figure 9 in Komarek and Polifke.[10]

First the steady mean fields are computed. Figure 5 shows the steady state heat release rate field. In order to anchor a V-flame, the upper side wall and the combustion chamber wall are cooled to 800 K. Subsequently, LRF equations are solved to compute the IR caused by velocity perturbations upstream of the swirler. Since the swirler is excluded, the perturbation structure at the swirler exit should be modeled. This is done by the actuator disk theory following Palies et al.,[11,12] which introduces two different velocity perturbations. One of them is the upstream *axial* velocity perturbation itself, which is conserved throughout the swirler due to continuity. The corresponding flame response mechanism is illustrated in the upper branch of Figure 6 denoted by F_A. The other perturbation occurs in the tangential velocity due to Kutta condition and should be identified as the source of an *inertial wave*.[7] As will be shown below, axial as well as radial velocity perturbations result, which have distinct mode structures. The first block F_{MC} in the lower branch of Figure 6 stands for the mode conversion from acoustic axial velocity to inertial wave. The second block F_S stands for the corresponding *swirl* component of the flame response.

Since the present approach is linear, the velocity perturbations can be applied separately. Similar to the Bunsen flame calculations in the previous section, we first compute the IRs. To account for the first contribution, an axial velocity perturbation at the inlet is introduced as

$$u'_z(z=0,t) = \bar{u}_z \varepsilon \delta(t) \tag{10}$$

For the inertial wave contribution, the Kutta condition is applied, i.e. the tangential velocity perturbation is defined as $u'_\theta = u'_z \tan\alpha$, where α indicates the swirl angle. By applying modal decomposition on the linearized Navier–Stokes equations, Albayrak and Polifke[17] showed that any tangential velocity perturbation can be constructed by modes. $M_j(m_k r)$ is the j-th eigenmode and given by

$$M_j(xr) = J_j(xr) - \frac{J_1(xr_o)}{Y_1(xr_o)} Y_j(xr) \tag{11}$$

where J_j and Y_j are the first and second kind of Bessel function, respectively. These eigenmodes are found analytically by deriving the dispersion relation and applying the impermeability condition as $u'_r = 0$ at annular duct walls. For simplicity, the perturbation is approximated by the first eigenmode

$$u'_\theta(z=0,t) \approx \bar{u}_z \tan(\alpha) \varepsilon \chi_1 M_1(m_1 r) \delta(t) \tag{12}$$

where m_k is the k-th positive root of $M_1(xr_i) = 0$ for x. The prefactor χ of the eigenmodes is calculated through

$$\chi_k = \frac{\int_{r_i}^{r_o} r M_1(m_k r) \mathrm{d}r}{\int_{r_i}^{r_o} r M_1(m_k r)^2 \mathrm{d}r} \tag{13}$$

Two separate simulations are performed with the above boundary conditions, i.e. equations (10) and (12). Again, the Dirac delta function is approximated by a normal distribution function with small standard deviation. The corresponding heat release rate fluctuations describe the IRs denoted by h_A and h_S, which are plotted in Figure 7(c). In the following subsection, the IR results are interpreted.

3.1. Interpretation of the response to inertial waves

Since the configuration is 2D axisymmetric, a tangential velocity perturbation by itself does not generate any heat release rate fluctuations. The swirl contribution to the flame response is generated through the axial and radial velocity perturbations that result from inertial waves. As explicated in a previous study,[17] the modal decomposition applied on a swirling flow generates also perturbations of axial and radial velocity. Since we approximated the tangential velocity perturbation at the swirler exit only with the first eigenmode (see equation (12)), the corresponding eigenmodes for axial and radial velocity perturbations read

$$\hat{u}_r \propto M_1(m_{1,1} r) \tag{14a}$$

$$\hat{u}_z \propto M_0(m_{1,1} r) \tag{14b}$$

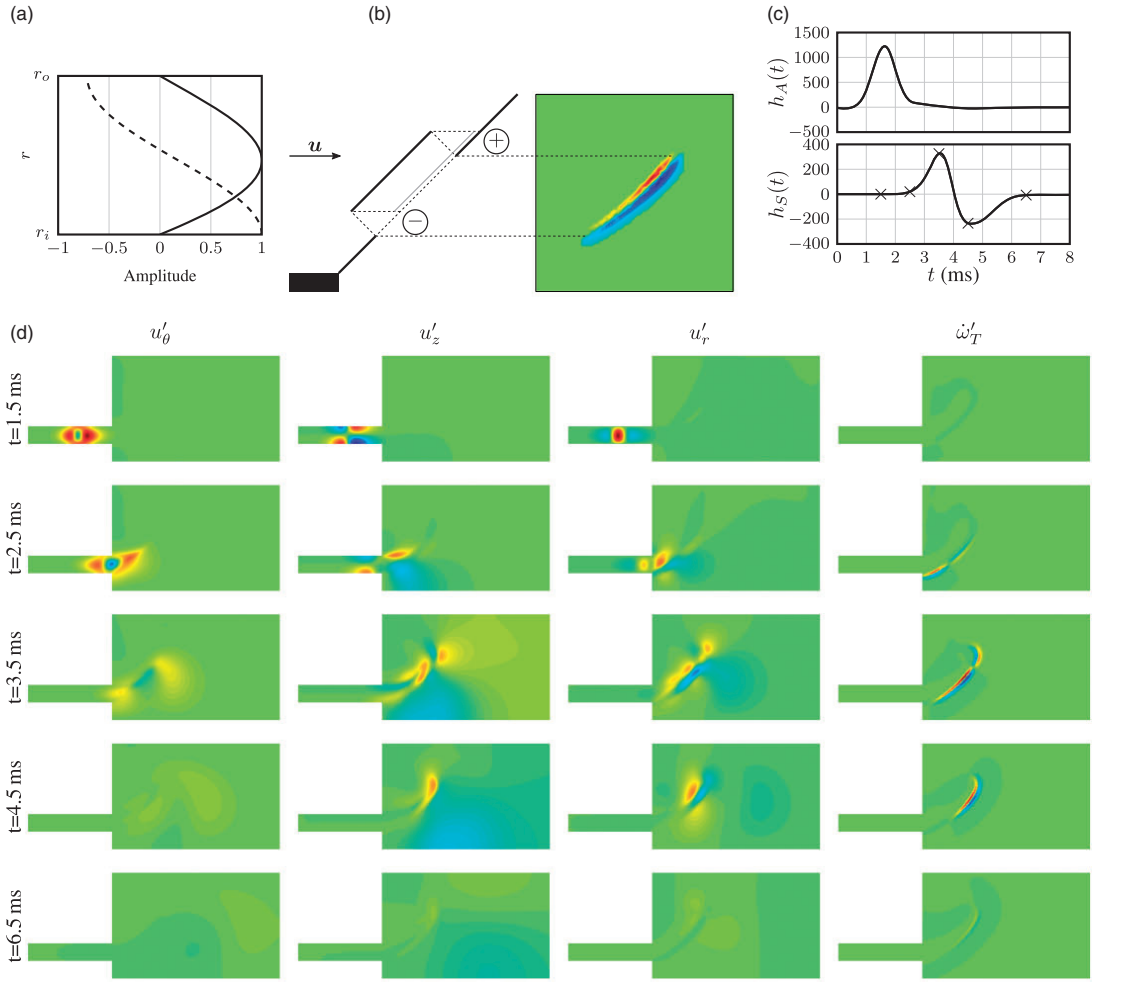

Figure 7. Response of flame front to an inertial wave generated by a perturbation of tangential velocity at the inlet. (a) Normalized eigenmode of $\hat{u}_z$ (- - -); $\hat{u}_\theta$ and $\hat{u}_r$ (——). (b) Sketch of a flame perturbed by negative axial velocity. Left: Level-set framework. Right: $\dot{\omega}'_T$ in LRF framework. (c) Flame impulse responses to axial (top) and tangential (bottom) perturbation. Crosses indicate times of snapshots shown in Figure 7(d). (d) Snapshots of normalized tangential, axial, radial velocities and heat release rate (from left to right) after an impulsive perturbation of tangential velocity.

The eigenfunction profiles are plotted against the duct radius in Figure 7(a). The amplitudes in x-axis are normalized with the maximum values. These profiles are also observed in the snapshots in Figure 7(d), which depict the results of the IR simulation with tangential velocity perturbation as defined in equation (12). All quantities in the snapshots are normalized with maximum values. Thus, the range of the colormaps is from –1 (blue) to 1 (red).

The tangential and radial velocities (shown in the first and third columns, respectively) exhibit the pattern of the $M_1(m_{1,1}r)$ eigenmode. In the third column, the axial velocity perturbations are shown, which have a $M_0(m_{1,1}r)$ eigenmode pattern. All velocity perturbations exhibit dispersive behavior in the axial direction during the propagation in the duct (see Albayrak and Polifke[17]), which is clearly seen in the first row. For example, in axial velocity perturbation, a pocket of a wave travels in front and followed by another wave pocket with a negative sign.

In the last column of Figure 7(d), the linearized heat release rates are presented. We interpret the source terms by the level-set approach proposed by Blumenthal et al.[2] The correspondence between the LRF framework and the level-set approach is demonstrated in Figure 7(b). A snapshot of a flame

is illustrated, which is perturbed by a negative axial velocity perturbation. In the level-set framework (left plot), the flame is moved towards upstream due to the kinematic balance between the flow velocity and the flame speed. The perturbed flame surface generates a deficit and an overlap in flame surface area as indicated in the figure with – and + signs, respectively. The change in the flame surface area can be easily visualized by projecting the perturbed flame to the unperturbed flame. As discussed by Blumenthal et al.,[2] the unsteady heat release rate is generated by the flame surface area fluctuations. In the linearized heat release rate $\dot{\omega}_T$ framework (right plot), the movement of the flame surface can be understood as a positive $\dot{\omega}'_T$ in the upstream region and a negative $\dot{\omega}'_T$ in the downstream region.

The shape of the IR caused by a tangential velocity perturbation (see Figure 7(c)) is explained using the snapshots in Figure 7(d). The first row in the snapshots corresponds to the simulation time of 1.5 ms. At this time, no heat release rate fluctuation is generated (see lower part in Figure 7(c)) as the inertial waves still propagates through the duct and did not reach the flame yet. The negative axial velocity region around the inner duct wall arrives first at the flame base and displaces the flame in the upstream direction. In level-set framework, this is characterized by a leading overlap (denoted by a plus sign in Figure 7(b)) and a following gap (denoted by a minus sign in Figure 7(b)) in flame surface area. It is important to note that when assessing the net influence of a pocket, the leading part has a stronger weight due to a larger radius compared to the following part. Therefore, the IR starts with a positive contribution. At a slightly later time, the positive axial velocity perturbation around the outer duct wall arrives to the flame and displaces the flame towards downstream, which causes a negative contribution. Both, the impact of the negative (inner wall) and positive (outer wall) axial velocity perturbations can be observed in the $\dot{\omega}'_T$ plot at 2.5 ms with a sign change in the middle of the flame. Combination of these both effects yields a weakly positive slope of the IR at early times. The downstream displaced flame reaches the flame tip and the corresponding flame surface area gap leaves the domain, i.e. the maximum IR is observed at 3.5 ms. After this point, the flame response starts to sink. This trends continues till the upstream displaced flame, caused by the negative velocity perturbation at the inner wall, reaches the flame tip at 4.5 ms. The only remaining gap is then convected through the flame surface till the initial flame is recovered around 6.5 ms. This is also called as the restoration mechanism by Blumenthal et al.[2]

Although the configuration is simplified, we argue that it is an ideal case to study the flame-flow interaction mechanisms without complication. This strong argument can be supported by the following observations: (1) By definition, the FTF is a global quantity as the heat release rate is integrated over the whole flame surface. Therefore, impact of turbulence related flame wrinkles on the FTF is negated. (2) In swirling flows, there exist unstable coherent structures, i.e. precessing vortex cores that are particularly important for the burner stability (see Oberleithner et al.[29]). However, the energy content of these structures clustered at a distinct high frequency, which is not explicitly related to the inertial waves generated at the swirler.

The IRs in Figure 7(c) show qualitative similarities with results of Komarek and Polifke[10] for a turbulent swirling flame, i.e. the axial velocity contribution shows a Gaussian-like positive IR and the inertial wave contribution has a positive response followed by a negative. The integral of the axial velocity contribution gives one, whereas the inertial wave contribution gives zero. These values are also in agreement with the low frequency limit of the FTF described by Polifke and Lawn.[30] Two distinct time lags are observed. The axial perturbation contribution has zero time lag (in low Mach number framework, the speed of sound is infinity). The swirl contribution has a convective time lag (≈ 2 ms), which is related to the distance from the swirler to the flame. This also confirms the actuator disk model by Palies et al.[11,12] Our approach further suggests that the tangential velocity perturbations generate axial and radial perturbations, which disturb the flame front and cause heat release rate fluctuations. This is not predicted by the actuator disk model, where the turbulent flame speed modulations caused by the tangential velocity perturbations are the major cause of the flame response. Moreover, the inertial wave structures brings a physical explanation to the work from Acharya and Lieuwen,[13] where the generation of axial and radial velocity perturbations is observed in numerical simulations.

4. Conclusion

An idealized swirling flame is investigated with emphasis on the mechanism of flame response to tangential velocity perturbations. We identify these perturbations as inertial waves, which are accurately described by linear theory. A method based on LRF equations is thus developed to identify the flame IR. The linear framework is ideal to scrutinize the interaction between inertial waves and a swirl flame. Linearized low Mach number Navier–Stokes equations with reduced order one-step chemistry are implemented in a finite element method framework in order to describe flame dynamics. The solution algorithm consists of two parts: First, Newton's method is employed to find the steady state

solution. Then, the LRF equations are solved with an impulsive flow perturbation to obtain the flame IR. This approach is thoroughly validated for a laminar Bunsen flame.

The approach is then applied to a swirling flame. By analyzing the snapshots of the perturbed LRF fields, characteristics of the response of the flame to a tangential velocity perturbation are elucidated. Inertial waves comprise perturbations in all three velocity components; fluctuations of heat release rate are explained in terms of the kinematic balance of flame front propagation with the axial and radial velocity components.

The results bring new insight to the dynamics of swirling flames and can be used to explain some previous results. Acharya and Lieuwen[13] observed in numerical simulations that the acoustic waves crossing the swirler generate hydrodynamic waves, which generate unsteady heat release. Similarly, Hirsch et al.[9] attributed the cause of the unsteady heat release to the secondary velocity fluctuations using the azimuthal vorticity equations. We can precisely identify these flow structures as inertial waves, and compute their spatio-temporal evolution. Note that the argument of Palies et al.,[11,12] i.e. that flame response is caused by changes in turbulent flame speed that result from swirl number variations, cannot be applied to the present laminar swirl flame.

A possible extension of this work is to apply the approach to a realistic configuration with turbulence to study 3D structures. Solution of the Reynolds-averaged Navier–Stokes equations (RANS), time averaged reactive flow fields from large eddy simulation (LES) or experiment can be used as the linearization point. The LRF is a powerful tool for fast and accurate IR estimations. Moreover, it can be easily converted to a linear eigenvalue problem, which can be used for the global stability and sensitivity analysis.

Acknowledgements

The presented work is part of the Marie Curie Initial Training Network *Thermo-acoustic and aero-acoustic nonlinearities in green combustors with orifice structures* (TANGO).

Declaration of Conflicting Interests

The author(s) declared no potential conflicts of interest with respect to the research, authorship, and/or publication of this article.

Funding

The author(s) disclosed receipt of the following financial support for the research, authorship, and/or publication of this article: We gratefully acknowledge the financial support from the European Commission under call FP7-PEOPLE-ITN-2012.

References

1. Schuller T, Durox D and Candel S. A unified model for the prediction of laminar flame transfer functions: comparisons between conical and V-flame dynamics. *Combust Flame* 2003; 134: 21–34.
2. Blumenthal RS, Subramanian P, Sujith R, et al. Novel perspectives on the dynamics of premixed flames. *Combust Flame* 2013; 160: 1215–1224.
3. Cho JH and Lieuwen TC. Laminar premixed flame response to equivalence ratio oscillations. *Combust Flame* 2005; 140: 116–129.
4. Tay-Wo-Chong L, Bomberg S, Ulhaq A, et al. Comparative validation study on identification of premixed flame transfer function. *J Eng Gas Turb Power* 2012; 134: 8.
5. Kornilov VN, Rook R, ten Thije Boonkkamp JHM, et al. Experimental and numerical investigation of the acoustic response of multi-slit Bunsen burners. *Combust Flame* 2009; 156: 1957–1970.
6. Polifke W. Combustion instabilities. In: Anthoine J and Hirschberg A (eds) *Advances in aeroacoustics and applications*. Rhode-St-Genèse: Von Karman Institute, 2004, pp.22–33.
7. Gallaire F and Chomaz JM. Instability mechanisms in swirling flows. *Phys Fluids* 2003; 15: 2622–2639.
8. Straub DL and Richards GA. Effect of axial swirl vane location on combustion dynamics. In: *International gas turbine and aeroengine congress & exhibition*, Indianapolis, Indiana, 7–10 June 1999. New York, NY: ASME.
9. Hirsch C, Fanaca D, Reddy P, et al. Influence of the swirler design on the flame transfer function of premixed flames. In: *ASME turbo expo*, Reno, NV, USA, 6–9 June 2005, pp.151–160. New York, NY: American Society of Mechanical Engineers.
10. Komarek T and Polifke W. Impact of swirl fluctuations on the flame response of a perfectly premixed swirl burner. *J Eng Gas Turb Power* 2010; 132: 7.
11. Palies P, Durox D, Schuller T, et al. The combined dynamics of swirler and turbulent premixed swirling flames. *Combust Flame* 2010; 157: 1698–1717.
12. Palies P, Schuller T, Durox D, et al. Modeling of premixed swirling flames transfer functions. *Proc Combust Inst* 2011; 33: 2967–2974.
13. Acharya V and Lieuwen T. Role of azimuthal flow fluctuations on flow dynamics and global flame response of axisymmetric swirling flames. In: *52nd aerospace sciences meeting*, National Harbor, Maryland, 13–17 January 2014.
14. Cumpsty NA, Nicholas A and Marble FE. The generation of noise by the fluctuations in gas temperature into a turbine. Technical Report CUED/A TURBO/TR57, Cambridge, England, 1974.
15. Cumpsty N and Marble F. The interaction of entropy fluctuations with turbine blade rows; a mechanism of turbojet engine noise. *Proc Royal Soc Lond A* 1977; 357: 323–344.

16. Kerrebrock JL. Small disturbances in turbomachine annuli with swirl. *AIAA J* 1977; 15: 794–803.
17. Albayrak A and Polifke W. Propagation velocity of inertial waves in cylindrical swirling flow. In: *23nd interntional congress on sound and vibration (ICSV23)*, Athens, Greece, 10–14 July 2016. Auburn University, Alabama: IIAV.
18. Qadri UA. *Global stability and control of swirling jets and flames*. PhD Thesis, University of Cambridge,UK, 2014.
19. Blanchard M, Schuller T, Sipp D, et al. Response analysis of a laminar premixed M-flame to flow perturbations using a linearized compressible Navier-Stokes solver. *Phys Fluids* 2015; 27: 043602.
20. Poinsot T and Veynante D. *Theoretical and numerical combustion*. 2nd ed. Philadelphia: Edwards, R. T. Incorporated, 2005. [ISBN 1-930217-10-2].
21. Majda A and Lamb KG. Simplified equations for low Mach number. *Dynam Issues Combust Theor* 2012; 35: 167.
22. McMurtry PA, Jou W-H, Riley J, et al. Direct numerical simulations of a reacting mixing layer with chemical heat release. *AIAA J* 1986; 24: 962–970.
23. Williams FA. *Combustion theory*. 2nd ed. Boston, Massachusetts, US: Addison-Wesley Publishing Company, 1985.
24. Hecht F. New development in freefem++. *J Numer Math* 2012; 20: 251–265.
25. Duchaine F, Boudy F, Durox D, et al. Sensitivity analysis of transfer functions of laminar flames. *Combust Flame* 2011; 158: 2384–2394.
26. Kim SD, Lee YH and Shin BC. Newton's method for the Navier-Stokes equations with finite-element initial guess of stokes equations. *Comput Math Appl* 2006; 51: 805–816.
27. Bibrzycki J, Poinsot T and Zajdel A. Investigation of laminar flame speed of Ch4/N2/O2 and Ch4/Co2/O2 mixtures using reduced chemical kinetic mechanisms. *Arch Combust* 2010; 30: 287–296.
28. Pironneau O. On the transport-diffusion algorithm and its applications to the Navier-Stokes equations. *Numer Math* 1982; 38: 309–332.
29. Oberleithner K, Sieber M, Nayeri CN, et al. Three-dimensional coherent structures in a swirling jet undergoing vortex breakdown: stability analysis and empirical mode construction. *J Fluid Mech* 2011; 679: 383–414.
30. Polifke W and Lawn CJ. On the low-frequency limit of flame transfer functions. *Combust Flame* 2007; 151: 437–451.
31. Weller HG, Tabor G, Jasak H, et al. A tensorial approach to computational continuum mechanics using object-oriented techniques. *Comput Phys* 1998; 12: 620–631.

Appendix

The experimental setup is described in detail by Kornilov et al.[5] A perfectly premixed lean Methane-air flame with equivalence ratio is $\phi = 0.8$ is considered in a multi slit burner. Center to center distance between two slits is 5 mm. Both, the duct radius and the length are both 1 mm. Since the flow is laminar and axisymmetric, only one-half of one slit flame is chosen as the numerical domain. The plenum does not modify the flow profiles in the combustion region and thus is excluded. The flame is stabilized on the wall that is cooled to temperature of $T = 373$ K. The bulk flow velocity in the duct is 1 m/s and the inflow temperature is $T_1 = 293$ K. Thermal conductivity at inflow is $\lambda_1 = 0.0257$ W/(mK).

The CFD simulations are performed in OpenFOAM, which is a finite volume solver.[31] Second-order spatial discretization (Gaussian integration with central differences) and time integration (backward) schemes are employed. The modified version of reactingFOAM is used, i.e. low Mach number assumption and Schmidt number of 0.7. Reduced two step chemistry mechanism 2S-CM2 as described by Bibrzycki et al.[27] is used to model the Methane-air combustion.

The linearized version of equation (1) that is implemented in FreeFem++ reads

$$\begin{aligned}&\left(\rho'\bar{T} + \bar{\rho}T'\right)\nabla\cdot\boldsymbol{u}' + \bar{\rho}\bar{T}\nabla\cdot\bar{\boldsymbol{u}} \\ &\quad = \frac{1}{c_p}\left[\nabla\cdot\left(\lambda'\nabla\bar{T} + \bar{\lambda}\nabla T'\right) + (\dot{\omega}_T)'\right]\end{aligned} \tag{15a}$$

$$\begin{aligned}&\bar{\rho}\left(\frac{\overline{\mathrm{D}}\boldsymbol{u}'}{\overline{\mathrm{D}}t} + \boldsymbol{u}'\cdot\nabla\bar{\boldsymbol{u}}\right) + \rho'\bar{\boldsymbol{u}}\cdot\nabla\bar{\boldsymbol{u}} \\ &\quad = -\nabla p' + \nabla\cdot\left(\mu'\nabla\bar{\boldsymbol{u}} + \bar{\mu}\nabla\boldsymbol{u}'\right)\end{aligned} \tag{15b}$$

$$\begin{aligned}&\bar{\rho}\left(\frac{\overline{\mathrm{D}}Y_F'}{\overline{\mathrm{D}}t} + \boldsymbol{u}'\cdot\nabla\bar{Y}_F\right) + \rho'\bar{\boldsymbol{u}}\cdot\nabla\bar{Y}_F \\ &= \frac{1}{c_p}\left[\nabla\cdot\left(\lambda'\nabla\bar{Y}_F + \bar{\lambda}\nabla Y_F'\right) + (\dot{\omega}_F)'\right]\end{aligned} \tag{15c}$$

$$\begin{aligned}&\bar{\rho}\left(\frac{\overline{\mathrm{D}}T'}{\overline{\mathrm{D}}t} + \boldsymbol{u}'\cdot\nabla\bar{T}\right) + \rho'\bar{\boldsymbol{u}}\cdot\nabla\bar{T} \\ &\quad = \frac{1}{c_p}\left[\nabla\cdot\left(\lambda'\nabla\bar{T} + \bar{\lambda}\nabla T'\right) + (\dot{\omega}_T)'\right]\end{aligned} \tag{15d}$$

where $\overline{(.)}$ indicates a mean quantity and $(.)'$ a perturbed quantity. Linearized material derivative is given by

$$\frac{\overline{\mathrm{D}}(.)}{\overline{\mathrm{D}}t} = \frac{\partial(.)}{\partial t} + \bar{\boldsymbol{u}}\nabla(.) \tag{16}$$

For the combustion model, the parameters α, β and A have to be chosen. The model parameter α represents the total heat release of the flame, while β is a non-dimensional formulation of the activation temperature.

α can be calculated by $\alpha = (T_2 - T_1)/T_2$, while β is given as $\beta = \alpha T_a/T_2$ with the activation temperature T_a. Poinsot and Veynante[20] give two typical values for β, $\beta = 8$ for turbulent combustion and $\beta = 18.4$ for premixed hydrocarbon–air flames. We find that the lower beta value of 8 yields thicker flame structures which are closer to the results from OpenFOAM. The preexponential factor is $A = 2.25 \cdot 10^9$. We adjust the preexponential factor such that the flame speed of the reference flame is captured. We use the analytic expression for the flame speed Poinsot and Veynante[20]

$$s_L = \frac{1}{\beta} exp\left(-\frac{\beta}{2\alpha}\right)\left(2A\frac{\lambda_1}{\rho_1 c_p}\right)^{0.5}\left(1 + \frac{1.344 - 3\alpha}{\beta}\right) \quad (17)$$

The constants in Sutherland's viscosity model are $A_s = 1.67212 \cdot 10^{-6}$ kg/(sm$\sqrt{\text{K}}$) and $S = 170.672$ K.

Available online at www.sciencedirect.com

ScienceDirect

Proceedings of the Combustion Institute 36 (2017) 3725–3732

Proceedings of the Combustion Institute

www.elsevier.com/locate/proci

An analytical model for the impulse response of laminar premixed flames to equivalence ratio perturbations

A. Albayrak, R.S. Blumenthal, A. Ulhaq, W. Polifke*

Professur für Thermofluiddynamik, Technische Universität München, Boltzmannstr. 15, Garching D-85748, Germany

Received 2 December 2015; accepted 1 June 2016
Available online 20 June 2016

Abstract

The dynamic response of conical laminar premixed flames to fluctuations of equivalence ratio is analyzed in the time domain, making use of a level set method ("*G*-Equation"). Perturbations of equivalence ratio imposed at the flame base are convected towards the flame front, where they cause modulations of flame speed, heat of reaction and flame shape. The resulting fluctuations of heat release rate are represented in closed form in terms of respective impulse response functions. The time scales corresponding to these mechanisms are identified, their contributions to the overall flame impulse response are discussed. If the impulse response functions are Laplace transformed to the frequency domain, agreement with previous results for the flame frequency response is observed. An extension of the model that accounts for dispersion of equivalence ratio fluctuations due to molecular diffusion is proposed. The dispersive model reveals the sensitivity of the premixed flame dynamics to the distance between the flame and the fuel injector. The model results are compared against numerical simulation of a laminar premixed flame.

Keywords: Laminar premixed flame dynamics; Equivalence ratio perturbation; Impulse response; Flame frequency response; Dispersion

1. Introduction

Modern low-emission combustion processes often utilize premixed combustion with lean fuel-air mixtures. However, premixed combustion is prone to thermo-acoustic instabilities, where positive feedback between fluctuating heat release and acoustics drives self-excited oscillations. Large amplitude oscillations can cause damage to a combustor, thus it is necessary to understand the physics of lean premixed combustion dynamics and reveal key factors and interaction mechanisms responsible for instabilities.

Premixed flame dynamics is driven mainly by velocity and equivalence ratio perturbations. The corresponding interaction mechanisms have been studied extensively by means of analytical models, numerical simulations and experiments, as described by Lieuwen [1]. First analytical studies of the dynamic response of anchored premixed flames to velocity perturbation were carried out by Boyer and Quinard [2] and Fleifil et al. [3]. Schuller

* Corresponding author.
E-mail address: polifke@tfd.mw.tum.de (W. Polifke).

http://dx.doi.org/10.1016/j.proci.2016.06.002

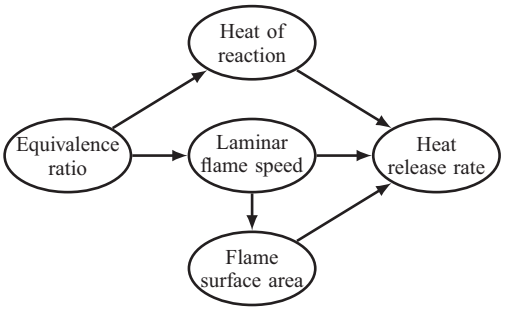

Fig. 1. Major mechanisms contributing to heat release rate oscillations [7].

et al. [4] presented a comprehensive treatment for various flame shapes, and compared analytical results against numerical and experimental data. All these studies were based on a linearized version of the so-called *G-Equation*, i.e. a kinematic equation for a propagating flame front [5]. Using the same framework, the response of laminar premixed flames to equivalence ratio perturbations was studied by Dowling and Hubbard [6] and by Lieuwen and co-authors [7–9].

The conventional way of representing the flame response to both velocity and equivalence ratio perturbations relies on the *Flame Transfer Functions* (FTF) in the frequency domain. Such a frequency domain approach is very convenient for asymptotic stability analysis, but poses a challenge for the physics-based interpretation of transient flow–flame interactions. A time domain approach, based on the *Impulse Response* (IR) function, appears more suitable for this purpose, even though fundamentally FTF and IR contain the same information. The IR of premixed flames to velocity perturbations was determined by Blumenthal et al. [10] using the linearized *G*-Equation. The time domain perspective allowed straightforward identification of characteristic time scales and gave additional insight into the pertinent flow–flame interactions. Moreover, complete correspondence with frequency domain results by Schuller et al. [4] could be established.

In the present work, the impulse response of a conical premix flame to perturbations of equivalence ratio is derived analytically. Following Lieuwen and co-workers [7–9], the dominant interaction mechanisms between fluctuations of equivalence ratio and heat release rate are considered (see Fig. 1): Firstly, perturbations in equivalence ratio modulate the heat of reaction and the laminar flame speed, which affect the heat release rate of the flame in a direct manner [11,12]. Moreover, changes in laminar flame speed disturb the kinematic balance between flow and flame, such that the flame shape and the flame surface area are also perturbed. This is an indirect, but important effect, first discussed by Lawn and Polifke [11]. Other contributions, i.e. flame stretch and curvature, gas expansion, flame confinement and anchoring, are not considered in the present analysis.

Like earlier studies [2–4,7–9], the present work uses the linearized *G*-Equation, but in the time domain. More insight into the physics of flame dynamics is expected to result from such a treatment. It will be confirmed that the overall flame dynamics can be described by the superposition of the mechanisms depicted in Fig. 1. The respective contributions to the overall flame response are determined by individual IRs and relevant time scales are identified. Furthermore, an extension of the model is proposed, which considers the effect of dispersion on the spatio-temporal distribution of equivalence ratio perturbations and on the flame dynamics.

The paper is structured as follows: A model for premixed flame dynamics based on the linearized *G*-Equation is described in the next section. Heat release rate fluctuations caused by perturbations of equivalence ratio are described in terms of impulse responses. For each of the contributions depicted in Fig. 1, the respective IR is derived and explained in Section 3. Eventually the flame transfer functions of Shreekrishna et al. [8] are recovered. In Section 4, the dispersive model is introduced. Results of a validation study against numerical simulation is presented in Section 5.

2. Modeling tools

2.1. Modeling of heat release rate fluctuations

Flame dynamics can be investigated with the relation $q(t) = \int_f \rho \Delta H s_L \, \mathrm{d}A$ for the unsteady heat release rate of a premixed flame in linearized form

$$\frac{q'(t)}{\bar{q}} = \int_f \frac{\Delta H'}{\Delta \bar{H}} \frac{\mathrm{d}A}{\bar{A}} + \int_f \frac{s'_L}{\bar{s}_L} \frac{\mathrm{d}A}{\bar{A}} + \frac{A'(t)}{\bar{A}} \,, \qquad (1)$$

where $\bar{(\,)}$ and $(\,)'$ stand for the steady and fluctuating quantities, respectively. ΔH is the heat of reaction, s_L is the laminar flame speed and A is the flame surface area. The fluctuating quantities depend on the local values of equivalence ratio ϕ. The unburnt gas density ρ is assumed to be constant. The major contributions to heat release rate fluctuations discussed above (see Fig. 1) appear explicitly on the r.h.s. of the equation.

2.2. G-Equation approach for flame shape

The flame surface motion is modeled with the *G-Equation*, i.e. a level set approach that reads

$$\frac{\partial G}{\partial t} + \vec{v} \cdot \vec{\nabla} G = s_L |\vec{\nabla} G|. \qquad (2)$$

Here $\vec{v}$ is the flow velocity and G is the level set function with the flame position at $G = 0$. The

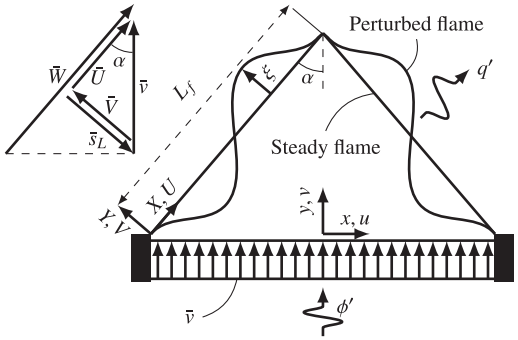

Fig. 2. Flame configuration, important velocities and laboratory $(x,\ y)$ and flame aligned $(X,\ Y)$ coordinate systems.

linearized G-Equation can be solved analytically for uniform mean velocity $\vec{v} = (0, \bar{v})$, see Fig. 2. The assumption of linearity limits any perturbations to small amplitudes in order to have an amplitude independent flame response. The flame aligned coordinate system "$(X,\ Y)$" is employed instead of the laboratory coordinate system "$(x,\ y)$", see Fig. 2. The flame surface motion is assumed to be strictly normal to the flame, mathematically $G(X, Y, t) = Y - \xi(X, t)$. Substituting the perturbation in flame surface position $\xi(X,\ t)$ in the linearized G-Equation leads to

$$\frac{\partial \xi}{\partial t} + \bar{U}\frac{\partial \xi}{\partial X} = V' - s'_L \ . \tag{3}$$

The velocities $U,\ V$ and s_L are illustrated in Fig. 2. The flame is assumed to be attached to the wall corners, i.e., $\xi(0, t) = 0$ is used as boundary condition. The analytical solution of Eq. (3) will be employed to determine the contribution of flame surface area fluctuations to the heat release rate in Section 3.3.

2.3. Impulse response (IR) for identification

A general way to quantify linear fluctuations in heat release rate q' caused by equivalence ratio perturbations ϕ' is the *impulse response* $h(\tau)$, which is defined implicitly via

$$\frac{q'(t)}{\bar{q}} = \frac{1}{\bar{\phi}}\int_0^\infty h(\tau)\phi'(y = 0, t - \tau)\,\mathrm{d}\tau \ . \tag{4}$$

Here the source of ϕ' is located at flame base $y = 0$ without loss of generality. If an impulse perturbation $\phi'(y = 0, t) = \bar{\phi}\varepsilon\delta(t)$ is imposed, where δ is the Dirac delta function and ε the relative strength of the perturbation, then correspondingly $q'(t)/\varepsilon\bar{q} = h(t)$, which is why $h(\tau)$ is called the *impulse response*. The effects that contribute to flame response – see Fig. 1 and Eq. (1) – can be investigated separately,

$$h(t) = h_{\Delta H}(t) + h_{s_L}(t) + h_A(t). \tag{5}$$

The FTF $F(\omega)$ is obtained from the IR by Laplace transformation, $F(s) = \int_0^\infty \mathrm{e}^{-st}h(t)\,\mathrm{d}t$ with $s = -i\omega$.

2.4. Transport of equivalence ratio perturbations

The convective transport of equivalence ratio perturbations may be modeled with the 1-D advection equation as

$$\frac{\partial \phi'}{\partial t} + \bar{v}\frac{\partial \phi'}{\partial y} = 0 \ . \tag{6}$$

The analytical solution for an impulse perturbation imposed at flame base $y = 0$ reads

$$\phi'(x, y, t) = \bar{\phi}\varepsilon\delta\left(t - \frac{y}{\bar{v}}\right) = \bar{\phi}\varepsilon\delta\left(t - \frac{X}{\bar{W}}\right) \ . \tag{7}$$

Physically interpreted, a sudden change in equivalence ratio at the flame base convects in $y-$direction towards the flame tip with the flow velocity $\bar{v}$. Equation (7) also shows how this effect may be represented in the flame-aligned coordinate system.

3. Contributions to the flame impulse response

3.1. Fluctuations of heat of reaction

The first term on the right hand side of Eq. (1) stands for the contribution of heat of reaction fluctuations to the heat release rate. The fluctuation in heat of reaction $\Delta H'$ caused by the equivalence ratio perturbations ϕ' is approximated by a relation $\Delta H = f(\phi)$ from empirical data (valid for CH_4 [7]). First order Taylor series expansion is employed for fluctuating quantities, $\Delta H' = \mathrm{d}\Delta H/\mathrm{d}\phi|_{\phi=\bar{\phi}}\phi'$.

By integrating $\Delta H'$ over the flame surface, the IR contribution is calculated as

$$\begin{aligned} h_{\Delta H}(t) &= \frac{1}{\varepsilon}\int_f \frac{\Delta H'}{\Delta \bar{H}}\frac{\mathrm{d}A}{\bar{A}} \\ &= \frac{1}{\varepsilon}\left.\frac{\mathrm{d}\Delta H}{\mathrm{d}\phi}\right|_{\phi=\bar{\phi}}\frac{1}{\Delta \bar{H}\bar{A}}\int_f \phi'\,\mathrm{d}A \ , \end{aligned} \tag{8}$$

where $\bar{A} = \pi L_f^2 \sin\alpha$ is the steady flame surface area and $\mathrm{d}A = 2\pi(L_f - X)\sin\alpha \mathrm{d}X$ is the steady infinitesimal flame surface area for a conical flame. By substituting $\phi' = \bar{\phi}\varepsilon\delta\left(t - X/\bar{W}\right)$ as defined in Section 2.4, the IR is obtained in closed form

$$h_{\Delta H}(t) = \frac{2S_{\Delta H}}{\tau_c^2}\{R(t - \tau_c) - R(t) + \tau_c H(t)\}. \tag{9}$$

where $H(t)$ is the Heaviside function and $R(t)$ is the Ramp function. $S_{\Delta H} = \left(\bar{\phi}/\Delta\bar{H}\right)\mathrm{d}\Delta H/\mathrm{d}\phi|_{\phi=\bar{\phi}}$ is the sensitivity of the heat of reaction to the equivalence ratio. $\tau_c = L_f/\bar{W}$ is a convective time scale, which is defined as the time span for the perturbation to travel from the base of the flame to its tip.

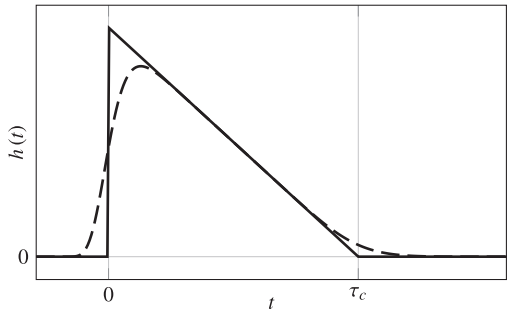

Fig. 3. Contribution of fluctuations in heat of reaction or laminar flame speed to the IR. Models without (——) and with dispersion (– –).

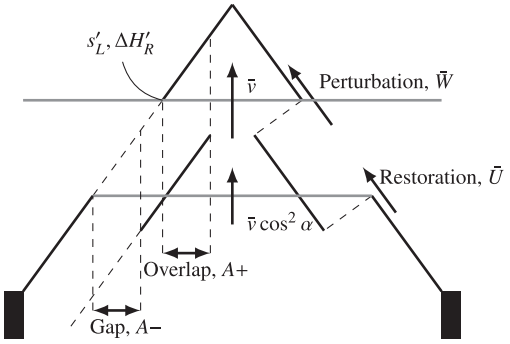

Fig. 4. Intermediate flame shape with relevant velocities for convection of perturbation and restoration process. Visualization of area gap and overlap due to the change in laminar flame speed.

The IR according to Eq. (9) is plotted in Fig. 3 with the solid line.

Laplace Transform as defined in Section 2.3 recovers exactly the analytical expression for the flame transfer function obtained by Shreekrishna et al. [8, Eq. (25)].

For the lean premixed flame, a positive impulse perturbation in the equivalence ratio increases the heat of reaction on the flame surface element located at the instantaneous position of the perturbation. The increase in heat of reaction also increases the heat release rate (see Eq. (1)). In Fig. 4 a flame perturbed by a δ-pulse as defined in Eq. (7) is shown. The upper gray line ("Perturbation, $\bar{W}$") indicates the flame surface element, whose heat of reaction is changed. The incoming perturbation initially acts on the flame at the base, which has the largest radius. As the perturbation is convected towards the flame tip, the resulting perturbation in heat release rate decreases, because the radius of the flame decreases. This fact explains the trend shown in Fig. 3, that the IR contribution is highest at the beginning and decreases until the convective time scale τ_c, when the perturbation reaches the flame tip, which has zero radius.

For rich mixtures, additional fuel barely changes the heat of reaction, which implies that the sensitivity $S_{\Delta H}$ and thus also the corresponding IR are very small.

3.2. Fluctuations of laminar flame speed

The second term on the right hand side of Eq. (1) stands for the contribution of laminar flame speed fluctuations to the heat release rate. The same approach as described in Section 3.1 is employed also for laminar flame speed contribution. The only difference is that $S_{\Delta H}$ is replaced with the sensitivity of laminar flame speed to the equivalence ratio, $S_{s_L} = \left(\bar{\phi}/\bar{s}_L\right) \mathrm{d}s_L/\mathrm{d}\phi|_{\phi=\bar{\phi}}$. The shape of the corresponding IR is shown in Fig. 3 and can be explained with similar arguments as in Section 3.1. Again, Laplace Transform recovers exactly the FTF of Shreekrishna et al. [8, Eq. (24)].

For lean premixed flames the sensitivity S_{s_L} is positive and therefore the IR is positive. For rich mixtures, additional fuel leads to a decrease in the laminar flame speed and the IR is reversed.

3.3. Fluctuations of flame surface area

The third term on the right hand side of Eq. (1) stands for the contribution of flame surface area fluctuations to the IR of the heat release rate. This mechanism was already discussed by Blumenthal et al. [10], albeit only for the perturbations in velocity. Relevant time scales of restoration τ_r and convection τ_c were revealed, their impact on flame dynamics was discussed. In the present study, a similar approach is developed for the effects of equivalence ratio perturbations on flame shape and heat release rate. The similarity comes from the fact that the perturbed flame position ξ depends on V' and s'_L, as described in the right hand side of Eq. (3). The similarity is attributed to Eq. (3), where V' and s'_L act as source terms for the perturbed flame position ξ.

The first step is to compute ξ. Equation (3) for $\xi(X, t)$ can be formulated as an integral equation

$$\xi(X,t) = -\frac{1}{\bar{U}} \int_0^X s'_L\left(X', t - \frac{X - X'}{\bar{U}}\right) \mathrm{d}X' \,, \tag{10}$$

where laminar flame speed fluctuations caused by ϕ' are considered solely ($V' = 0$). The IR contribution is calculated as

$$h_A(t) = \frac{1}{\varepsilon} \frac{A'(t)}{\bar{A}} = \frac{2}{\varepsilon L_f^2 \tan\alpha} \int_0^{L_f} \xi(X,t)\, \mathrm{d}X \,. \tag{11}$$

In order to calculate the closed form IR, $\phi' = \bar{\phi}\varepsilon\delta\left(t - X/\bar{W}\right)$ is substituted in Eq. (10) and ξ is

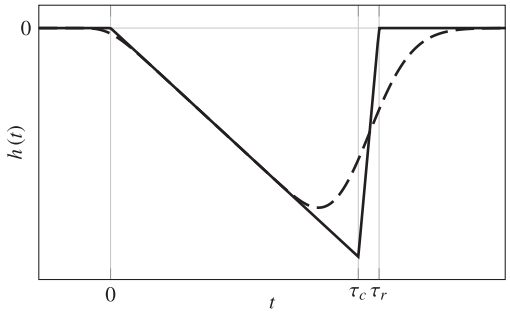

Fig. 5. Contribution of fluctuations of flame surface area to IR. Model without (——) and with dispersion (– –).

expressed as

$$\xi(X,t) = -\left.\frac{\mathrm{d}s_L}{\mathrm{d}\phi}\right|_{\phi=\bar{\phi}} \frac{\bar{\phi}\varepsilon\tau_r}{\tau_r-\tau_c}\left[H\left(t-\frac{X}{\bar{W}}\right) - H\left(t-\frac{X}{\bar{U}}\right)\right], \tag{12}$$

where $\tau_r = L_f/\bar{U}$ is the restorative time scale, which is defined as the time span for the hypothetical restoration line to travel from the base of the flame to its tip. ξ is illustrated with an intermediate flame shape perturbed with an impulse in Fig. 4.

The upper gray line ("Perturbation, $\bar{W}$") indicates the convection of impulsive perturbation and $\bar{W} = \bar{v}/\cos(\alpha)$ is the projection on $X-$direction. Since the mixture is assumed lean and the equivalence ratio perturbation is positive, the laminar flame speed perturbation is also positive. An increase in laminar flame speed overcomes the flow velocity normal to the flame surface and the flame propagates towards the base.

Starting from the anchoring point, where $\xi(0,t) = 0$, the restoration mechanism [10] re-establishes the original, unperturbed flame shape after the perturbation of equivalence ratio has passed. The lower gray line ("Restoration, $\bar{U}$") in Fig. 4 indicates up to which position the restoration process has progressed. This line travels with the speed $U = \bar{v}\cos(\alpha)$ in $X-$direction. The restoration line is upstream of the perturbation line, because of slower propagation speed.

By substituting ξ described in Eq. (12) into Eq. (11), the closed form IR is obtained

$$h_A(t) = -\frac{2S_{s_L}}{\tau_c(\tau_r-\tau_c)}\left[\frac{\tau_c}{\tau_r}\{R(t-\tau_r)-R(t)\} - \{R(t-\tau_c)-R(t)\}\right] \tag{13}$$

which is plotted in Fig. 5 with the solid line. Again the FTF given by Shreekrishna et al. [8, Eq. (26)] is exactly recovered by Laplace Transform.

The shape of the IR may be explained as follows: The perturbation ϕ' causes flame propagation towards the base and creates additional flame surface area indicated as "Overlap, A^+" in Fig. 4. At the same time, the restoration mechanism brings the flame to its old position and causes a deficit in flame surface area indicated as "Gap, A^-" in Fig. 4. Since the restoration process is slower, it acts at a position where the flame radius is larger than the one for the perturbation, thus the perturbed area is less than the steady area (negative IR in Fig. 5). As long as both processes act on the flame together, the deficit of flame surface area continuously increases. At late times $t > \tau_c$, when the perturbation has passed the flame, only the restorative mechanism acts to recover the original flame shape. The flame surface area deficit vanishes once the restoration line reaches the flame tip, which corresponds to the restorative time scale τ_r.

This section concludes with a comment on the study of Cho and Lieuwen [7], who derived time domain representations of flame dynamics by inverse Laplace transformation of frequency domain results. However, the IR was not recovered, because a generic form of perturbations was considered instead of an impulse perturbation. A full time domain analysis of the flame response to a generic perturbation is not straightforward and was indeed not attempted by Cho and Lieuwen [7]. Instead, their results are valid only in the low-frequency, quasi-steady limit.

4. Extended model with dispersion

In typical technical premixed combustion systems, the fuel is injected from a considerable distance upstream of the flame. This distance is important for the equivalence ratio perturbations because of dispersion due to molecular diffusion for a laminar flame. Generalization to turbulent dispersion is straightforward, but not discussed further here (refer to Polifke et al. [13], Lawn and Polifke [11], Schuermans et al. [12] and Bobusch et al. [14]). As the injection point moves further upstream, a wider Gaussian distribution instead of an impulse (Dirac function) arrives at the flame base and thus the impact on flame dynamics becomes weaker.

The model described in Section 2 and also previous models [7–9] employ an advection equation as described in Eq. (6). The impact of the species diffusion can be accounted by considering 1-D advection-diffusion equation with impulse perturbation at flame base $y = 0$, which reads

$$\frac{\partial\phi'}{\partial t} + \bar{v}\frac{\partial\phi'}{\partial y} = D\frac{\partial^2\phi'}{\partial y^2}\,, \tag{14}$$

where D is the averaged diffusion coefficient. The analytical solution reads

$$\phi'(x,y,t) = \bar{\phi}\varepsilon\sqrt{\frac{1}{\pi\tau_d t}}\exp\left[-\frac{1}{\tau_d t}\left(t-\frac{X}{\bar{W}}\right)^2\right], \tag{15}$$

where $\tau_d = 4D/\bar{v}^2$ is the diffusive time scale, which describes the strength of the diffusion. The solution is expressed in the flame aligned coordinate system.

The formalism developed in Section 3 can also be applied to the extended model. For heat of reaction contribution, Eq. (8) is integrated with the diffusive perturbation equation (15) instead of the impulse equation (7) (same for laminar flame speed contribution). The resulting IR contribution reads

$$h_{\Delta H}(t) = \frac{S_{\Delta H}}{\tau_c^2}\left\{\Re(t-\tau_c) - \Re(t) + \tau_c \mathrm{erf}\left(\frac{t}{\sqrt{\tau_d t}}\right)\right\}, \tag{16}$$

where $\Re(t,\tau)$ is the smoothed Ramp function defined as

$$\Re(t-\tau) = \sqrt{\frac{\tau_d t}{\pi}}\exp\left(-\frac{(t-\tau)^2}{\tau_d t}\right) + (t-\tau)\mathrm{erf}\left(\frac{t-\tau}{\sqrt{\tau_d t}}\right). \tag{17}$$

The contribution of laminar flame speed fluctuations is the same as Eq. (16), but $S_{\Delta H}$ is replaced with S_{s_L}.

For flame surface area contribution, the flame surface deviation ξ is determined by integrating equation (10) again with the diffusive perturbation. The contribution is then computed by integrating the flame surface deviation Eq. (11) as

$$h_A(t) = -\frac{S_{s_L}}{\tau_c(\tau_r-\tau_c)}\left[\frac{\tau_c}{\tau_r}\{\Re(t-\tau_r)-\Re(t)\} - \{\Re(t-\tau_c)-\Re(t)\}\right]. \tag{18}$$

The resulting IRs are plotted in Figs. 3 and 5 with dashed lines, for heat of reaction (same for laminar flame speed) and flame surface area, respectively.

The model can be extended for the cases, where the perturbation is imposed upstream of the flame base, say $y = -y_0$. The additional time lag for the perturbation to travel till the flame base $\tau_0 = y_0/\bar{v}$ can be accounted by change of variable of $t = t^* - \tau_0$ in Eqs. (15)–(18).

5. Validation against numerical simulation

A numerical simulation of a 2D axisymmetric conical flame is performed to validate the analytical model. Length and radius of the upstream flow duct are both 1 mm, the downstream radius of the computational domain is 6 mm in order to prevent confinement effects. A uniform mesh is constructed with a cell size of 0.02 mm. Slip and adiabatic wall boundary conditions are imposed to correspond with the analytical framework. A lean mixture of CH_4 and air ($\bar{\phi} = 0.8$) is used, the inflow velocity is $\bar{v} = 1$ m/s (Reynolds number 130) at a temperature of 293 K. A 2-step reduced

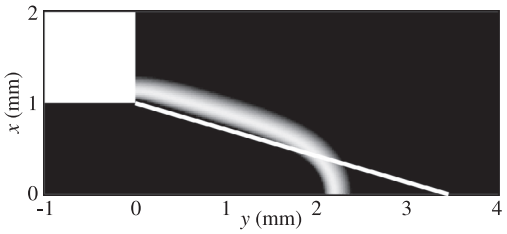

Fig. 6. Flame shapes: G-Equation model vs. numerical simulation with 2-step chemistry.

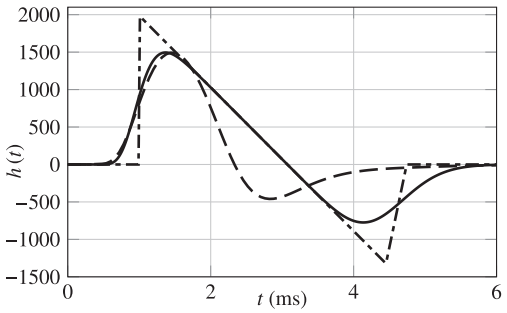

Fig. 7. Impulse response functions of conical laminar premixed flame. Analytical model without dispersion (– - –), with dispersion (——) and CFD results (— —).

chemistry is employed [15] in rhoReactingFoam (OpenFOAM solver), which is modified to assume Prandtl number of 0.7. The averaged molecular diffusivity was set to $D = 0.22 \times 10^{-4}\mathrm{m}^2/\mathrm{s}$, appropriate for CH_4 in air [16].

Figure 6 compares the distribution of steady heat release rate from CFD against the analytical *G*-Equation flame. Close to the tip, curvature effects – which are not considered in *G*-Equation used – result in a comparatively shorter flame length of the CFD model.

Broadband equivalence ratio perturbations with an amplitude of $\varepsilon = \phi'/\bar{\phi} = 0.05$ are imposed at the inlet. The corresponding IR is determined via system identification (for details see [17]) and compared against the analytical model in Fig. 7. The latter includes all three contributions discussed above, see Fig. 1.

Including dispersion in the analytical model gives a "smeared out" response, in qualitative agreement with CFD. More than that, Fig. 7 shows very good quantitative agreement between CFD and the dispersive model for the early period $t <$ 2 ms.

At later times, the impulse response is negative before it decays to zero. This important feature, which is responsible for the excess gain of the FTF (see below) is reproduced qualitatively by both models based on the *G*-Equation. Nevertheless, it is apparent that at later times $t > 2$ ms quantitative

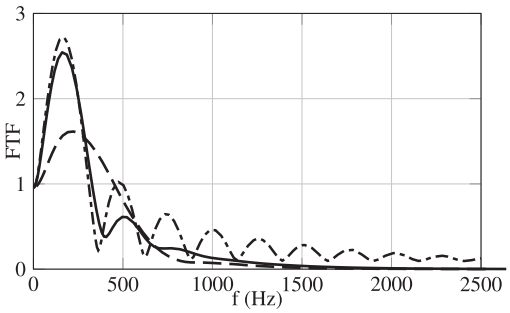

Fig. 8. Gain of FTF. Analytical model without dispersion (– - –), with dispersion (——) and CFD results (— —).

agreement with CFD deteriorates. This is due to the over-predicted flame length of the G-Equation model, resulting from the neglect of curvature effects. Note that the overall duration of the IR is related to the restorative time scale $\tau_r = L_f/\bar{U}$. Since the flame length L_f is over-predicted, the resulting IR is also more pronounced at late times.

Figure 8 compares the gain of the FTFs determined with the analytical model and the CFD simulation, respectively. Important qualitative features are reproduced by both analytical model formulations: the overall low pass filter behavior is observed, initial overshoot in gain is present, the low frequency limit (see Polifke and Lawn [18]) is correctly captured as unity.

The dash-dotted line indicates the FTF from the analytical model without dispersion. The model shows oscillatory behavior in the high frequency range, which is eliminated by dispersion (shown with solid line).

Both analytical and numerical results exhibit excess gain $|FTF| > 1$ at frequencies around 200 Hz. Excess gain results from constructive superposition of the positive and negative parts of the IR, as discussed by Huber and Polifke [19] and Blumenthal et al. [10]. The analysis in Section 3 has shown that the positive part of the IR results from fluctuations in heat of reaction and flame speed, while the negative part is due to the modulation of flame surface area. In the low frequency limit there is destructive superposition of these effects, which becomes constructive at intermediate frequencies, resulting in excess gain. Indeed, earlier models that did not take into account changes in flame surface area do not exhibit excess gain [13,20].

The intermediate frequency $f_{\max}$ where the gain attains its maximum can be roughly estimated as

$$f_{\max} \approx \frac{\pi}{2(t_{\max} - t_{\min})}, \tag{19}$$

where $t_{\max}$ and $t_{\min}$ are the times where the IR reaches maximal/minimal values. For the analytical model with dispersion, one estimates $f_{\max} \approx 200$ Hz, which agrees with the gain of the FTF shown in Fig. 8. For the CFD results, the negative part of the IR appears earlier and is less pronounced (see Fig. 6), thus excess gain occurs at higher frequencies and with reduced magnitude, as seen in Fig. 8.

6. Conclusion

The response of laminar premixed flame to equivalence ratio perturbations was studied analytically by determining the IR for heat release rate. In the framework of the G-Equation contributions of heat of reaction, laminar flame speed and flame surface area were taken into consideration. Two relevant time scales were identified, i.e. a convective time scale τ_c and a restorative time scale τ_r. The transport of equivalence ratio perturbations is related to τ_c, while the propagation of flame shape perturbations along the flame is related to τ_r. The contributions of heat of reaction and laminar flame speed are governed only by τ_c, since the convective perturbations of equivalence ratio causes local changes at the flame surface. The contribution of flame surface area is controlled by both τ_c and τ_r due to the restoration mechanism. Complete agreement with flame transfer functions calculated by Shreekrishna et al. [8] was established by Laplace transformation of IRs.

An extension to the model was proposed in order to account for the dispersion due to molecular diffusion. The dispersive model adds one more time scale τ_d regarding the strength of the dispersion. As the location of the perturbation moves further away from the flame, its impact on the flame dynamics becomes weaker [13].

Analytical models were compared against numerical simulation by examining the respective IRs and FTFs. Quantitative agreement was not achieved, since the analytical G-Equation model used in this study neglects curvature effects and thus over-predicts the flame length. Nevertheless, very satisfactory qualitative agreement with respect to the shape of the IR and the relevant time scales was observed. Overall, the model with dispersion showed significantly better agreement than the model without dispersion.

The analysis in the paper shows that excess gain in the flame response to equivalence ratio fluctuations results from constructive superposition of the effects of fluctuations in heat of reaction and flame speed on the one hand, and the effects of modulation of flame shape on the other.

Acknowledgments

The presented work is part of the Marie Curie Initial Training Network *Thermo-acoustic and aero-acoustic nonlinearities in green combustors with orifice structures* (TANGO). We gratefully acknowledge the financial support from the

European Commission under call FP7-PEOPLE-ITN-2012. Financial support for A. Ulhaq was provided by higher education commission (HEC) of Pakistan. Financial support for R. S. Blumenthal was provided by Technische Universität Müchen, Institute for Advanced Study, funded by the German Excellence Initiative, and German Research Foundation DFG, project PO 710/12-1.

References

[1] T.C. Lieuwen, *Unsteady Combustor Physics*, Cambridge University Press, 2012.
[2] L. Boyer, J. Quinard, *Combust. Flame* 82 (1990) 51–65.
[3] A. Fleifil, A.M. Annaswamy, Z.A. Ghoneim, A.F. Ghoniem, *Combust. Flame* 106 (1996) 487–510.
[4] T. Schuller, D. Durox, S. Candel, *Combust. Flame* 134 (1) (2003) 21–34.
[5] A.R. Kerstein, W.T. Ashurst, F.A. Williams, *Phys. Rev. A* 37 (1988) 2728.
[6] A. Dowling, S. Hubbard, *Proc. Inst. Mech. Eng., Part A J. Power Energy* 214 (4) (2000) 317–332.
[7] J.H. Cho, T. Lieuwen, *Combust. Flame* 140 (1) (2005) 116–129.
[8] Shreekrishna, S. Hemchandra, T. Lieuwen, *Combust. Theor. Model.* 14 (5) (2010) 681–714.
[9] S. Hemchandra, in: ASME Turbo Expo: Turbine Technical Conference and Exposition, GT2011-45590, American Society of Mechanical Engineers, 2011, pp. 567–578.
[10] R.S. Blumenthal, P. Subramanian, R. Sujith, W. Polifke, *Combust. Flame* 160 (7) (2013) 1215–1224.
[11] C.J. Lawn, W. Polifke, *Combust. Sci. Technol.* 176 (2004) 1359–1390.
[12] B. Schuermans, V. Bellucci, F. Guethe, F. Meili, P. Flohr, O. Paschereit, in: International Gas Turbine and Aeroengine Congress & Exposition, GT2004-53831, 2004.
[13] W. Polifke, J. Kopitz, A. Serbanovic, in: 7th AIAA/CEAS Aeroacoustics Conference, AIAA 2001–2104, 2001. Maastricht, The Netherlands
[14] B.C. Bobusch, B. Ćosić, J.P. Moeck, C. Oliver Paschereit, in: Journal of Engineering for Gas Turbines and Power, vol. 136, 2013, p. 021506, doi:10.1115/1.4025375.
[15] J. Bibrzycki, T. Poinsot, A. Zajdel, *Archivum Combustionis,* A. Teodorczyk, Varsovie, Pologne 30 (2010) 287–296.
[16] M. Cowie, H. Watts, *Can. J. Chem.* 49 (1) (1971) 74–77.
[17] W. Polifke, *Ann. Nuclear Energy* 67C (2014) 109–128, doi:10.1016/j.anucene.2013.10.037.
[18] W. Polifke, C.J. Lawn, *Combust. Flame* 151 (3) (2007) 437–451, doi:10.1016/j.combustflame.2007.07.005.
[19] A. Huber, W. Polifke, *Int. J. Spray Combust. Dyn.* 1 (2) (2009) 199–228.
[20] J.F. v Kampen, J.B.W. Kok, T.H. van der Meer, in: 12th International Congress on Sound and Vibration (ICSV12), IIAV, Lisbon, Portugal, July 11-14 2005.

Special Issue - Advective disturbances in combustor thermoacoustics

International journal of spray and combustion dynamics

International Journal of Spray and Combustion Dynamics
0(0) 1–8

DOI: 10.1177/1756827717740776
journals.sagepub.com/home/scd
SAGE

An analytical model based on the *G*-equation for the response of technically premixed flames to perturbations of equivalence ratio

Alp Albayrak and Wolfgang Polifke

Abstract

A model for the response of technically premixed flames to equivalence ratio perturbations is proposed. The formulation, which is an extension of an analytical flame tracking model based on the linearized *G*-equation, considers the flame impulse response to a local, impulsive, infinitesimal perturbation that is transported by convection from the flame base towards the flame surface. It is shown that the contributions of laminar flame speed and heat of reaction to the impulse response exhibit a local behavior, i.e. the flame responds at the moment when and at the location where the equivalence ratio perturbation reaches the flame surface. The time lag of this process is related to a convective time scale, which corresponds to the convective transport of fuel from the base of the flame to the flame surface. On the contrary, the flame surface area contribution exhibits a non-local behavior: albeit fluctuations of the flame shape are generated locally due to a distortion of the kinematic balance between flame speed and the flow velocity, the resulting wrinkles in flame shape are then transported by convection towards the flame tip with the restorative time scale. The impact of radial non-uniformity in equivalence ratio perturbations on the flame impulse response is demonstrated by comparing the impulse responses for uniform and parabolic radial profiles. Considerable deviation in the phase of the flame transfer function, which is important for thermo-acoustic stability, is observed.

Keywords

Equivalence ratio perturbation, flame dynamics, flame transfer function, impulse response, technically premixed flames

Date received: 11 June 2017; accepted: 11 October 2017

1. Introduction

Lean fuel–air mixtures allow low-emission combustion processes in a variety of industrial applications. However, operating under such conditions increases the chance of thermo-acoustic instabilities. In order to analyze, predict and control instabilities that result from flow–flame–acoustic interactions, the dynamic response of flames to perturbations is an active research topic. Premixed flames are sensitive to perturbations of upstream velocity as well as equivalence ratio.[1,2] The present study focuses on the latter response mechanism.

The so-called *G*-equation—a level set equation that can be used to describe flame front kinematics[3]—has been used in a variety of studies on the response of a premixed flame to velocity perturbations.[4–6] To the authors' knowledge, Dowling and Hubbard[7] were the first to propose a model based on the *G*-equation for the response to equivalence ratio perturbation. In the framework of that model, Lieuwen and co-authors[8,9] identified three major contributions to perturbations of flame heat release as heat of reaction, laminar flame speed, and flame surface area; and provided an analytical expression for the flame transfer function (FTF) by solving the linearized *G*-equation in the frequency domain. An equivalent time-domain formulation, which yields the flame impulse response (IR)

Faculty of Mechanical Engineering, Technical University of Munich, Garching, Germany

Corresponding author:
Alp Albayrak, Thermo-Fluid Dynamics Group, Technical University of Munich, Boltzmannstr. 15, D-85748 Garching, Germany.
Email: albayrak@tfd.mw.tum.de

rather than the frequency response, was proposed by Albayrak et al.[10] This approach explicitly reveals two global time scales of the flame response, related to the propagation of the perturbation along the flame surface and the restoration of flame shape. These time scales were identified previously in the flame response to velocity fluctuations, as explained in detail by Blumenthal et al.[11]

All the models cited in the previous paragraph assume perturbations of equivalence ratio that are uniform across the mixing duct. This is a strong assumption, which will in general not be satisfied in practical applications with so-called technical premixed flames,[a] where fuel–air mixing is not perfect, such that mean as well as fluctuations of equivalence ratio will exhibit some non-uniformity. The present study proposes an extended, time-domain-based analysis of the effect of perturbations of equivalence ratio on flame heat release rate, which relaxes this assumption. In particular, the flame IR to a local, impulsive, infinitesimal perturbation of fuel concentration is derived analytically. The approach allows to determine the flame response to any kind of equivalence ratio perturbation profile as a convolution over the local perturbations. Moreover, the infinitesimal perturbation gives insight to the flame response mechanisms: the direct contributions, i.e. the heat of reaction and laminar flame speed, are local processes with a convective time delay, whereas the flame surface area contribution exhibits a convective nature, which is triggered locally.

In the next section the derivation of the local IR is given for a laminar conical Bunsen flame. The IR that corresponds to an uniform perturbation profile[10] is recovered, which validates the approach. Then, several perturbation profiles are investigated. It is shown that the perturbation profile has an impact on the phase of the FTF.

2. Model

The flame IR model is derived for a laminar, axisymmetric, conical flame (see Figure 1), which has been investigated repeatedly with analytical approaches.[8–10] It is possible to formulate the model for other flame shapes, e.g. V- and M-shaped flames, however this is not explicated in this paper. The flame is subjected to an impulsive local equivalence ratio perturbation $\phi'(t,z,r)$ around infinitesimal vicinity of the radius a. This is illustrated in Figure 1 with a blue circle. This reads mathematically

$$\phi'_a(t,0,r) = \bar{\phi}\delta(r-a)\delta(t) \tag{1}$$

where $\delta(t)$ is the Dirac delta function. Without essential loss of generality, the axial position of the perturbation

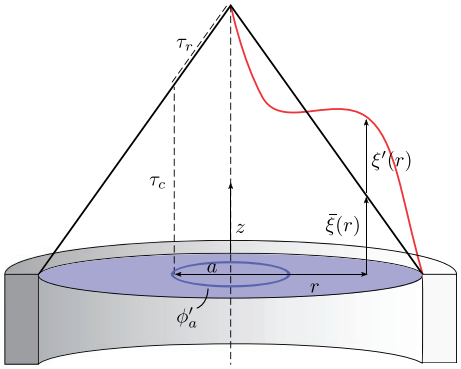

Figure 1. Illustration of the flame configuration. The mean and perturbed flame front are shown by black and red lines, respectively. Blue surface indicates the mean uniform equivalence ratio. The circle with radius a indicates infinitesimal hollow equivalence ratio perturbation. τ_c and τ_r indicate local time scales for propagation of the perturbation and restoration, respectively.

is assumed to be located in the flame base $z=0$. The corresponding IR in heat release rate $h_a(t)$ is defined implicitly by the relation

$$\frac{q'_a(t)}{\bar{q}} = \int_{-\infty}^{\infty} h_a(t-\tau)\frac{\phi'_a(t,0,r)}{\bar{\phi}}\,\mathrm{d}\tau \tag{2}$$

where q is the global heat release rate integrated over the whole flame.

2.1 Governing equations

To pursue analytical expressions the flow velocities are assumed to be uniform. The flame front kinematics is described by the level set method G-equation

$$\frac{\partial G}{\partial t} + \boldsymbol{u}\cdot\nabla G = s_L|\nabla G| \tag{3}$$

where s_L stands for the laminar flame speed.

The global heat release rate can be computed as

$$q = \int_f \rho s_L \Delta H \mathrm{d}A \tag{4}$$

where ρ is density, ΔH is heat of reaction, and A is the flame surface area. The integral interval denoted by subscript "f" indicates that the integral is evaluated over the flame surface area. The flame surface area reads

$$A = \int_0^R 2\pi r\sqrt{1+\left(\frac{\partial \xi}{\partial r}\right)^2}\,\mathrm{d}r \tag{5}$$

The transport of mixture inhomogeneities can be modeled by the advection equation for the equivalence ratio. This mathematically reads

$$\frac{\partial \phi}{\partial t} + \boldsymbol{u} \cdot \nabla \phi = 0 \tag{6}$$

2.2 Modeled equations

Assuming small amplitude fluctuations, all equations described above are linearized. $\bar{(\cdot)}$ and $(\cdot)'$ indicate mean and fluctuating quantities, respectively. No velocity fluctuations are allowed, $\boldsymbol{u}' = 0$. It is assumed that the flame is surjective, i.e. $G(t, z, r) = z - \xi(t, r)$. The linearized ξ-equation reads

$$\frac{\partial \xi'}{\partial t} + c_r \frac{\partial \xi'}{\partial r} = -s_L' \sqrt{\left(\frac{\partial \bar{\xi}}{\partial r}\right)^2 + 1} \tag{7}$$

where c_r is the propagation speed in the radial direction of the flame restoration process (see Blumenthal et al.[11])

$$c_r = u_r + \frac{\bar{s}_L \dfrac{\partial \bar{\xi}}{\partial r}}{\sqrt{\left(\dfrac{\partial \bar{\xi}}{\partial r}\right)^2 + 1}} \tag{8}$$

The normalized and linearized heat release rate fluctuations $q'/\bar{q}$ read

$$\frac{q'(t)}{\bar{q}} = \int_f \frac{\Delta H'}{\Delta \bar{H}} \frac{\mathrm{d}A}{\bar{A}} + \int_f \frac{s_L'}{\bar{s}_L} \frac{\mathrm{d}A}{\bar{A}} + \frac{A'}{\bar{A}} \tag{9}$$

where the density perturbations ρ' due to the equivalence ratio perturbations are assumed to be negligible. The impulsive perturbation simplifies the convolution integral in equation (2) and the IR can be explicitly defined as

$$h_a(t) \equiv \frac{q_a'(t)}{\bar{q}} = h_{\Delta H} + h_{s_L} + h_A \tag{10}$$

where three major contributions according to equation (9) are identified as heat of reaction $h_{\Delta H}$, laminar flame speed h_{s_L} and flame surface area h_A.

To calculate $h_{\Delta H}$ and h_{s_L} the fluctuating quantities, i.e. $\Delta H'$ and s_L', should be modeled. This is done by first-order Taylor series expansion

$$\Delta H' = S_{\Delta H} \frac{\Delta \bar{H}}{\bar{\phi}} \phi' \tag{11a}$$

$$s_L' = S_{s_L} \frac{\bar{s}_L}{\bar{\phi}} \phi' \tag{11b}$$

where $S_{\Delta H}$ and S_{s_L} are defined as the respective sensitivities of the heat of reaction and the laminar flame speed to change in equivalence ratio

$$S_{\Delta H} \equiv \left.\frac{\mathrm{d}\Delta H}{\mathrm{d}\phi}\right|_{\phi=\bar{\phi}} \frac{\bar{\phi}}{\Delta \bar{H}} \tag{12a}$$

$$S_{s_L} \equiv \left.\frac{\mathrm{d}s_L}{\mathrm{d}\phi}\right|_{\phi=\bar{\phi}} \frac{\bar{\phi}}{\bar{s}_L} \tag{12b}$$

Following Abu-Off and Cant,[12] for a lean premixed methane air flame, the heat of reaction, and laminar flame speed are expressed as a function of equivalence ratio

$$s_L = A \phi^B \mathrm{e}^{-C(\phi - D)^2} \tag{13}$$

$$\Delta H = \frac{2.9125 \cdot 10^6 \min(1, \phi)}{1 + 0.05825\phi} \tag{14}$$

where $A = 0.6079$, $B = -2.554$, $C = 7.31$, and $D = 1.23$. The flame surface area contribution h_A is calculated by the linearized flame surface area

$$\frac{A'}{\bar{A}} = \frac{\displaystyle\int_0^R 2\pi r \frac{\dfrac{\partial \bar{\xi}}{\partial r}\dfrac{\partial \xi'}{\partial r}}{\sqrt{\left(\dfrac{\partial \bar{\xi}}{\partial r}\right)^2 + 1}} \mathrm{d}r}{\displaystyle\int_0^R 2\pi r \sqrt{1 + \left(\frac{\partial \bar{\xi}}{\partial r}\right)^2} \mathrm{d}r} \tag{15}$$

The equivalence ratio perturbation $\phi'(t, z, r)$ is modeled by linearized advection equation

$$\frac{\partial \phi'}{\partial t} + u_z \frac{\partial \phi'}{\partial z} = 0 \tag{16}$$

3. Response of a conical flame

For a conical flame, the steady flame shape is expressed as

$$\bar{\xi}(r) = (R - r) \sqrt{\left(\frac{u_z}{\bar{s}_L}\right)^2 - 1} \tag{17}$$

and the flame restoration speed simplifies to

$$c_r = -\bar{s}_L \sqrt{1 - \left(\frac{\bar{s}_L}{u_z}\right)^2} \tag{18}$$

The solution of the ϕ' transport equation (16) with the boundary condition (1) reads

$$\phi'_a(t,z,r) = \bar{\phi}\delta(r-a)\delta\left(t-\frac{z}{u_z}\right) \tag{19}$$

Using equations (17), (18), and (19), the contributions to the IR can be expressed in closed forms. The following subsections provide the derivations for the heat of reaction and flame surface area contributions. The contribution of the laminar flame speed is analogous to that of the heat of reaction and therefore not discussed explicitly. Note that the derivations are valid for any equivalence ratio. For convenience, this paper presents only the results for lean flames with $\phi < 1$ and $S_{\Delta H} > 0$.

3.1 Heat of reaction contribution

The flame IR contribution of the heat of reaction is calculated by substituting the perturbation profile defined in equation (19) into equation (10)

$$h_{\Delta H}(a,t) = 2S_{\Delta H}\frac{a}{R^2}\delta(t-\tau_c) \tag{20}$$

where τ_c is the time scale related to the propagation of the equivalence ratio perturbation from the base to the flame surface which reads

$$\tau_c(a) = \frac{\bar{\xi}(a)}{u_z} \tag{21}$$

In Figure 1, the time scale τ_c is indicated as the dashed line, on which the equivalence ratio perturbation propagates. The IR is plotted in the left column of Figure 2 for five perturbation locations, i.e. $a = R \times [0, 0.25, 0.5, 0.75, 1]$. The IR is a local process. A positive impulsive response in heat release is observed at the instant when the perturbation reaches the flame surface. For $a = R$, the delay in the response is $\tau_c = 0$, since the perturbation acts immediately on the flame surface. The delay in the response increases as the location of the perturbation gets closer to the center. At the same time, the strength of the IR decreases. This is explained by the perimeter of the flame, which decreases with the radius. For the perturbation close to the center, the perturbation acts on a smaller perimeter and generates a weaker modulation of the overall heat release rate.

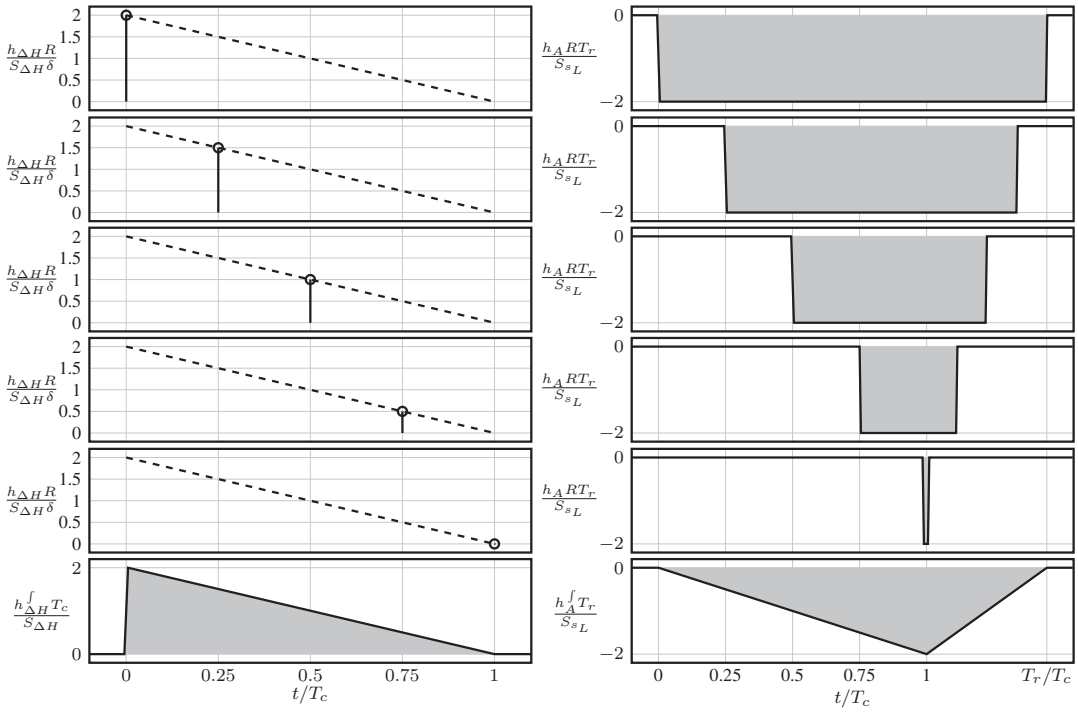

Figure 2. Heat of reaction (left) and flame surface area (right) contributions to the impulse response. From top to bottom, impulse responses with different perturbation locations are shown, respectively $a = R \times$ [1,0.75,0.5,0.25,0]. Last row is the uniform impulse responses.

For validation purposes, the IR for a uniform equivalence ratio perturbation is obtained by integrating the local source over the radius, mathematically

$$h^{\int}_{\Delta H}(t) = \int_0^R h_{\Delta H}(a,t)\mathrm{d}a \tag{22}$$

The final expression reads

$$h^{\int}_{\Delta H}(t) = \frac{2S_{\Delta H}}{T_c^2}(T_c - t)[H(t) - H(t - T_c)] \tag{23}$$

where $T_c = \tau_c(0)$ is the convective time scale of the perturbation at the center. The detailed derivation is given in Appendix 1. This expression is the same as the one derived by Albayrak et al.[10] The IR is plotted in last row on left column of Figure 2.

The same derivation also applies for the laminar flame speed contribution. Substituting ΔH with s_L in the equations in this subsection yields the IR for flame speed contribution.

3.2 Flame surface area contribution

First, the solution of equivalence ratio perturbation (equation (19)) is inserted to the linearized laminar flame speed (equation (11)). The resulting expression is then used as the right hand side term that is the source term for linearized ξ-equation (equation 7). The corresponding solution of the linearized ξ-equation reads

$$\xi'_a(t,r) = S_{s_L}\frac{u_z}{c_r}[H(r-a)-1]\delta\left(t - \tau_c - \tau_r + \frac{r}{c_r}\right) \tag{24}$$

where $H(t) \equiv \begin{cases} 0, & t < 0 \\ 1, & t \geq 0 \end{cases}$ is the Heaviside step function, which is equal to the integral of the Dirac delta function

$$H(t) = \int_{-\infty}^{t} \delta(t')\,dt' \tag{25}$$

τ_r is the time scale of the restoration process and reads

$$\tau_r(a) = \frac{a}{c_r} \tag{26}$$

The time scale is illustrated in Figure 1 by the dashed line from the perturbed flame to the tip of the flame.

The flame surface area contribution defined in equation (10) is calculated via equation (15) and reads

$$h_A(a,t) = -2S_{s_L}\frac{c_r}{R^2}[H(t-\tau_c) - H(t-\tau_c-\tau_r)] \tag{27}$$

In right column of Figure 2, the IR contribution is plotted for different perturbation locations, i.e. $a = R\times[0, 0.25, 0.5, 0.75, 1]$. Contrary to the flame speed and heat of reaction contributions, the area contribution is not a local process. The contribution starts when the perturbation reaches with the flame, which is related with the convective time scale τ_c. Change in the laminar flame speed occurs at the location of contact and results in flame displacement. Assuming a lean premixed flame with positive equivalence ratio perturbation indicates that the flame displacement is in upstream direction and thus causes a negative response. This is shown in Figure 2. A negative response is generated at the time τ_c. Then, the perturbed flame is transported towards flame tip, which occurs with the restorative time scale τ_r. The IR contribution vanishes once the perturbed flame reaches the flame tip.

For validation purposes, the IR for uniform equivalence ratio perturbation is obtained by integrating the local source over the whole radius. Mathematically

$$h^{\int}_{A}(t) = \int_0^R h_A(a,t)\mathrm{d}a \tag{28}$$

The final expression reads

$$h^{\int}_{A}(t) = -\frac{2S_{s_L}}{T_c(T_r - T_c)} \times \left[\frac{T_c}{T_r}\{R(t-T_r) - R(t)\} - \{R(t-T_c) - R(t)\}\right] \tag{29}$$

where $T_r = \tau_r(R)$ is the global restorative time scale and $R(t) \equiv \max(t, 0)$ is the ramp function, which is equal to the integral of the Heaviside function

$$R(t) = \int_{-\infty}^{t} H(t')\,dt' \tag{30}$$

The IR is shown in last row of the right column of Figure 2. Again, this expression agrees with the results of Albayrak et al.[10]

4. Comparison of perturbation types

A generic description of the equivalence ratio perturbations can be defined as a boundary condition

$$\phi'_a(t,0,r) = C_f(a)\bar{\phi}\delta(t) \tag{31}$$

The overall IR contribution $h^{\int}$ can be calculated from the local source IR h_a as

$$h^{\int}(t) = \int_0^R C_f(a)h_a(t)\mathrm{d}a \tag{32}$$

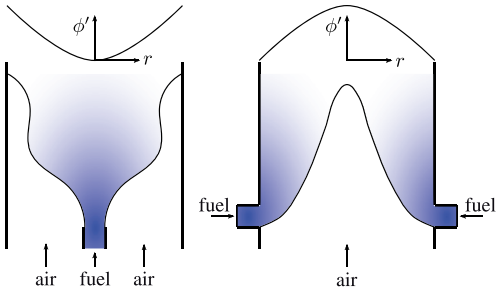

Figure 3. Sketches of two possible fuel injector configurations for technically premixed flames. Left: the fuel injection at the center and air supply as co-flow. Right: fuel supply from side walls. The blue color represents the equivalence ratio perturbations $\phi\prime$. On top, $\phi\prime$ is plotted against the radius.

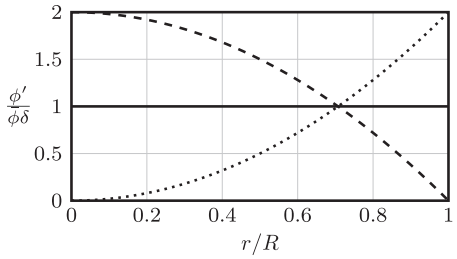

Figure 4. Different radial profiles for equivalence ratio perturbations. (——) is uniform profile, (- - -) is parabolic profile with side wall fuel injection, and (·····) is with center fuel injection.

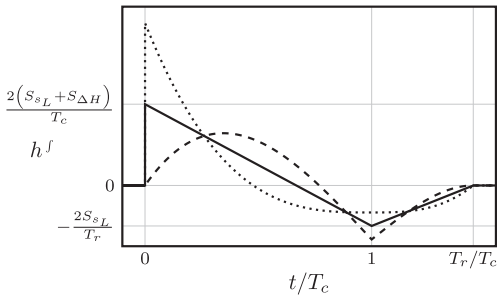

Figure 5. Overall impulse responses for uniform (——), parabolic with side wall fuel injection (- - -), and with center fuel injection (·····) equivalence ratio perturbations.

where C_f stands for the form factor, which is $C_f = 1$ for the uniform perturbation.

For illustration purposes, an uniform perturbation profile is compared against parabolic profiles. Possible configurations are illustrated as sketch in Figure 3. In the left part of the figure, the choked fuel injection at the center with a co-flow air supply is shown. Flow perturbations in the air supply cause equivalence ratio fluctuations. The magnitude of the equivalence ratio perturbations is higher closer to the side walls, since the choked fuel flow prevents the penetration to the center region. In the right part of the figure, the reversed configuration is shown, i.e. the choked fuel injection is supplied through side walls. In this configuration, penetration to the side walls is prevented. This yields an equivalence ratio perturbation with higher magnitude in the center.

The form factors C_f^c and C_f^s indicate the case with center fuel injection and the side fuel injection, respectively. Perturbation strengths are kept constant as the uniform profile, i.e. $\int_0^R aC_f \mathrm{d}a = \int_0^R a\mathrm{d}a$. The form factors are approximated by parabolic functions

$$C_f^c = 2\frac{a^2}{R^2} \tag{33}$$

$$C_f^s = 2\left(1-\frac{a}{R}\right)\left(1+\frac{a}{R}\right) \tag{34}$$

The profiles are shown in Figure 4. The burner radius is $R = 1$ mm, the axial flow velocity is $u_z = 1$ m/s and the mean equivalence ratio is $\bar{\phi} = 0.8$. Corresponding laminar flame speed is $\bar{s}_L = 0.278$ m/s. The global convective time of perturbation is $T_c = 3.45$ ms and the global restoration time scale is $T_r = 3.74$ ms.

The IRs are shown in Figure 5. The solid line indicates the uniform perturbation profile, which also corresponds to the model derived by Albayrak et al.[10] The dashed and dotted lines correspond to the fuel injection from side walls and the center, respectively. The global time scales, i.e. T_c and T_r, are the same for all perturbations profiles. However, initial response of the side fuel injection is less steep than the uniform profile because the perturbations close to the walls are weak. The positive response region of the parabolic profile is longer. This can be explained by the stronger positive contributions at the center, i.e. the flame speed and heat of reaction contributions, because the equivalence ratio perturbation is higher around the center. This is followed by a narrower but a stronger negative response, which is mainly caused by the flame surface area contribution.

The response of the center fuel injection case is stronger at the beginning compared to the uniform profile due to the large amplitude perturbation close to the walls. However, the positive response region is shorter and followed by a longer and weaker negative response. This is explained by the weak equivalence ratio perturbation close to the center.

The corresponding FTFs are calculated as the Fourier Transform of the IRs. For the case of the uniform perturbation profile, the corresponding results previously derived by Shreekrishna et al.[9] are recovered

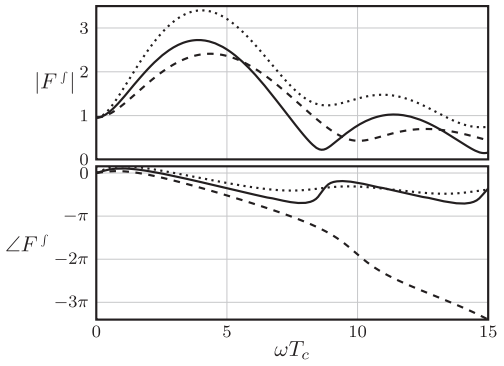

Figure 6. Flame transfer functions for uniform (——), parabolic with side wall fuel injection (- - -), and with center fuel injection (·····) equivalence ratio perturbations.

exactly. Results are shown in Figure 6. The gain for the case with the side fuel injection is slightly stronger than the other profiles. Considerable deviation is observed in phase for the case with the center fuel injection.

5. Conclusion

The linear response of a technically premixed flame to perturbations of equivalence ratio is investigated using a level set method ("*G*-equation"). In particular, the time-domain-based, analytical model proposed by Albayrak et al.[10] is extended to account for local modulations of fuel concentration, which are likely to result from imperfect fuel–air premixing in technical applications. Three major contributions to the fluctuations in heat release rate—related to modulation of heat of reaction, laminar flame speed, and flame surface area, respectively[8]—are analyzed for the case of a local perturbation. It is demonstrated that the heat of reaction and laminar flame speed contributions are local processes in the sense that the flame response is activated once the perturbation reaches the flame. Therefore, they are characterized by a local convective time scale τ_c, which is the time for the local perturbation to travel from the flame base to the flame surface. The third contribution, related to flame surface area, is an indirect mechanism caused by the modulation of the laminar flame speed, which locally induces a wrinkle in the flame shape that propagates towards the flame tip. This process is related to the restoration time scale τ_r identified by Blumenthal et al.[11] Thus, the flame surface area affects the heat release rate during a time interval from τ_c to τ_r.

For validation purposes, the IR to a perturbation with uniform profile, which was already studied by Albayrak et al.[10] and Cho and Lieuwen,[8] is recovered with the method proposed in this paper. Moreover, the method is applied in an exemplary manner to two parabolic perturbation profiles, which can be regarded as a technically premixed case with fuel injection from the center and side walls, respectively. It is shown that the flame response, particularly the phase of the FTF, can be altered significantly by the non-uniformity of equivalence ratio perturbations.

The local flame IR is a simple yet powerful concept, which allows to determine the response to arbitrary profiles of equivalence ratio perturbations as an integral over local perturbations. Closed form analytical solutions for the flame impulse can be found if mean equivalence ratio and mean flow velocities are assumed to be uniform, as was the case in the present study. More complicated configurations can be calculated numerically, however the underlying physics is the same. Including the generation and propagation of local equivalence ratio fluctuations in more realistic flow configurations can be an interesting future work. The impact of the local convective time scales on the flame response can be analyzed.

In this work, the time domain approach is preferred over the frequency domain approach, although they contain the same information. This is justified by the convective processes, which can be interpreted from a time domain approach. The local response can be also derived in the frequency domain as the FTF, which can be extended for the case the weakly non-linear response.

Acknowledgments

The presented work is part of the Marie Curie Initial Training Network Thermo-acoustic and aero-acoustic nonlinearities in green combustors with orifice structures (TANGO).

Declaration of Conflicting Interests

The author(s) declared no potential conflicts of interest with respect to the research, authorship, and/or publication of this article.

Funding

The author(s) disclosed receipt of the following financial support for the research, authorship, and/or publication of this article: the European Commission under call FP7-PEOPLE-ITN-2012 and the Research Association for Combustion Engines (Forschungsvereinigung Verbrennung e.V.—FVV, project number: 6011702).

Note

a. Some authors prefer the term "practical premixed flames".

References

1. Lawn CJ and Polifke W. A Model for the Thermoacoustic Response of a Premixed Swirl Burner, Part II: The Flame Response. *Combust Sci Technol* 2004; 176: 1359–1390.

2. Lieuwen TC. *Unsteady combustor physics*. UK: Cambridge University Press, 2012.
3. Kerstein AR, Ashurst WT and Williams FA. Field Equation for Interface Propagation in an Unsteady Homogeneous Flow Field. *Phys Rev A* 1988; 37: 2728–2731.
4. Boyer L and Quinard J. On the Dynamics of Anchored Flames. *Combust Flame* 1990; 82: 51–65.
5. Fleifil A, Annaswamy AM, Ghoneim ZA, et al. Response of a Laminar Premixed Flame to Flow Oscillations: A Kinematic Model and Thermoacoustic Instability Results. *Combust Flame* 1996; 106: 487–510.
6. Schuller T, Durox D and Candel S. A Unified Model for the Prediction of Laminar Flame Transfer Functions: Comparisons Between Conical and V-Flame Dynamics. *Combust Flame* 2003; 134: 21–34.
7. Dowling AP and Hubbard S. Instability in Lean Premixed Combustors. *Proc IMechE, Part A: J Power and Energy* 2000; 214: 317–332.
8. Cho JH and Lieuwen TC. Laminar Premixed Flame Response to Equivalence Ratio Oscillations. *Combust Flame* 2005; 116–129.
9. Shreekrishna, Hemchandra S and Lieuwen T. Premixed Flame Response to Equivalence Ratio Perturbations. *Combust Theory Modell* 2010; 14: 681–714.
10. Albayrak A, Blumenthal RS, Ulhaq A, et al. An Analytical Model for the Impulse Response of Laminar Premixed Flames to Equivalence Ratio Perturbations. *Proc Combust Inst* 2017; 36: 3725–3732.
11. Blumenthal RS, Subramanian P, Sujith R, et al. Novel Perspectives on the Dynamics of Premixed Flames. *Combust Flame* 2013; 160: 1215–1224.
12. Abu-Off G and Cant R. Reaction Rate Modeling for Premixed Turbulent Methane-air Flames. In: *Proceedings of the joint meeting of Spanish*, Portuguese, Swedish and British Sections of the Combustion Institute, Madeira, 1996.

Appendix 1

The derivation of the heat of reaction contribution to the impulse response for the uniform perturbation $h^{\int}_{\Delta H}(t)$ (equation (23)) is demonstrated starting from the local heat of reaction contribution $h_{\Delta H}(a,t)$ (equation (20)).

Substituting equation (20) in the integral in equation (22) yields

$$h^{\int}_{\Delta H}(t) = \frac{2S_{\Delta H}}{R^2}\int_0^R a\delta(t-\tau_c)\mathrm{d}a \tag{35}$$

where $\tau_c = T_c(1-a/R)$ is valid for a conical flame. The change of variables $b = t - T_c(1-a/R)$ yields

$$h^{\int}_{\Delta H}(t) = \frac{2S_{\Delta H}}{T_c^2}\left[\int_{t-\tau_c}^{t} b\delta(b)\mathrm{d}b + (T_c - t)\int_{t-\tau_c}^{t}\delta(b)\mathrm{d}b\right] \tag{36}$$

The first integral is zero. The second integral is evaluated by using the fact that the Heaviside step function is the anti-derivative of the Dirac delta function. The result reads

$$h^{\int}_{\Delta H}(t) = \frac{2S_{\Delta H}}{T_c^2}(T_c - t)[H(t) - H(t-T_c)] \tag{37}$$

Now, we derive the same for the parabolic profile that corresponds to the center fuel injection case. Substituting the form factor $C_f = 2a^2/R^2$ into equation (32), the integral term reads

$$h^{\int}_{\Delta H}(t) = \frac{2S_{\Delta H}}{R^4}\int_0^R a^3\delta(t-\tau_c)\mathrm{d}a \tag{38}$$

Again, we perform the change of variables $b = t - T_c(1-a/R)$. The resulting integral reads

$$h^{\int}_{\Delta H}(t) = \frac{2S_{\Delta H}}{T_c^4}\int_{t-\tau_c}^{t}(b - t + T_c)^3\delta(b)\mathrm{d}b \tag{39}$$

Since all integrals $\int b^n\delta(b)\mathrm{d}b$ with $n \in \mathbb{N}_1$, the only the integral with $n = 0$ remains

$$h^{\int}_{\Delta H}(t) = \frac{2S_{\Delta H}}{T_c^4}(T_c - t)^3\int_{t-\tau_c}^{t}\delta(b)\mathrm{d}b \tag{40}$$

This integral is calculated as

$$h^{\int}_{\Delta H}(t) = \frac{2S_{\Delta H}}{T_c^4}(T_c - t)^3[H(t) - H(t-T_c)] \tag{41}$$

The flame surface area contribution is calculated in an analogous manner.

Alp Albayrak[1]
Fakultät für Maschinenwesen,
Technische Universität München,
Boltzmannstraße 15,
Garching D-85747, Germany
e-mail: albayrak@tfd.mw.tum.de

Thomas Steinbacher
Fakultät für Maschinenwesen,
Technische Universität München,
Boltzmannstraße 15,
Garching D-85747, Germany
e-mail: steinbacher@tfd.mw.tum.de

Thomas Komarek
Fakultät für Maschinenwesen,
Technische Universität München,
Boltzmannstraße 15,
Garching D-85747, Germany

Wolfgang Polifke
Fakultät für Maschinenwesen,
Technische Universität München,
Boltzmannstraße 15,
Garching D-85747, Germany
e-mail: polifke@tfd.mw.tum.de

Convective Scaling of Intrinsic Thermo-Acoustic Eigenfrequencies of a Premixed Swirl Combustor

Spectral distributions of the sound pressure level (SPL) observed in a premixed, swirl stabilized combustion test rig are scrutinized. Spectral peaks in the SPL for stable as well as unstable cases are interpreted with the help of a novel criterion for the resonance frequencies of the intrinsic thermo-acoustic (ITA) feedback loop. This criterion takes into the account the flow inertia of the burner and indicates that in the limit of very large flow inertia, ITA resonance should appear at frequencies where the phase of the flame transfer function (FTF) approaches $-\pi/2$. Conversely, in the limiting case of vanishing flow inertia, the new criterion agrees with previous results, which state that ITA modes may arise when the phase of the FTF is close to $-\pi$. Relying on the novel criterion, peaks in the SPL spectra are identified to correspond to either ITA or acoustic modes. Various combustor configurations are investigated over a range of operating conditions. It is found that in this particular combustor, ITA modes are prevalent and dominate the unstable cases. Remarkably, the ITA frequencies change significantly with the bulk flow velocity and the position of the swirler but are almost insensitive to changes in the length of the combustion chamber (CC). These observations imply that the resonance frequencies of the ITA feedback loop are governed by convective time scales. A scaling rule for ITA frequencies that relies on a model for the overall convective flame time lag shows good consistency for all operating conditions considered in this study. [DOI: 10.1115/1.4038083]

1 Introduction

Stricter emission regulations, in particular for nitrogen oxides (NO_x), promoted the development of lean premixed combustion systems. Such combustors, however, often exhibit increased emissions of combustion noise and are more susceptible to thermo-acoustic instabilities [1,2]. Such self-excited instabilities arise from feedback between the unsteady heat release of the flame and flow perturbations—in particular acoustic waves—in a combustor. High amplitude pressure and velocity oscillations resulting from thermo-acoustic interactions can cause problems ranging from increased noise emissions to severe damage of the complete system.

Thermo-acoustic instabilities are commonly characterized as acoustic eigenmodes of the combustion system driven by heat release fluctuations of the flame [3]. The flame is viewed as a source, which feeds perturbation energy into the acoustic modes. However, Hoeijmakers et al. [4,5] showed that velocity sensitive flames can develop thermo-acoustic instabilities even in a fully anechoic environment. This appears paradoxical, since all acoustic perturbations generated by the flame leave an anechoic domain without reflection; acoustic modes cannot form in such an environment. Polifke and coworkers, however, identified the so-called *intrinsic thermo-acoustic* (ITA) feedback loop between unsteady heat release by the flame and upstream velocity fluctuations, which does not involve reflection of acoustic waves at the combustor inlet or exit [6,7]. Numerical simulation [8,9] of intrinsic instabilities of laminar premixed flames in computational domains with nonreflecting boundary conditions confirmed the results of Hoeijmakers. Emmert et al. [10] argued that the ITA feedback should play an important role even for realistic combustor configurations with (partially) reflecting boundaries, because ITA modes exist in addition to acoustic cavity modes and can, for certain conditions, be dominantly unstable. Analytical results of Mukherjee and Shrira [11] for a simple model of an n–τ flame in a resonator support these findings. It is particularly interesting that the standard methods for passive control of thermo-acoustic instabilities (i.e., acoustic liners and decreasing boundary reflection coefficients) may not stabilize ITA modes. As shown by Emmert et al. [10], just the opposite effect can be observed, i.e., increased acoustic losses at the combustor exit can enhance the ITA feedback and lead to increased growth rates. Silva et al. [12] showed that ITA resonances can lead to the formation of characteristic peaks in the spectral distribution of the sound pressure level (SPL) of broad-band combustion noise of turbulent flames.

Fundamentally, ITA feedback exists because the sound emitted by an unsteady flame *directly*—i.e., without reflection of acoustic waves by the environment—disturbs the velocity field in the vicinity of the flame. This argument is developed in more detail as follows: premixed flames respond to perturbations of upstream velocity with a change in their heat release rate $\dot{Q}$. This, in turn, generates acoustic waves that travel in both upstream and downstream direction. The upstream propagating acoustic wave g_c perturb the upstream velocity u_c and, thus, close a feedback loop, see Fig. 1. It has to be emphasized that corresponding intrinsic modes exist in addition to the acoustic modes ("cavity modes"). The ITA feedback loop may be affected but not eliminated by acoustic reflections at the boundaries or area jumps. Therefore, the frequencies of ITA modes need not to be close to acoustic eigenfrequencies of the combustor. On the other hand, one should expect that lock-on between ITA and acoustic modes is possible.

The characteristics of the ITA modes are largely determined by the flame transfer function (FTF), which relates velocity fluctuations u'_{ref} at a reference position—usually close to the flame anchoring position—to fluctuations of the heat release rate q'. In previous studies, it was argued that the frequencies of the pure ITA modes in any anechoic environment coincide with

[1]Corresponding author.

Contributed by the Combustion and Fuels Committee of ASME for publication in the Journal of Engineering for Gas Turbines and Power. Manuscript received July 28, 2017; final manuscript received August 1, 2017; published online November 7, 2017. Editor: David Wisler.

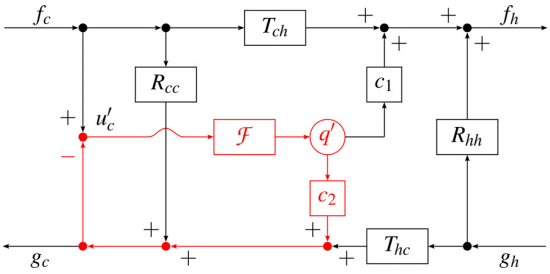

Fig. 1 Intrinsic thermo-acoustic feedback loop of a velocity sensitive flame: heat release q' responds to fluctuations of upstream velocity u'_c, thereby generating a characteristic wave g, which propagates upstream, where it perturbs velocity u'_c. The resulting intrinsic feedback loop does not involve reflection of acoustic waves at combustor inlet or outlet. R and T represent coefficients of reflection and transmission by the discontinuity of acoustic impedance across the flame, respectively.

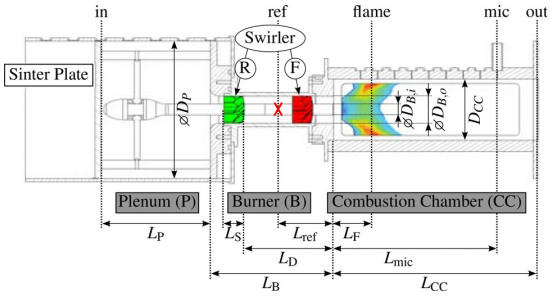

Fig. 2 Sketch of the Beschaufelter-Ring-Spalt (BRS) test rig

frequencies where the phase of the FTF is close to an odd multiple of $-\pi$ [5,7,9]. Furthermore, the gain of the FTF at those frequencies determines whether the corresponding ITA mode is stable or unstable: The higher the gain, the more prone the flame becomes to an instability driven by ITA feedback. Clearly, a flame may exhibit more than one ITA mode, provided that the gain of the FTF does not decrease rapidly with frequency.

In this work, ITA resonances and instabilities of a perfectly premixed, swirl stabilized combustor are investigated, and a refined criterion for the respective frequencies is developed. It is argued that the ITA frequencies depend not only on the phase of the FTF but also on the inertia of the burner flow, plus the ratios of temperature, cross-sectional area, and specific impedance across the flame. The analysis is validated by experimental results, where (1) the power rating, and thus the mean flow velocity, and (2) the position of the swirler are modified. Although these two measures do not change the acoustic characteristics of the system, significant shifts in peak frequencies of the SPL spectra are observed. These shifts are well predicted by the refined criterion for ITA frequencies.

The measures (1) and (2) both change the gain and in particular the phase of the FTF, i.e., the time scales of the flame response, which are understood to be convective in nature. This suggests that ITA frequencies should exhibit convective scaling. This hypothesis is substantiated by considering how relevant length and velocity scales of a turbulent flame change with bulk flow velocity. A simple relation that predicts how ITA resonance frequencies should increase with bulk flow velocity compares well with experimental results.

This paper is structured as follows: We first describe the experimental setup investigated in this study. Then, measurement methods and results for the SPL spectra and the flame frequency response (FFR) are presented. Subsequently, the distributed time lag model for the FTF is outlined. This is followed by the derivation of a refined criterion for ITA eigenfrequencies, which is then employed to interpret the experimental results. Finally, convective scaling of the ITA modes is established.

2 Experimental Setup

Measurements presented in this paper were performed on a swirl stabilized, perfectly premixed combustor as sketched in Fig. 2. All parameters are specified in Table 1. This setup is known as the "BRS burner" and has served as a base for several numerical and experimental studies, e.g., Refs. [13–15]. It consists of a cylindrical plenum (P) with an inner diameter of D_P and a length of L_P. A sinter plate is placed at the upstream end of the plenum. The porous material allows flow to pass through, but at the same time provides a defined acoustic "hard wall" boundary condition. At the combustor exit, a perforated plate is installed in order to achieve a boundary condition with reduced acoustic reflections.

Attached to the plenum is the burner (B), which comprises an annulus with inner and outer diameter $D_{B,i}$ and $D_{B,o}$, respectively, and a swirler mounted on a central bluff body. The swirler with an axial length L_S has eight vanes, which turn the flow by approximately 45 deg, resulting in a swirl number of approximately 0.74. The combustion chamber (CC) has a square cross section and a variable axial length L_{CC}. Two configurations were investigated with $L_{CC} = 300$ mm and $L_{CC} = 700$ mm. The former leads to stable operation, while the latter tends to develop thermo-acoustic instability. The combustor is operated with a methane-air mixture at an equivalence ratio of $\bar{\phi} = 0.77$ with three power settings 30, 50, and 70 kW, which correspond to a bulk axial flow speed inside the burner annulus $\bar{u}_B$ of ($\bar{u}_B = 11.3$, 18.8, and 26.4 m/s), respectively. The increase in thermal power leads to a small axial shift of the spatial distribution of the maximum heat release and, thus, to a slight elongation of the flame.

The swirler can be placed at two axial positions denoted by "R" for the rear and "F" for the front position. The front position is located 30 mm before the combustion chamber, the rear at 130 mm. A change in the swirler positions has only a negligible effect on the mean distribution of heat release but results in a significant change of the FTF [13]. Inspired by studies of Straub and Richards [16] on the effect of fuel nozzle configuration on premix combustion dynamics, Komarek and Polifke [13] explained that this effect results from superposition of the respective responses of the flame to axial and tangential velocity fluctuations. Since the axial velocity fluctuations travel with the speed of sound, while the tangential velocity fluctuations are convected by the mean flow, a change in the swirler position by half a convective wavelength alters the superposition of the respective contributions and

Table 1 Parameters of the BRS test rig

Length	$L_P = 0.17, L_S = 0.03, L_B = 0.18, L_{ref} = 0.07, L_F = 0.045\ L_{CC} = L_{mic} = (0.3, 0.7)$, $L_D = (0.03, 0.13)\ D_P = 0.2, D_{B,o} = 0.04, D_{B,i} = 0.016, D_{CC} = 0.09$ m
Mean velocity at burner (B)	30, 50, 70 kW, respectively $\bar{u}_B = 11.3, 18.8, 26.4$ m/s
Cross-sectional area	$A_P = \frac{\pi}{4}D_P^2, A_B = \frac{\pi}{4}\left(D_{B,o}^2 - D_{B,i}^2\right), A_{CC} = D_{CC}^2$
Temperature	$T_c = 293, T_h = 1930$ K

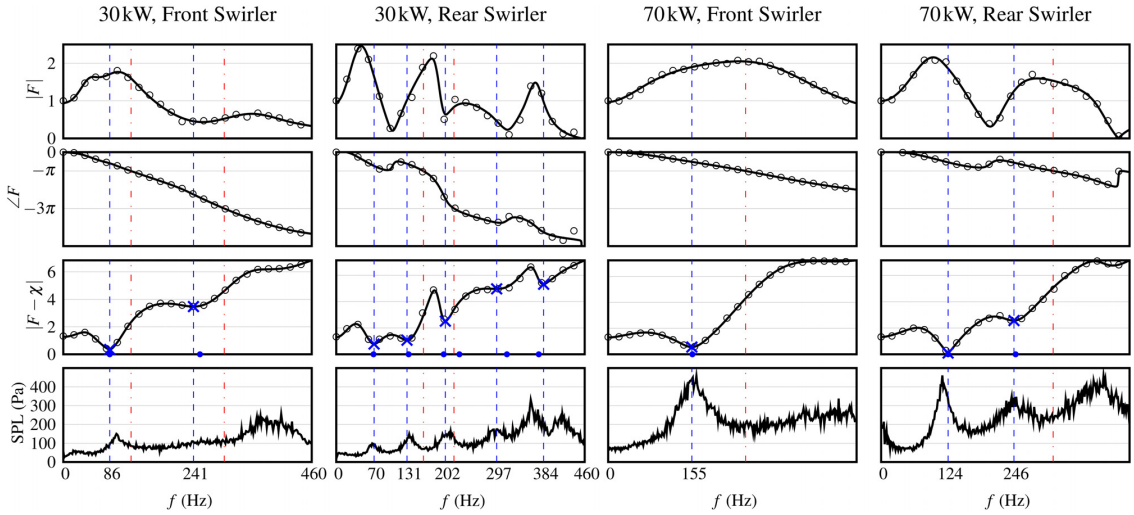

Fig. 3 Stable operating condition with $L_{CC} = 300$ mm. Vertical lines indicate ITA frequencies according to $-\pi$ criterion (- - -) and refined criterion (- - -), respectively. Top three rows: measurements (○) versus model (——) of FTF. Row 1 and 2: gain and phase of FTF. Row 3: absolute value of dispersion relation, solution of $\mathcal{F}_M - \chi = 0$ (•), local minima of $|F - \chi|$ (×). Row 4: measured sound pressure levels.

thus the overall flame dynamics significantly. These arguments were corroborated by studies of Palies et al. [17] on the dynamics of swirling flames.

3 Spectral Distribution of Sound Pressure Levels

Time series of pressure fluctuations are measured by a microphone placed at the position "mic" in Fig. 2. From these data, the noise level in terms of the SPL spectrum is estimated using Welch's method with a symmetric Hamming window of a width of 20,000. No acoustic excitation was applied.

The SPL spectra for the 30 kW and 70 kW cases with the short combustion chamber ($L_{CC} = 300$ mm) are plotted in the bottom row of Fig. 3. These cases correspond to a stable operating condition. Accordingly, the SPL spectra show several fairly broad resonant peaks of moderate height. Figure 3 shows clearly that under variation of power rating—at constant equivalence ratio—or swirler position, both frequencies and amplitudes of the peaks change. The changes in frequency are remarkable, because the speed of sound in plenum and combustor, which governs the acoustic eigenfrequencies of the test rig, is not affected by changes in power rating or swirler position.

By increasing the combustion chamber length from $L_{CC} = 300$ mm to $L_{CC} = 700$ mm, the 30 kW cases become unstable. Figure 4 shows the corresponding SPL spectra. The front position case (left plot) has a strong peak at a frequency near 100 Hz and its multiples. Similarly, the rear position case (right plot) has a peak frequency near 60 Hz and its multiples. For the 70 kW power rating with elongated combustion chamber, the combustor is stable; therefore, the SPL spectrum is not shown here.

4 Measurement of Flame Frequency Response

The FFR, which describes the response of the flame to upstream velocity perturbations, is determined by acoustically exciting the flame with a siren [18]. The normalized axial velocity fluctuations $u'_{\mathrm{ref}}/\bar{u}_{\mathrm{ref}}$ at a point 70 mm upstream of the beginning of the combustion chamber (marked by a cross in Fig. 2) are related to the normalized integrated heat release fluctuations $Q'/\bar{Q}$ of the flame at discrete frequencies ω_n

$$F(\omega_n) = \frac{Q'(\omega_n)/\bar{Q}}{u'_{\mathrm{ref}}(\omega_n)/\bar{u}_{\mathrm{ref}}}, \omega_n \in \mathbb{R} \tag{1}$$

The velocity signal was captured by a constant temperature anemometry probe and the heat release by a photomultiplier with an interference filter attached (centered on a wavelength of $307.1 + 3/-0$ nm; half power bandwidth of 10 ± 2 nm; transmission of 15%).

For the stable configuration with a short combustion chamber $L_{CC} = 300$, the FTF was measured for power ratings 30 and 70 kW, each with the swirler mounted in the front and the rear position, respectively. The results are again shown in Fig. 3 (○ symbol). For the front swirler position (left plots), the transfer function has, for both power ratings, a single excess of gain $|F| > 1$ at low frequencies, followed by a smooth decay, while the phase can be approximated with a constant negative slope.

For swirler mounted in the rear position, the gain of the FFR exhibits pronounced maxima and minima, which can be explained as the effect of constructive and destructive superposition of several contributions to the flame dynamics with different time lags. As mentioned in the introduction, the flame response of a swirl flame includes contributions from acoustic and swirl waves [13,17]. The difference in time lags is significantly larger for the rear swirler position, which leads to more frequent extrema in gain due to more rapid alternations between constructive and destructive interference (see Ref. [19]). For the swirler mounted in the rear position, the phase follows the same overall slope as for the front position but exhibits jumps at several frequencies, i.e., at 100 Hz for the 30 kW and at 210 Hz for the 70 kW cases. These frequencies match with the local minima of the gain. This

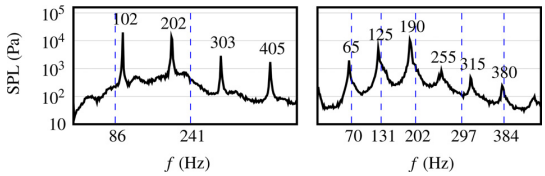

Fig. 4 SPL for unstable 30 kW case. Left/right: front/rear swirler position. Vertical lines: refined criterion - - -.

is a typical behavior of systems governed by processes with different time scales, cf. [20] for an illustrative example.

The increase of the power rating from 30 to 70 kW affects noticeably the slope of the phase, since the characteristic time delay of the flame changes. This is largely an effect of the change in the flow velocity $\bar{u}_B$ and the flame length L_F, as described by Alemela et al. [21]. This is discussed in more detail in the following.

5 Modeling of Flame Transfer Function

As suggested by Subramanian et al. [22], a distributed time lag model in the form of a stable rational function is used in this work to model the flame transfer function

$$\mathcal{F}_M(\omega) = \sum_{k=1}^{n} \frac{C_k}{i\omega - A_k},\ \omega \in \mathbb{C} \tag{2}$$

where approximately $n \approx 10$ poles suffice to provide a good fit to the measured flame frequency response. Here, ω is the angular frequency and i is the complex unit. During regression, all parameters C_k and A_k are optimized such that the quadratic error between the measured data and the model is minimized. According to Polifke and Lawn [23], the frequency response at the low-frequency limit $\omega = 0$ should be 1, which corresponds to a gain value of 1 and a phase value of 0. By adding these data point to the experimental data set, we ensure that the resulting FTF satisfies this condition.

The Bode plot of the resulting FTF for the 30 kW is shown with the solid line —— in Fig. 3 (first two columns and first two rows). Similarly, for the 70 kW case, the corresponding FTF is shown in Fig. 3 (last two columns and first two rows). The fitted models are in excellent agreement with the measurements of the FFR. At frequencies higher than the plotted ones, the model predicts a quick decay of the gain to 0. This agrees well with the low-pass filter behavior of a realistic flame transfer function as described by Merk [24]. For the analysis performed in this study, only frequencies below 440 Hz are relevant, since all observed ITA modes are within this range.

6 Criteria for Intrinsic Thermo-Acoustic Frequencies

Intrinsic thermo-acoustic frequencies can be estimated by a simple criterion proposed independently by Hoeijmakers et al. [5] and Emmert et al. [7], which we refer to as the "$-\pi$ criterion." Here, the argument is developed for an anchored flame in a straight duct with anechoic boundaries, see Fig. 5. Following Silva et al. [8], the equations for such a configuration are written as

$$\begin{bmatrix} -1 & R_{\text{in}} & 0 & 0 \\ T_{11} & T_{12} & -1 & 0 \\ T_{21} & T_{22} & 0 & -1 \\ 0 & 0 & R_{\text{out}} & -1 \end{bmatrix} \begin{bmatrix} f_{\text{in}} \\ g_{\text{in}} \\ f_{\text{out}} \\ g_{\text{out}} \end{bmatrix} = \begin{bmatrix} 0 \\ 0 \\ 0 \\ 0 \end{bmatrix} \tag{3}$$

where T_{ij} are the coefficients of the acoustic transfer matrix of the flame. R_{in} and R_{out} refer to inlet and outlet reflection coefficients. In general, all T's and R's are functions of ω. The corresponding dispersion relation evaluates to

$$T_{22} - R_{\text{out}}T_{12} + R_{\text{in}}T_{21} - R_{\text{in}}R_{\text{out}}T_{11} = 0 \tag{4}$$

where the l.h.s. is the determinant of the system matrix. With anechoic inlet and outlet boundaries $R_{\text{in}} = R_{\text{out}} = 0$, this equation simplifies further to $T_{22} = 0$. For a velocity sensitive flame

$$T_{22} = \frac{1}{2}\left(\xi_f + 1 + \theta\mathcal{F}\right) \tag{5}$$

with the temperature ratio $\theta = T_h/T_c - 1$ and the ratio of the impedances $\xi_f = (\rho_c c_c)/(\rho_h c_h)$ [8]. T denotes the temperature, ρ is the density and c is the speed of sound. The subscripts c and h indicate position, upstream (cold) and downstream (hot) of flame, respectively. The dispersion relation (4) reduces to

$$\mathcal{F} = -\frac{\xi_f + 1}{\theta} \tag{6}$$

This expression can be solved analytically if the FTF is represented by a simple time lag model $\mathcal{F} = Ne^{-i\omega\tau_F}$, where τ_F is the time lag and N is the gain of the FTF, yielding the flame intrinsic frequencies

$$f_{\text{ITA}} = \left(\frac{2n+1}{2\tau_F}\right)_{n\in\mathbb{N}_0} \tag{7}$$

which are identified as the frequencies where the phase of FTF is equal to $-(2n+1)\pi$. Hoeijmakers et al. [5] showed that this simple criterion works also for realistic FTFs. A graphical representation of the dispersion relation as a phasor plot also leads to the conclusion that ITA frequencies should occur close to frequencies, where the phase of the flame transfer function is close to an odd multiple of $-\pi$, see Fig. 6 in Ref. [25].

However, if the $-\pi$ criterion is applied to the BRS test rig, the estimated frequencies do not coincide with the peaks in SPL, see, vertical, dashed-dotted lines - - - in Fig. 3. In order to resolve this discrepancy, we argue that ITA frequencies may be significantly influenced by the *flow inertia* of the flame holder or burner, which for the present configuration can be regarded as the inertia of the air column inside the annulus. We propose a refined, more accurate criterion for ITA frequencies by solving the dispersion relation for a combined "burner and flame" configuration as shown in Fig. 6.

The overall transfer matrix for burner and flame is formed by considering the area jump between the plenum and the upstream of the mixing duct (p–u), the propagation of waves inside the mixing duct section (u–d), the area jump between the downstream of mixing duct, and the combustion chamber (d–c) as well as the flame (c–h). Location (d) is assigned as the velocity reference position of the FTF. The coupling relations across all elements read as

$$\begin{bmatrix} f_u \\ g_u \end{bmatrix} = 0.5 \begin{bmatrix} 1+\alpha_1 & 1-\alpha_1 \\ 1-\alpha_1 & 1+\alpha_1 \end{bmatrix} \begin{bmatrix} f_p \\ g_p \end{bmatrix} \tag{8}$$

$$\begin{bmatrix} f_d \\ g_d \end{bmatrix} = \begin{bmatrix} e^{-i\omega L_B/c_c} & 0 \\ 0 & e^{i\omega L_B/c_c} \end{bmatrix} \begin{bmatrix} f_u \\ g_u \end{bmatrix} \tag{9}$$

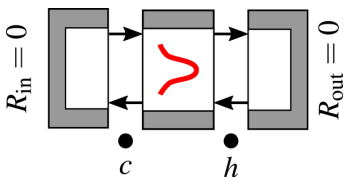

Fig. 5 Flame intrinsic configuration

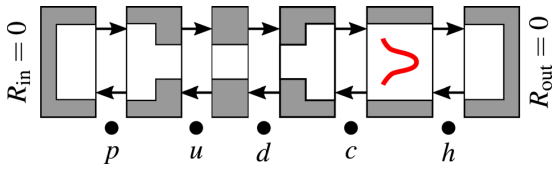

Fig. 6 Flame and burner placed in an anechoic environment

$$\begin{bmatrix} f_c \\ g_c \end{bmatrix} = 0.5 \begin{bmatrix} 1+\alpha_2 & 1-\alpha_2 \\ 1-\alpha_2 & 1+\alpha_2 \end{bmatrix} \begin{bmatrix} f_d \\ g_d \end{bmatrix} \tag{10}$$

$$\begin{bmatrix} f_h \\ g_h \end{bmatrix} = 0.5 \begin{bmatrix} \xi_f+1 & \xi_f-1 \\ \xi_f-1 & \xi_f+1 \end{bmatrix} \begin{bmatrix} f_c \\ g_c \end{bmatrix} + 0.5\alpha_2\theta\mathcal{F} \begin{bmatrix} 1 & -1 \\ -1 & 1 \end{bmatrix} \begin{bmatrix} f_d \\ g_d \end{bmatrix} \tag{11}$$

(again we refer to Ref. [8] for details). The overall transfer matrix T_{ij} from location "p" to "h" (see Fig. 6) is obtained by sequential matrix multiplication of the transfer matrices that appear in Eqs. (8)–(11). The dispersion relation $T_{22} = 0$ corresponding to the case of anechoic boundaries can be simplified considerably if one assume that the burner is acoustically compact, $\omega L_B/c_c \ll 1$, such that $e^{\pm i\omega L_B/c_c} \approx 1 \pm i\omega L_B/c_c$. In that case, one obtains the dispersion relation

$$\mathcal{F} = \underbrace{-\frac{1}{\theta}\left(1 + \frac{\xi_f}{\alpha} + ikL_l\xi_f\right)}_{\chi} \tag{12}$$

where $k = \omega/c_c$ is the axial wave number and $\alpha = \alpha_1\alpha_2$ is the area ratio between plenum and combustion chamber. The latter is a product of the two area ratios plenum-burner $\alpha_1 = A_P/A_B$ and burner-combustion chamber $\alpha_2 = A_B/A_{CC}$. The *inertial length*

$$L_I \equiv \frac{\alpha_1^2 - 1}{\alpha_1^2\alpha_2} L_B \tag{13}$$

quantifies the flow inertia of the burner. We identify the frequencies where the dispersion relation (12) has a solution, $F(\omega) - \chi(\omega) = 0$, as ITA frequencies of the combined burner and flame system.

If the area ratio between plenum and burner is large, the inertial length is larger than the geometrical length of the burner. Thus, the flow inertia may be very significant even for a burner that is acoustically compact. For the case of a very large area ratio between plenum and burner, $\alpha_1 \gg 1$, one approximates $L_I \approx L_B/\alpha_2$, and the dispersion relation (12) reduces to the expression derived by Polifke [25] for identifying the frequencies, where the instability potentiality of a burner attains a maximum. The intimate connection between ITA feedback and the instability potentiality was explicated by Emmert et al. [7]. On the other hand, for the case of an acoustically transparent flame holder with $\alpha = 1$ and $L_I \to 0$, the dispersion relation (12) reduces to the established result Eq. (6), i.e., the $-\pi$ criterion.

It is not possible to solve the dispersion relation Eq. (12) by using the measured flame frequency response F, since it only contains sampled information at real frequencies $\omega_n \in \mathbb{R}$. If a stable rational function model $\mathcal{F}_M$ for the flame transfer function is fit to the measurements as described earlier, the dispersion relation $\mathcal{F}_M(\omega) - \chi(\omega) = 0$ can be evaluated numerically to compute complex-valued frequencies, i.e., growth rates. This yields several frequencies and growth rates, all corresponding to ITA eigenmodes of the system shown in Fig. 6, i.e., flame and burner in an anechoic environment. The frequencies obtained from this method are indicated with markers • on the abscissa in the third row of Fig. 3.

A simpler method to estimate ITA frequencies is to evaluate the absolute value of the dispersion relation $|F - \chi|$ for real frequencies $\omega_n \in \mathbb{R}$. This can be done for every sampling point of the measured FFR without a rational fit for the FTF. By identifying the local minima of the absolute value, the ITA mode frequencies may be estimated. This absolute value of the dispersion relation is plotted in the third row of Fig. 3. Local minima are shown on the plot with the marker ×. Dashed vertical lines - - - are used to indicate the corresponding frequencies. The proximity of markers × and • indicates that this simplified criterion works well for all cases.

The ITA frequencies estimated from the dispersion relation (12) for burner and flame in an anechoic environment coincide in many cases with peaks in measured SPLs. For the 30 kW case with the front swirler position (first column of Fig. 3), a first peak in SPL is observed at around 100 Hz, which is predicted with only a slight deviation by the proposed refined criterion. In the noise spectrum around 400 Hz, a broad peak is observed. On the one hand, this is known to be the acoustic quarter wave mode of the complete system [10]. On the other hand, analysis of the dispersion relation (12) predicts an ITA mode in this frequency range at about 380 Hz. With the swirler in the rear position (second column of Fig. 3), we find ITA modes near 70, 130, and 200 Hz. All of them are captured correctly by the extended criterion. Just as for the case with the swirler mounted in the front position, an ITA mode is predicted just below 400 Hz, which is again close to the acoustic quarter wave mode. In the 70 kW case with the front swirler position (third column of Fig. 3), only a single, prominent peak is observed in the noise spectrum at around 150 Hz. For the rear swirler position (last column of Fig. 3), two peaks are observed at around 120 and 250 Hz, which may be associated with ITA feedback. A third peak emerges at around 400 Hz, which coincides with the acoustic quarter wave mode.

For the 30 kW power rating cases, the combustor becomes unstable if the combustion chamber length L_{CC} is increased from 300 mm to 700 mm. Comparison of Figs. 3 and 4 shows that the fundamental frequencies of instability for the long combustion chamber, which are 102 Hz for the swirler in the front position and 65 Hz for the swirler in the rear position, are in good agreement with the frequencies of combustion noise resonance peaks observed in the short combustor (see the two plots on the left in the bottom row of Fig. 3). At first sight, it is a remarkable, even baffling observation that the significant change in combustor acoustics that certainly must result from the increase in combustion chamber length did not affect the frequencies of SPL peaks in a significant manner. However, the fundamental frequencies of the peaks in SPL for the unstable cases are in good agreement with the estimates of the refined criterion for ITA frequencies, so we may conclude that for the BRS burner the dominant unstable modes are ITA modes, which resolves the paradox.

7 Analysis of Liming Cases

In this section, the dispersion relation Eq. (12) is analyzed for two limiting cases in order to develop a physical interpretation of the effect of burner flow inertia on the ITA feedback mechanism and the phase of the flame frequency response at ITA resonance. For the case of vanishing inertial length $L_I \to 0$, we will recover the $-\pi$ criterion discussed earlier. On the other hand, we will find that for very large inertial length $L_I \to \infty$, ITA modes should occur whenever the phase of the FTF is close to $-\pi/2$.

For the analysis of both limiting cases, a thermo-acoustic block diagram as introduced by Schuermans [26] for the coupling of acoustic velocities and pressure across a compact flame is helpful, see Fig. 7. Linearization of the Rankine–Hugoniot conditions yields the result that pressure fluctuations up- and downstream side of the flame are equal, while a discontinuity in velocities results from heat release rate oscillations

$$p'_h = p'_c \tag{14}$$

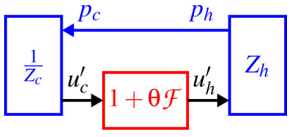

Fig. 7 Block diagram for a thermo-acoustic system

$$u'_h = u'_c + \theta q' \tag{15}$$

where $q' = Q'/\bar{Q}\bar{u}_c$. The remainder of the acoustic system can be lumped into two acoustic impedances, Z_c for elements upstream of the flame, and Z_h for elements downstream of the flame.

The first case considered is one of a burner with small inertial length L_I placed in an anechoic environment. To be precise, it is assumed that the length L_B of the burner is small, while the area ratios α_1 between plenum-burner and α_2 burner-combustion chamber are not very different from unity, such that $ikL_I\xi_f \ll 1 + \xi_f/\alpha$. This case describes an acoustically transparent burner (or flame-holder) and could be realized, e.g., by a thin perforated plate with moderate porosity.

It should be obvious that in the limit $L_I \to 0$, this setup is equivalent to the configuration in Fig. 5 described by Eq. (6), for which the $-\pi$ criterion should hold. Nevertheless, let us analyze the relative phases between fluctuating velocities, pressure, and flame heat release in more detail. The anechoic inlet and outlet boundary conditions imply for the acoustic impedances $Z_c = -\rho_c c_c$ and $Z_h = \rho_h c_h$. The corresponding system variables $[p', u'_c, u'_h, q']$ are illustrated in a phasor plot in the left part of Fig. 8.

Since the upstream and downstream pressure fluctuations are equal, $p'_c = p'_h$, only a single arrow is drawn to represent pressure, which is aligned with the real axis without loss of generality. The velocity perturbation u'_h at the downstream side is parallel to the pressure vector, because the impedance Z_h is a positive real number, i.e., multiplication with Z_h only scales the magnitude. The upstream velocity perturbation u'_c, however, is antiparallel to the pressure fluctuations, because the impedance Z_c is a negative real number. Note that the length of the vectors is only of secondary importance, the relative phases and thus the directions of vectors are significant. Nevertheless, the downstream velocity vector u'_h is represented with a longer arrow than the upstream velocity vector, since $\rho_c c_c > \rho_h c_h$. Finally, one can also construct the heat release rate vector q' from the velocity difference, as stated in Eq. (15).

The semicircular arc Z_h/Z_c represents the phase difference in acoustic velocity fluctuations across the flame. With reference to the block diagram in Fig. 7, it is noted that this relation results from the acoustic impedances, i.e., $u'_c = Z_h/Z_c u'_h$, which implies a phase difference of $-\pi$ between the velocities. The thermo-acoustic feedback loop is closed by the flame dynamics, $u'_h = u'_c + \theta q' = (1 + \theta\mathcal{F})u'_c$ as illustrated with the semicircular arc $1 + \theta/\mathcal{F}$. We see that at resonance, the phase angle for the flame response $\mathcal{F}$ is obtained by the definition of the FTF $q' = \mathcal{F}u'_c$. The angle between u'_c and q' is equal to $-\pi$, which recovers the $-\pi$ criterion.

Now, we consider the limit of a burner with very large flow inertia $L_I \to \infty$ placed in an anechoic environment. This limiting case may be realized by a burner with significant length L_B and strong flow contraction, such that $\alpha_1 \gg 1$, while $\alpha_2 \ll 1$.

The downstream impedance Z_h is unaltered, because an anechoic outlet condition is considered as in the previous case. Therefore, the fluctuations of pressure p' and downstream velocity u'_h are again aligned to each other in the phasor diagram, see the right part of Fig. 8. However, the upstream impedance Z_c is modified by the flow inertia of the burner. A momentum balance for the fluid inside the burner yields

$$p'_u - p'_d = \rho_c L_B \frac{\partial u'_B}{\partial t} \tag{16}$$

where u'_B stands for the acoustic velocity inside the burner (which is assumed to be acoustically compact). We have assumed that the cross-sectional area A_P of the plenum is much larger than that of the burner A_B, such that $\alpha_1 = A_p/A_B \gg 1$. Thus, the upstream side of the burner approximates an "open end" boundary condition with $p'_u = 0$. We obtain from Eq. (16) for the upstream impedance Z_c resulting from burner flow inertia

$$Z_c = \frac{p'_c}{u'_c} = -i\rho_c c_c L_I k \tag{17}$$

where the mass balance between burner and the combustion chamber is used for substituting $u'_B = u'_c/\alpha_2$ and the acoustic dispersion relation is used for substituting $\omega = c_c k$. The inverse of the impedance $1/Z_c$ determines the phase angle between p' and u'_c, which is $-3\pi/2$ as shown in Fig. 8. The resulting phase difference between u'_h and u'_c is illustrated with the semicircular arc Z_h/Z_c. The feedback loop is closed by the flame dynamics, as illustrated with the semicircular arc $1 + \theta/\mathcal{F}$, which relates u'_c to u'_h. Again, we examine the angle between u'_c and q' for the FTF phase angle. This angle is slightly smaller than $-\pi/2$. In the limit of very large burner flow inertia $L_I \to \infty$, the upstream velocity perturbations u'_c becomes very small compared to the downstream velocity perturbations u'_h, following the upstream impedance $Z_c \to \infty$. This necessitates that heat release rate fluctuations q' be aligned with the downstream velocity perturbations u'_h. Thus, in the limit $L_I \to \infty$ of very large burner flow inertia, the refined criterion for ITA frequencies reduces to a "$-\pi/2$ criterion," i.e., the phase of the FTF should be equal to $-\pi/2$ (or in general $-(4n+1)\pi/2$, $n \in \mathbb{N}_0$). The BRS burner has a rather large inertial length, $L_I \approx 1.4$ m, and indeed the SPL spectra in Fig. 3 show that the ITA resonances roughly comply with the $-\pi/2$ criterion.

For the small, but non-negligible values of the burner inertial length L_I, the phase of the flame transfer function at ITA resonance should be between $-\pi/2$ and $-\pi$ (up to multiples of 2π). Note that graphical analysis of the dispersion relation Eq. (12) for the configuration of burner and flame in a phasor plot—see the discussion of Fig. 6 in Ref. [25]—leads to the same conclusion. In this general case, the refined criterion described in Sec. 6—which requires numerical solution of the dispersion relation Eq. (12) or identification of the minima of $|F - \chi|$—gives a quantitative prediction of ITA frequencies for the configuration of burner and flame in an anechoic environment.

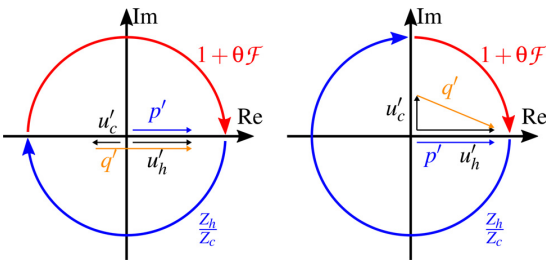

Fig. 8 Phasor diagrams for flame-only (left) and burner-flame (right) ITA feedback loops. Phase lags of acoustics and flame response are represented by circular arrows indicated by Z_h/Z_c and $1+\theta/\mathcal{F}$, respectively.

8 Convective Scaling of Intrinsic Thermo-Acoustic Frequencies

In Secs. 6 and 7, a method for identifying peaks in the SPL with ITA modes has been introduced. It has been applied to identify several stable and unstable ITA modes in experimental data of different burner configurations and operating points. In this section, we emphasize the fact that the frequencies of the ITA modes scale roughly with the bulk flow velocity inside the burner but not with the speed of sound in plenum or combustor. We distinguish between two effects: (1) a direct effect, which depends on the characteristic convective time scale of a flame, and (2) an indirect effect, which depends on the generation and propagation of so-called swirl waves. As discussed, e.g., by Komarek and Polifke [13] or Palies et al. [17], those waves propagate with a convective speed.

In Secs. 8.1 and 8.2, we focus, first, on the direct effect of a varying bulk flow velocity, which corresponds to a change of the

characteristic time scale of the flame. Second, we analyze the impact of the position of the swirler.

8.1 Bulk Flow Velocity. According to Alemela et al. [21], the characteristic time of a flame τ_F can roughly be estimated by

$$\tau_F = C_\tau \frac{L_F^*}{u_{\text{eff}}} \tag{18}$$

where L_F^* is the modified flame length and C_τ is a proportionality factor. The effective velocity u_{eff} is proportional to the axial bulk flow velocity inside the burner: $u_{\text{eff}} \propto \bar{u}_B$. The length L_F^* can be computed from the geometrical flame length L_F by a correlation including the turbulent Reynolds number Re_t and the Karlovitz number Ka [21]. By assuming $f_{\text{ITA}} \propto 1/\tau_F$ and applying Eq. (18) a scaling relation for the ITA frequencies with varying bulk flow velocities can be derived

$$\frac{f_{\text{ITA},2}}{f_{\text{ITA},1}} = \frac{L_{F,1}^*}{L_{F,2}^*}\frac{\bar{u}_{B,2}}{\bar{u}_{B,1}} = \frac{L_{F,1}}{L_{F,2}}\left[\frac{\text{Re}_{t,1}}{\text{Re}_{t,2}}\right]^{0.2}\frac{\bar{u}_{B,2}}{\bar{u}_{B,1}} \tag{19}$$

Here, the effect of the Karlovitz number was neglected. If we further assume that the turbulent Reynolds number is proportional to the bulk flow velocity $\text{Re}_t \propto \bar{u}_B$, we obtain

$$\frac{f_{\text{ITA},2}}{f_{\text{ITA},1}} = \frac{L_{F,1}}{L_{F,2}}\left(\frac{\bar{u}_{B,2}}{\bar{u}_{B,1}}\right)^{0.8} \tag{20}$$

This equation relates the ITA frequencies of two power ratings, signified by the indices 1 and 2. It is now compared to the experimental results described earlier by using the bulk velocities specified in Table 1. Data from experiments with a power rating of 50 kW (18.83 m/s), which have not been discussed until now, were added here. The axial distribution of the normalized OH^* intensity I inside the combustion chamber is plotted in Fig. 9 for these power settings. The flame lengths for the power ratings, 30, 50, and 70 kW are approximated as 41, 43.5, and 45.1 mm, respectively. This length is defined as the distance from the beginning of the combustion chamber to the maximum of the heat release. For plotting, linear interpolation is employed between these power ratings. The resulting function for the relative change of the frequency is plotted in Fig. 10 (——). Additionally, the behavior of the lowest ITA frequency for the swirler rear (- - -) and swirler front (- · -) position is plotted.

The proposed model with its nearly linear dependency captures the measured behavior quite well. A change in the power rating, and, hence the bulk flow velocity, affects the resonance frequency of the ITA feedback loop, i.e., the eigenfrequency of the ITA modes. This fact can be exploited to detect these modes: a scaling of the frequency of a certain peak in the measured SPL with bulk velocity indicates that ITA feedback is involved.

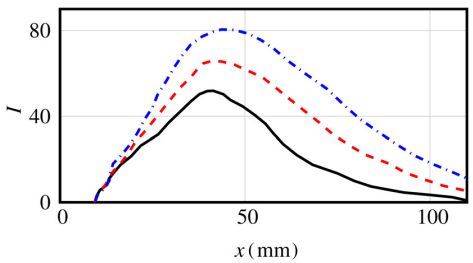

Fig. 9 Axial distribution of normalized OH^* intensity emission ——*I*. 30 kW - - -, 50 kW, and 70 kW - · -.

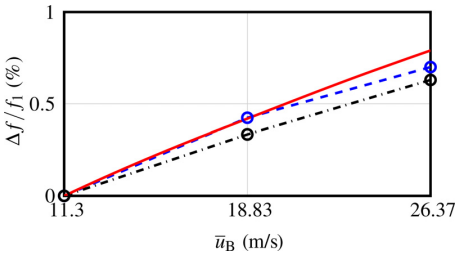

Fig. 10 Normalized variation of the dominant ITA frequency over the bulk flow velocity inside the burner. —— model from Eq. (20), - - - lowest ITA frequency of swirler rear setup, - · - lowest ITA frequency of swirler front setup.

8.2 Swirler Position. In this section, the effect of the swirler position on the ITA modes is scrutinized. The contribution of the swirl to the flame transfer function adds an additional time scale. An acoustic disturbance impinging on the swirler generates fluctuations of the swirl number. Those transversal velocity fluctuations—or swirl waves—propagate with a velocity that is of the order of the mean flow speed, which leads to a convective time lag

$$\tau_S \approx \frac{L_D}{\bar{u}_B} \tag{21}$$

here, L_D stands for the distance from the swirler to the combustion chamber inlet and $\bar{u}_B$ is the axial velocity in the mixing duct. The relevant velocities and lengths are schematically illustrated in Fig. 11. More details about interactions of acoustics with a swirler in the thermo-acoustic context can be found in a review paper by Candel et al. [27]. The processes leading to the characteristic delay described in Eq. (18) (direct effect) acts in parallel to the swirl effects from Eq. (21). If the swirler is mounted close to the flame, both time delays are of the same order of magnitude.

As the swirler is moved further away from the combustion chamber, the time lag for the swirl contribution increases, while the time delay for the direct effects stays approximately constant. As a result of the superposition of those two different time lags, the phase of the frequency response shows several bends and jumps.

For the 30 kW power rating (first two columns of Fig. 3), the overall slope of the phase is similar to the one of the front position. This is a consequence of the fact that the flow structures and flame shape are not sensitive to changes in the swirler position. However, locally the phase deviates significantly from the linear

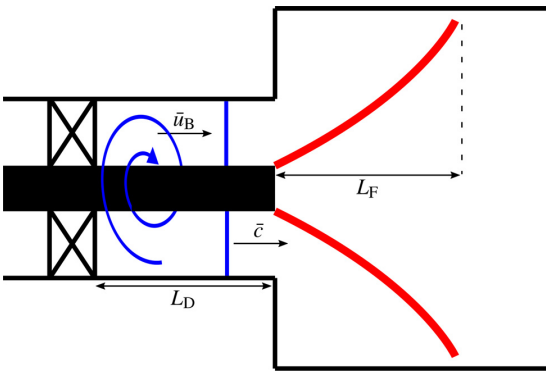

Fig. 11 Relevant length scales of the burner. L_F is the flame length and L_D is the duct length from the swirler to the combustion chamber.

decay due to the occurrence of further time scales. This introduces more ITA modes. The first ITA frequency shifts from 100 Hz (front) to 70 Hz (rear). This can be qualitatively explained by an increase of the time delay and, therefore, a decrease in the associated frequency.

A similar behavior can be observed at 70 kW. In the front swirler case, the time lag difference between acoustic and swirl components are again not significant. Therefore, the phase has a constant slope, which only leads to one ITA mode at around 155 Hz. Shifting the swirler to the rear position adds one additional mode at 246 Hz and shifts the first one to 124 Hz. Again, the frequency of the first ITA mode is reduced by moving the swirler upstream.

9 Summary and Conclusions

The experimental data from a premixed swirl combustor that are scrutinized in this study were generated almost a decade ago. At that time, flame transfer functions and sound pressure levels were measured over a range of power ratings and equivalence ratio for several values of combustion chamber length and swirl generator position. The objective of the measurement campaign was to generate a comprehensive data set, which would be used to validate the large eddy simulation (LES)/system identification approach for estimating the flame transfer function from simulation data on the one hand, and low-order network models for prediction of thermo-acoustic stability on the other. This objective was met to some extent; results of validation studies that concentrated on the flame transfer function of the flame were published by Tay-Wo-Chong et al. [14,28,29].

However, some features of this particular data set were difficult to align with our understanding of the nature of thermo-acoustic modes. For example, peaks in the spectral distribution of combustion noise showed *convective scaling*, i.e., they increased almost linearly with power rating. At constant equivalence ratio, an increase in power rating implies an increase in bulk flow velocity, while the speed of sound in the combustor remains constant, so that one would expect only a small change in acoustic frequencies. Similarly, a change in swirler position—which is commonly understood to change the flame transfer function and thus the stability, but not the frequency of a thermo-acoustic mode—resulted in a reduction of the peak frequency by more than one third. Conversely, more than doubling the length of the combustion chamber barely affected the frequency of the dominant mode in this test rig. A thermo-acoustic network model did reproduce these trends, but quantitative agreement was difficult to achieve, due to a lack of precise data on the reflection coefficient of the combustor exit and the temperature profile in the combustor. What was worse, the results did not "make sense," i.e., they could not be reconciled with the prevalent understanding that thermo-acoustic modes result from coupling of unsteady heat release with "chamber modes," i.e., acoustic modes of the combustion chamber or combined acoustic modes of plenum and combustion chamber coupled via the burner [3,27].

The present paper showed that these paradoxical observations can be explained as resonances or instabilities that result from ITA feedback, which is a feedback mechanism that does not involve reflection of acoustic waves at combustor inlet or outlet [6]. The stability and the frequencies of ITA modes is dominated by the gain and phase of the flame transfer function. In the idealized case of a velocity sensitive, time-lagged flame stabilized on an acoustically transparent flame holder in an anechoic environment, ITA modes were predicted to go unstable at frequencies where the gain of the flame response is large enough and its phase is close to a multiple of $-\pi$ [5]. For the turbulent, premixed swirl burner investigated in this study, this simple $-\pi$ criterion does not hold.

A refined criterion for ITA frequencies was deduced from the dispersion relation that describes the combined dynamics of a burner with significant flow inertia and a velocity sensitive flame in an anechoic environment. In the limiting case of very large flow inertia, the new criterion reduces to the condition that the phase of the FTF be $-\pi/2$ at ITA resonance. For small, but nonzero burner flow inertia, the phase should be between $-\pi/2$ and $-\pi$.

The refined criterion depends only on the ratios of cross-sectional areas and temperatures up- and downstream of burner and flame, the inertial length of the burner and the flame transfer function. This explains the convective scaling of ITA frequencies—recall that FTF phase scales with the characteristic convective time of the flame—as well as the observed sensitivity to swirler position and the insensitivity to combustion chamber length.

As was the case with the present study, one should expect that the concept of ITA feedback may elucidate further seemingly inexplicable observations on thermo-acoustic resonances and instabilities. On the other hand, the precise nature of the interactions between chamber and ITA modes in combustors with significant reflection coefficients poses intricate questions. Both topics are subject of ongoing investigations.

Acknowledgment

We are indebted to the anonymous reviewers of the draft version of this paper. Their critical comments prompted us to develop the refined criterion for ITA frequencies, which takes into account the flow inertia of the burner.

The support of Alstom Power Generation AG, Bayerische Forschungsstiftung, Bayerisches Staatsministerium für Wirtschaft, Forschung und Kunst, Bayerisches Staatsministerium für Wirtschaft, Infrastruktur und Technologie, and Siemens AG–Power Generation in the framework of KW21 is gratefully acknowledged.

Funding Data

- European Commission under call FP7-PEOPLE-ITN-2012 in the framework of the Marie Curie Initial Training Network Thermo-acoustic and aero-acoustic nonlinearities in green combustors with orifice structures (TANGO) (Grant No. 316654).

References

[1] Lieuwen, T., and McManus, K., 2003, "Introduction: Combustion Dynamics in Lean-Premixed Prevaporized (LPP) Gas Turbines," J. Propul. Power, **19**(5), p. 721.
[2] Poinsot, T., 2017, "Prediction and Control of Combustion Instabilities in Real Engines," Proc. Combust. Inst., **36**(1), pp. 1–28.
[3] Lieuwen, T., and Yang, V., eds., 2005, *Combustion Instabilities in Gas Turbine Engines: Operational Experience, Fundamental Mechanisms, and Modeling* (Progress in Astronautics and Aeronautics), Vol. 210, American Institute of Aeronautics and Astronautics, Reston, VA.
[4] Hoeijmakers, M., Lopez Arteaga, I., Kornilov, V., Nijmeijer, H., and de Goey, P., 2013, "Experimental Investigation of Intrinsic Flame Stability," European Combustion Meeting (ECM), Lund, Sweden.
[5] Hoeijmakers, M., Kornilov, V., Lopez Arteaga, I., de Goey, P., and Nijmeijer, H., 2014, "Intrinsic Instability of Flame-Acoustic Coupling," Combust. Flame, **161**(11), pp. 2860–2867.
[6] Bomberg, S., Emmert, T., and Polifke, W., 2015, "Thermal Versus Acoustic Response of Velocity Sensitive Premixed Flames," Proc. Combust. Inst., **35**(3), pp. 3185–3192.
[7] Emmert, T., Bomberg, S., and Polifke, W., 2015, "Intrinsic Thermoacoustic Instability of Premixed Flames," Combust. Flame, **162**(1), pp. 75–85.
[8] Silva, C. F., Emmert, T., Jaensch, S., and Polifke, W., 2015, "Numerical Study on Intrinsic Thermoacoustic Instability of a Laminar Premixed Flame," Combust. Flame, **162**(9), pp. 3370–3378.
[9] Courtine, E., Selle, L., and Poinsot, T., 2015, "DNS of Intrinsic Thermoacoustic Modes in Laminar Premixed Flames," Combust. Flame, **162**(11), pp. 4331–4341.
[10] Emmert, T., Bomberg, S., Jaensch, S., and Polifke, W., 2017, "Acoustic and Intrinsic Thermoacoustic Modes of a Premixed Combustor," Proc. Combust. Inst., **36**(3), pp. 3835–3842.
[11] Mukherjee, N., and Shrira, V., 2017, "Intrinsic Flame Instabilities in Combustors: Analytic Description of a 1-D Resonator Model," Combust. Flame, **185**, pp. 188–209.

[12] Silva, C. F., Merk, M., Komarek, T., and Polifke, W., 2017, "The Contribution of Intrinsic Thermoacoustic Feedback to Combustion Noise and Resonances of a Confined Turbulent Premixed Flame," Combust. Flame, **182**, pp. 269–278.
[13] Komarek, T., and Polifke, W., 2010, "Impact of Swirl Fluctuations on the Flame Response of a Perfectly Premixed Swirl Burner," ASME J. Eng. Gas Turbines Power, **132**(6), p. 061503.
[14] Tay-Wo-Chong, L., Bomberg, S., Ulhaq, A., Komarek, T., and Polifke, W., 2012, "Comparative Validation Study on Identification of Premixed Flame Transfer Function," ASME J. Eng. Gas Turbines Power, **134**(2), p. 021502.
[15] Nair, V., and Sujith, R., 2014, "Multifractality in Combustion Noise: Predicting an Impending Combustion Instability," J. Fluid Mech., **747**, pp. 635–655.
[16] Straub, D. L., and Richards, G. A., 1998, "Effect of Fuel Nozzle Configuration on Premix Combustion Dynamics," ASME Paper No. 98-GT-492.
[17] Palies, P., Durox, D., Schuller, T., and Candel, S., 2010, "The Combined Dynamics of Swirler and Turbulent Premixed Swirling Flames," Combust. Flame, **157**(9), pp. 1698–1717.
[18] Gentemann, A. M. G., Hirsch, C., Kunze, K., Kiesewetter, F., Sattelmayer, T., and Polifke, W., 2004, "Validation of Flame Transfer Function Reconstruction for Perfectly Premixed Swirl Flames," ASME Paper No. GT-2004-53776.
[19] Blumenthal, R. S., Subramanian, P., Sujith, R., and Polifke, W., 2013, "Novel Perspectives on the Dynamics of Premixed Flames," Combust. Flame, **160**(7), pp. 1215–1224.
[20] Lieuwen, T. C., 2012, "Aside 2.2. Effects of Simultaneous Acoustic and Vortical Velocity Disturbances," *Unsteady Combustor Physics*, Vol. 1, Cambridge University Press, Cambridge, UK, pp. 25–26.
[21] Alemela, P., Fanaca, D., Hirsch, C., Sattelmayer, T., and Schuermans, B., 2010, "Determination and Scaling of Thermo Acoustic Characteristics of Premixed Flames," Int. J. Spray Combust. Dyn., **2**(2), pp. 169–198.
[22] Subramanian, P., Blumenthal, R. S., Sujith, R., and Polifke, W., 2015, "Distributed Time Lag Response Functions for the Modelling of Combustion Dynamics," Combust. Theory Modell., **19**(2), pp. 223–237.
[23] Polifke, W., and Lawn, C. J., 2007, "On the Low-Frequency Limit of Flame Transfer Functions," Combust. Flame, **151**(3), pp. 437–451.
[24] Merk, H. J., 1957, "An Analysis of Unstable Combustion of Premixed Gases," Symp. (Int.) Combust., **6**(1), pp. 500–512.
[25] Polifke, W., 2011, "Thermo-Acoustic Instability Potentiality of a Premix Burner," European Combustion Meeting (ECM), Cardiff, UK, June 27–July 1.
[26] Schuermans, B., 2003, "Modeling and Control of Thermoacoustic Instabilities," Ph.D. thesis, École Polytechnique Fédérale de Lausanne, Lausanne, Switzerland.
[27] Candel, S., Durox, D., Schuller, T., Bourgouin, J.-F., and Moeck, J. P., 2014, "Dynamics of Swirling Flames," Annu. Rev. Fluid Mech., **46**(1), pp. 147–173.
[28] Tay-Wo-Chong, L., Komarek, T., Kaess, R., Föller, S., and Polifke, W., 2010, "Identification of Flame Transfer Functions From LES of a Premixed Swirl Burner," ASME Paper No. GT2010-22769.
[29] Tay-Wo-Chong, L., and Polifke, W., 2012, "LES-Based Study of the Influence of Thermal Boundary Condition and Combustor Confinement on Premix Flame Transfer Functions," ASME Paper No. GT2012-68796.